13 Cosmic Microwave Background

John Mather[1] · *Gary Hinshaw*[2] · *Lyman Page*[3]
[1]Astrophysics Science Division, NASA/GSFC Code 443,
Observational Cosmology, Greenbelt, MD, USA
[2]Department of Physics and Astronomy, University of British
Columbia, Vancouver, BC, Canada
[3]Department of Physics, Princeton University, Princeton, NJ, USA

Abstract: The cosmic microwave background (CMB) radiation, the relic of the early phases of the expanding universe, is bright, full of information, and difficult to measure. Along with the recession of galaxies and the primordial nucleosynthesis, it is one of the strongest signs that the Hot Big Bang Model of the universe is correct. It is brightest around 2 mm wavelength, has a temperature of T_{cmb} = 2.72548 ± 0.00057 K, and has a blackbody spectrum within 50 parts per million. Its spatial fluctuations (around 0.01% on 1° scales) are possibly the relics of quantum mechanical processes in the early universe, modified by processes up to the decoupling at a redshift of about 1,000 (when the primordial plasma became mostly transparent). In the cold dark matter (DM) model with cosmic acceleration (ΛCDM), the fluctuation statistics are consistent with the model of inflation and can be used to determine other parameters within a few percent, including the Hubble constant, the Λ constant, the densities of baryonic and dark matter, and the primordial fluctuation amplitude and power spectrum slope. In addition, the polarization of the fluctuations reveals the epoch of reionization at a redshift approximately twice that determined from the Gunn-Peterson trough due to optically thick Lyman α absorption in QSO spectra. It is of historic importance, and a testament to the unity of theory and experiment, that we now have a standard model of cosmology that is consistent with all of the observations.

Current observational challenges include (1) improvement of the spectrum distortion measurements, especially at long wavelengths, where the measured background is unexpectedly bright; (2) the search for the B-mode polarization (the divergence-free part of the polarization map), arising from propagating gravitational waves; and (3) the extension of fluctuation measurements to smaller angular scales. Much more precise spectrum observations near 2 mm are likely and would test some very interesting theories. Current theoretical challenges include explanation of the dark matter and dark energy; understanding, estimating, and removing the interference of foreground sources that limit the measurements of the CMB; detailed understanding of the influence of nonequilibrium processes on the decoupling and reionization phases; and searches for signs of the second order or exotic processes (e.g., isocurvature fluctuations, cosmic strings, non-Gaussian fluctuations). At this writing, we await the cosmological results of the Planck mission.

Keywords: Alpher, Anisotropy, ARCADE, Big Bang Theory, Blackbody, Bose-Einstein, CMB, COBE, Cold dark matter, Compton distortion, Cosmic microwave background radiation, Decoupling, Dicke, DMR, FIRAS, Foregrounds, Galactic emission, Herman, Lensing, Penzias, PIXIE, Planck, Polarization, Silk damping, Spectrum distortion, Standard model, Steady State Theory, Sunyaev–Zel'dovich, Wilson, WMAP

1 Introduction

1.1 Outline

In this article we outline the importance and the modern view of the CMB, its prediction and discovery, and the reason for its blackbody form. After a summary introduction we discuss, in section 2, the theory and measurement of the CMB spectrum and its distortions. We then discuss the theory and measurements of the CMB spectrum and its distortions, the standard μ and y distortions, the details of recombination, the effects of particle decay and annihilation,

alternatives to the Hot Big Bang, tests of cosmic inflation through the Silk damping effects, the effects of the dark energy, other processes, the reionization history, and far IR sources.

In section 3 we discuss high-precision spectrum measurements, outlining the techniques of differential comparison with reference blackbodies, as illustrated by the COBE FIRAS instrument, the COBRA rocket-borne instrument, the ARCADE 2 balloon-borne instrument, and the TRIS ground-based long wavelength measurements. We describe the PIXIE proposed high-precision spectropolarimeter and briefly discuss the DARE mission to search for the effects of the redshifted 21 cm hydrogen line.

The treatment of anisotropy and polarization measurements is somewhat different because there is a companion article describing the instrumentation by Hanany et al. (2012). We briefly review the history of temperature and polarization measurements and discuss the WMAP results, the standard cosmological model, the origin of structure, the geometry of the universe, the matter content of the universe, the age of the universe, the initial conditions from inflation, and parameters beyond the standard model. We discuss the anisotropy and polarization measurement frontiers, the search for non-Gaussianity in the fluctuations, and the search for large angular scale B-mode polarization, small scale anisotropy and polarization, the effects of lensing of the CMB, and the effects of neutrinos on the CMB.

1.2 Modern View

The cosmic microwave background radiation is the measurable relic of nature's greatest particle accelerator, the hot Big Bang, in which the temperatures and densities were so high that all particle species, and possibly all their collective oscillation modes, were in local thermal equilibrium. These particles must include quarks, leptons including the cosmic neutrino background, the Higgs boson, dark matter, supersymmetric particles if they exist, and the carriers of the four known forces: weak and strong nuclear forces, electromagnetism, and gravitation. If the Standard Model of particle physics is correct, then the weak and strong nuclear forces and electromagnetism are all unified in a single description, and all have comparable strength at high-enough temperatures and densities. Pushing back even farther, we can imagine an inflationary period in which a false vacuum filled with a scalar or other fields would decay into the true vacuum we observe today, along with particles and exponential expansion. And perhaps there was an era of quantum gravity in which gravitation was unified with the other three forces, and space and time were themselves quantum phenomena. But as the universe cooled, symmetries were broken many times as structures developed from the primordial material, antimatter was annihilated, and energy liberated from those phase transitions has been added to the electromagnetic fields, now observed at microwave frequencies. As a result, the CMB is now the dominant electromagnetic radiation field in the universe, and its photons far outnumber the baryons. The only other free particles with comparable densities are the unobserved cosmic background neutrinos, and potentially the dark matter particles, whatever they may be.

Of course there are innumerable virtual particles and vacuum fluctuations, whose influence can be measured in the Casimir effect, but whose meaning is not fully appreciated. Also, there may be holographic quantum fluctuations of space-time itself, but that is another topic. And curiously enough, since photons in vacuum are massless, the proper time for their trajectories from the Big Bang to our receivers is exactly zero. (On the other hand, the idea of the photon trajectory is itself a bit fuzzy, since electromagnetic fields are not billiard balls, and there are plasma interactions.)

In the homogeneous and isotropic expanding universe model, the CMB is approximately isotropic in a "preferred rest frame" at each point in space time. More precisely, the dipole term, that is, the lowest spherical harmonic of the distribution of the CMB temperature, is zero. That means that the velocity of the Earth relative to a large sample of the early universe can be observed and explained, but no more fundamental consequence has been recognized. It is also interesting that a substantial velocity of the observer relative to the CMB would change the angular scale of the features, owing to the aberration of light.

1.3 Prediction and Discovery

Prediction. The expanding universe was predicted by Friedman (1922) based on the cosmological equations of Einstein (1917), and independently by Lemaître (1927) who also estimated the Hubble constant from the known observations, and measured by Hubble (1929) using Cepheid variables as distance indicators. But it might or might not have been hot in the beginning, and the Steady State Theory of Hoyle (1948) and Bondi and Gold (1948) requiring replenishment by matter creation might have been correct, so the prediction and discovery of the CMB were hugely important for cosmology. When the expanding universe was first recognized, the distance measurements were seriously incorrect. Hubble's Cepheid variables in the Milky Way were a different type from the ones he found in other galaxies, leading to an expansion age that was significantly less than the ages of stars and even the Solar System, and casting doubt on the whole concept of the Big Bang. The discovery of the CMB did not quite erase all doubt about the hot Big Bang, as there was still the possibility that either a cold Big Bang or a steady state universe would produce starlight that could be absorbed and reemitted by dust grains to fill the universe with microwave background radiation. Also, even into the 1990s, there were questions about the expansion age of the universe relative to the oldest stars. This issue was not resolved until the launch and repair of the Hubble Space Telescope, which enabled more precise measurements of the Hubble constant, detection of the acceleration of the expansion, and better understanding of stellar ages.

Early Unrecognized CMB Measurements. The first known observation that can now be interpreted as a measurement of the CMB was reported very briefly by McKellar (1941), and mentioned by Herzberg (1950), a textbook with a statement that it had only limited significance. The observation of the ultraviolet absorption lines of interstellar CN molecules yielded their rotational excitation temperature, and of course one could imagine many possible ways that the molecules could be excited. Hence, the observation was not pursued at the time.

Alpher and Herman Prediction of Temperature. Alpher and Herman (1948), working with G. Gamow, estimated the temperature of the CMB at 5 K; later they estimated 28 K. They (Alpher, personal communication) tried to convince observers to go look for it, but at that time no serious effort was made, and in any case it would have been extremely difficult with the technology available then. J. Weber wanted to try but was told directly that the measurement was impossible (Weber, personal communication). The Alpher and Herman papers did not emphasize the predicted spectrum of the CMB or compare the spectrum with foreground sources or discuss how it might be detected. Later, radio astronomers and engineers made a number of measurements of the temperature of the dark sky and gave evidence that it was not in their instruments, but none of them were recognized as strong enough evidence or sufficiently surprising to the observers to command attention.

Discovery. The CMB was finally discovered at Bell Telephone Labs by Penzias and Wilson (1965), who were not looking for it but were astronomers testing a new, sensitive, and stable microwave receiver and horn antenna, working at 7.35 cm wavelength. As they were rechecking their measurement, they learned through B. Burke of a group at Princeton who were building equipment to measure the radiation. The Princeton group had been thinking about the bouncing universe, which would be filled with photons left over from previous expansion/contraction cycles. The Bell Labs discovery was published simultaneously with the Princeton interpretation by Dicke et al. (1965) and was front-page news in the NY Times (May 21, 1965). The Princeton group (Roll and Wilkinson 1966) soon completed their measurement at 3.2 cm wavelength, confirming or at least making it plausible that the CMB has the blackbody spectrum required by the hot Big Bang idea.

For a remarkable historical summary of the discovery of the CMB and its properties, the book "Finding the Big Bang" by Peebles et al. (2009) gives the human side of this field as well as an excellent tutorial on the technical aspects.

1.4 Blackbody Form and Dominance

Prediction of Blackbody Form. The idea that the CMB is the remnant of a hot equilibrium phase implies that the spectrum must be very close to a blackbody spectrum, although when examined very closely there must be tiny differences due to the cooling of matter below the CMB temperature (Chluba and Sunyaev 2012a). The blackbody form is preserved exactly through the history of the expanding universe, according to the following simple argument: Imagine a box containing primordial CMB, and imagine that the box expands with the homogeneous and isotropic expanding universe. Then photons crossing the walls of the box are in detailed balance, so we may now replace the imaginary box with a real box of moving mirrors that move with the expanding universe. Within this mirror box, we may represent the electromagnetic field as quanta occupying the spatial and polarization modes of the box. As the box expands, these modes expand adiabatically, and the occupation numbers do not change. The energy of each quantum diminishes as the box expands as well. In combination, these factors imply that the Planck function description of the blackbody is preserved, and the occupation number of each mode is just $1/(e^x - 1)$, where $x = h\nu/kT$. Also, the temperature of the CMB is inversely proportional to the expansion factor of the universe; conversely, $T_{cmb} = T_0(1+z)$, where T_{cmb} is the temperature of the CMB at a time in the past, T_0 is its temperature now, and z is the redshift corresponding to the time in the past. This dependence has been confirmed by observations of the excitation temperature of cyanogen (CN) and other molecules and ions seen in absorption against quasars, and through observations of the Sunyaev-Zel'dovich effect in distant clusters of galaxies.

Dominance and Perfect Spectrum. On a cosmic scale the CMB is extraordinarily bright, even though it has been difficult to measure. Its brightness (σT^4, with $T = 2.72548$ K) is 3.129 μW/m^2. The prediction of the blackbody form is very robust because the photons outnumber the baryons by nine orders of magnitude, and it is very difficult to conceive of any way in which they could have modified the CMB spectrum very much. This difficulty is a matter of perspective and scale – there are many kinds of proposed exotic processes such as explosive events that could have modified the spectrum, as well as four processes that are expected to occur: (i) acoustic damping, (ii) cooling of photons by adiabatically cooling matter, (iii) recombination radiation, and (iv) depending on the mass of the Dark Matter (DM) particle, also DM

annihilation. All of these processes are explained in Chluba and Sunyaev (2012a). The current success of the ΛCDM model has shifted focus from the more radical of these ideas.

Spectrum Turnover. Early measurements of the CMB were made at long wavelengths (more than a few mm) where the Planck function is close to a power law, that might also occur from a nonthermal process, so it was important to observe at shorter wavelengths. Many additional measurements of the CMB spectrum were made from the ground, balloons, rockets, and interstellar molecules, eventually confirming the blackbody turnover at short wavelengths. Until the flight of the Cosmic Background Explorer (COBE) satellite in 1989, reported by Mather et al. (1990), there was evidence that the spectrum was not exactly blackbody, as reported, for example, by Matsumoto et al. (1988), suggesting excess brightness at short wavelengths, but only with limited accuracy. The COBE results were quickly confirmed by the COBRA experiment of Gush et al. (1990). Reasons for the difficulties include: the CMB is faint relative to our 300 K local environment, it is nearly isotropic so that measurements must be absolutely calibrated, receiver sensitivity was barely adequate, atmospheric emission is strong, galactic emission from electrons (free-free scattering and synchrotron) is bright at long wavelengths, galactic dust is bright at short wavelengths, and instruments operated in air cannot be cooled to temperatures comparable to the CMB so that instrument self-emission is strong and absolute calibration is difficult. ❯ *Figure 13-1* shows the original COBE-FIRAS spectrum that showed that the COBE was working well. It is now the iconic figure even though the error bars have been reduced to 50 parts per million by Fixsen et al. (1996); see below for details.

Where Does the Energy Go? The energy density of the CMB and other constituents of the universe decline with the expansion, so where does that energy go? There are a few surprises. First, energy alone is not a conserved quantity in relativity. In special relativity, it is one component of a four-vector, and mass and energy can be interconverted according to $E = mc^2$.
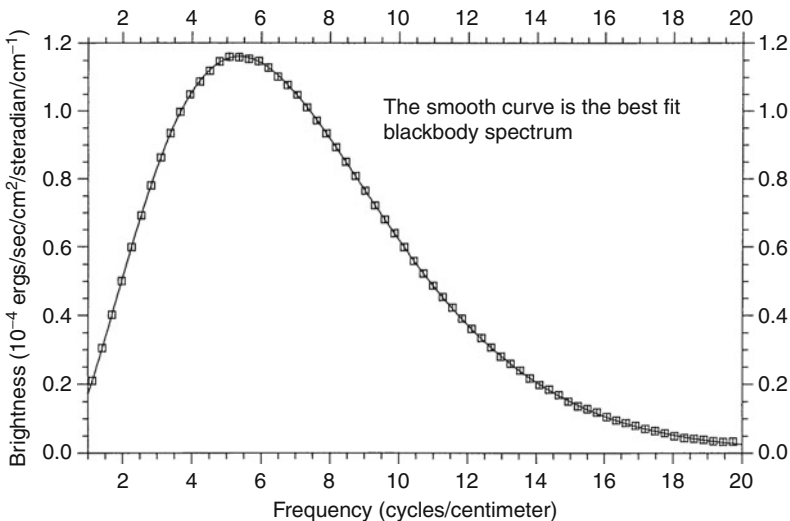
❏ **Fig. 13-1**
Preliminary spectrum of the cosmic microwave background from the FIRAS instrument at the north Galactic pole, compared to a blackbody. *Boxes* are measured points and show the assumed 1% error band. The units for the vertical axis are 10^{-4} ergs s^{-1} cm^{-2} sr^{-1} cm (From Mather et al. (1990))

In general relativity it is only one component of a stress-energy tensor, and in both cases its numerical value changes according to the velocity of the coordinate system in which it is measured. But there are still local conservation laws. Second, the "universe" is not a closed, finite system. In the expanding mirror box described above, the photons inside the box do work on the walls of the box, but when we remove the mirrors and replace the photons with others coming from the other side, there is nothing receiving the work that is being done on the imaginary walls. We conclude that we should trust the differential equations of general relativity but not the simplifications from analogies. There was a reason that cosmology could not be completed with Newtonian mechanics and nineteenth-century thermodynamics.

## 1.5   Celestial Emission at CMB Frequencies

❯ *Figure 13-2* shows the antenna temperature of the sky from 1 to 1,000 GHz for a region at a galactic latitude of roughly $20°$, though the levels one measures can be different by an order of magnitude depending on galactic longitude. The antenna temperature of a gray body is $T_{ant} = \epsilon Tx/(e^x - 1)$, where T is the physical temperature, ϵ is the emissivity, and $x = h\nu/kT$. Ignoring emission from the atmosphere, synchrotron emission dominates celestial emission at the low-frequency end, and dust emission dominates at high frequencies. The basic picture in ❯ *Fig. 13-2* has remained the same for over 30 years (Weiss 1980), though over the past decade, there has been increasing evidence for a new component of celestial emission in the 30 GHz region (e.g., Kogut et al. 1996; de Oliveira-Costa et al. 1997; Leitch et al. 1997). This new component is spatially correlated with dust emission. It has been identified with emission by tiny grains of dust that are spun up to GHz rotation rates by a variety of mechanisms, so-called "spinning dust," though other emission mechanisms may contribute to or produce the signal (Draine and Lazarian 1998, 1999). Understanding this emission source is an active area of investigation.

1.6   Energy Release, Anisotropy, Standard Model, and Polarization

Limits on Early Energy Release. If the CMB spectrum does not match a blackbody form, then significant energy release must have occurred to change it. When the universe was about 1 year old (redshift about 2×10^6), the double-photon Compton scattering processes that create and destroy photons effectively ceased, but multiple Compton scatterings that equilibrate energy between wavelengths were still operating. Hence, if energy were added or removed from the CMB, for instance by the decay of some dark matter particle, then the CMB could have a spectrum with a dimensionless chemical potential μ, and the photon occupation number would equilibrate to the form $1/(e^{x+\mu} - 1)$. (This form is only valid at high frequencies; at low frequencies, μ has to be a function of frequency.) When the universe cooled sufficiently to stop even this equilibration process, it became possible that we would observe a mix of blackbodies at different temperatures, either from a simple mixing or from energy added by Compton scattering from hot electrons. This is described by the Kompaneets parameter y, and the first serious limits were set by the COBE FIRAS instrument. Less than 0.01% of the CMB energy was added after the first year.

Events at and After Decoupling. About 400,000 years later, the universe became fairly quickly (over a period of about 100,000 years) transparent when temperatures reached around
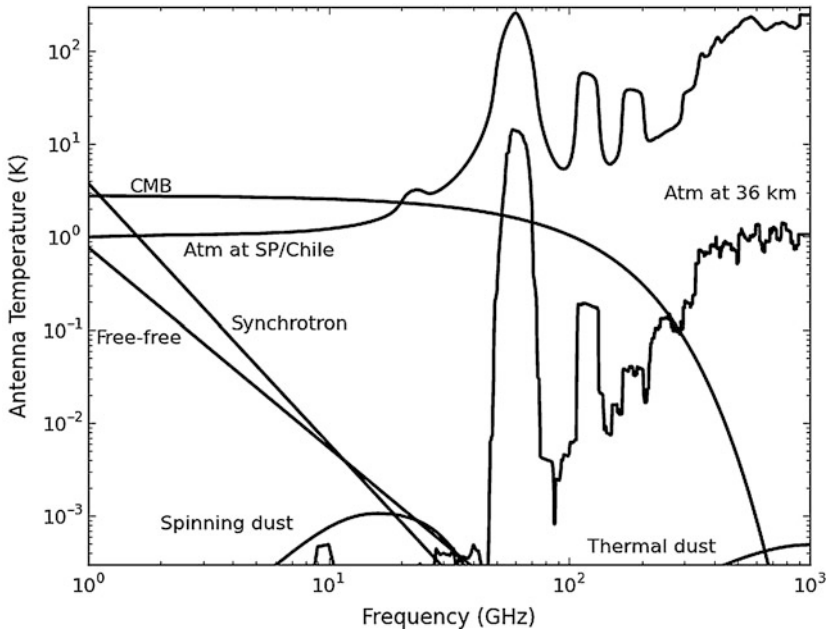
◘ Fig. 13-2

The antenna temperature from 1 to 1,000 GHz for a region of sky near a galactic latitude of roughly 20°. The flat part of the CMB spectrum, roughly below 30 GHz, is called the Rayleigh-Jeans portion. A Rayleigh-Jeans source with frequency-independent emissivity is a *horizontal line* on this plot. The synchrotron emission is from cosmic ray electrons orbiting in galactic magnetic fields and is polarized. Free-free emission is from galactic electrons' "braking radiation" (bremsstrahlung) and is not polarized. The amplitude of the spinning dust is not well known. This particular model comes from Ali-Haïmoud et al. (2009). The standard spinning dust emission is not appreciably polarized. The atmospheric models are based on the ATM code (Pardo et al. 2001) and are for a zenith angle of 45°. The South Pole/Atacama (Chile) spectrum is based on a precipitable water vapor of 0.5 mm. The difference between the two sites is inconsequential for this plot. The atmospheric spectra have been averaged over a 10% bandwidth. The pair of lines at 60 and 120 GHz are the oxygen doublet. The lines at 19 and 180 GHz are vibrational water lines. The finer scale features are from ozone

3,000 K and electrons were bound to atomic nuclei. This moment is known as the decoupling. We observe the map of the CMB predominantly as it was when it was last scattered in our direction. Little effect on the spectrum can be produced by the details of the reactions because as noted above, the photons outnumber the baryons by an enormous factor. But after decoupling, Compton drag on the residual ionization of the baryonic material still limits its ability to move, and, in addition, the baryons can cool adiabatically to have a temperature less than that of the CMB. These effects have tremendous importance to the formation of stars and galaxies, even if we cannot see much effect on the CMB. (Note that although it is often said that we observe the universe at the decoupling, the CMB spectrum is determined by and responds to events back to year one.)

Isotropy. The first test for the cosmic nature of the CMB was that it is isotropic (the same brightness in all directions). If its brightness showed any correlation with known objects such as the weather or the ecliptic plane or the galactic plane or nearby galaxies or clusters, then it would not be cosmic. As it happens, the foregrounds are bright enough to matter, but can be measured at other wavelengths and modeled and extrapolated to find a residual background. For many years, the only results on anisotropy were upper limits, but eventually the Doppler shift due to the Earth's motion relative to the cosmos was measured as a significant dipole. The Doppler-shifted blackbody is still a blackbody but at a modified temperature. We now know the velocity of the Solar System relative to the cosmos as v = 369.0 ± 0.9 km s^{-1} from COBE and WMAP (Hinshaw et al. 2009). The velocity produces a CMB temperature distribution that is to first order $T = T_0(1 + (v/c)\cos\theta)$ where, v is the velocity of motion, and θ is the angle between the observed direction and the direction of motion. The measured velocity is the vector sum of the instrument's velocity around the Earth and the Sun, the Sun's velocity around the center of the Milky Way galaxy, and the Milky Way's velocity relative to the rest of the universe, or more precisely the slice of space-time when the universe became transparent to the photons now reaching our detectors. The masses of nearby galaxies, acting through gravitational attraction over cosmic time, are thought to be enough to explain the motion of the Milky Way and hence the vector sum.

Higher Order Anisotropy. As it happens, the decoupling was soon after a time when baryonic matter was beginning to move under the influence of gravitational forces, now that it was no longer so strongly tied by Compton scattering to the CMB radiation field, and the attenuation of the radiation temperature diminished the gravitational importance and the pressure of the radiation field itself. (Dark matter was free to move much sooner.) On angular scales greater than $7°$, the major feature is the Sachs–Wolfe effect (Sachs and Wolfe 1967), in which some regions of the universe are more dense than others, and photons leaving the dense regions suffer more gravitational redshift than others. It was predicted by Harrison (1970), Peebles and Yu (1970), and Zel'dovich (1972) on very general grounds that the primordial fluctuations should have a scale-free power spectrum, with equal fluctuation amplitudes on all spatial scales. This prediction has been confirmed to excellent precision and extended by the WMAP team and by other anisotropy measurements at small angular scales. In addition, some forms of inflation theory say that the spectral index should not be exactly unity as predicted by Harrison, Peebles and Yu, and Zel'dovich, but a few percent smaller; this has also been has been measured as discussed below.

For smaller angular scales, a detailed analysis of coupled fluids acting before and after the decoupling is necessary. The fluids include the CMB, the cosmic neutrino background, the baryonic matter, the dark matter (cold and/or warm), and the dark energy (affecting the recent expansion history). In a remarkable accomplishment, cosmologists agree very well on the equations to be solved and the methods to be used; this is possible because all the motions are small and the complexity of the modern universe has not yet developed. There is now a "standard model" of cosmology based on cold dark matter with an Einstein Λ constant that matches all of the observations of anisotropy on all measured scales from the quadrupole term ($90°$ angular scale) up to multipole orders of thousands (arcminute scales). This is true despite the tiny amplitude of the fluctuations: a part in 10^5 on $7°$ scales, a part in 10^4 on $1°$ scales.

The remarkable feature found by observations and matched by theory is that there is a preferred angular scale for the fluctuations, called the "acoustic peak," at about $1°$ scale (spherical harmonic order about 200). This is effectively the observed size of the event horizon (and the age of the universe then) at the time of decoupling, and as matter feels the gravitational fields

of primordial perturbations, it begins to move at the decoupling time. More precisely, the event horizon (at the speed of light) is about $1.2°$, and the acoustic horizon is about $0.6°$, smaller because the speed of sound then is about half the speed of light. This acoustic horizon size at decoupling provides a physical scale that is imprinted on the matter distribution and preserved as the universe expands. It can be detected in the galaxy-galaxy correlation function and is the basis for the baryon acoustic oscillation method of measuring the cosmic acceleration, since the apparent size of a physical marker can be measured as a function of redshift. At smaller angular scales, there are approximate harmonics of the fundamental oscillation frequency, and the small-scale oscillations lose amplitude because of photon diffusion, an effect called Silk damping.

Propagation. Note that the intergalactic medium is not perfectly transparent; after decoupling, there is still residual ionization, and then after the first bright UV sources arise, the universe becomes reionized. The optical depth of the intergalactic medium after decoupling has been measured by the correlation of anisotropies and polarization on relatively large angular scales using the WMAP data. According to the WMAP7 data set (Jarosik et al. 2011), the optical depth from here to the decoupling is about $\tau = 0.088 \pm 0.015$, and the reionization redshift was $z = 10.5 \pm 1.2$, assuming the reionization happened quickly.

Lensing. A somewhat surprising result of general relativity is that the distant universe is not where it seems to be, but may be arcminutes away, due to the effect of gravitational lensing of intervening clusters and superclusters of galaxies. The Millennium Simulation yielded a mean deflection angle of $2.4'$ (Carbone et al. 2009). The lensing preserves surface brightness, so might naïvely be expected to have no effect on the CMB and its anisotropy, but this is untrue because the lensing changes the observed angular scales of the fluctuations, magnifying some and shrinking others. Hence, the lensing can be detected statistically against the random fluctuation field of the CMB and used to measure parameters of the mass distribution of the universe. Lensing would not directly affect the polarization of a CMB photon much (because the deflection angles are small), but it does affect the spatial map of the polarization field and sets a limit on the measurement of primordial gravitational waves (see below).

Standard Model. The results of these observations, interpreted through the standard model, have produced a total transformation of the subject of cosmology, from highly speculative to highly quantitative. The parameters of the standard model can be measured with accuracies of the order of a few percent or better and are in agreement with measurements of the accelerating universe obtained in other ways (supernova distance scale, baryon acoustic oscillations, and clustering). On the other hand, some writers believe that warm dark matter may also be required, rather than or in addition to cold. Although the CMB observations are matched essentially perfectly by ΛCDM, the populations and spatial distributions of dwarf galaxies may not match the models so well. This is not simple to model or to observe, as all the complexities of star formation, stellar winds, galactic growth and evolution, black holes, and AGN can influence the comparison of observations with numerical simulations.

Polarization. The new and exciting challenge for CMB observers is to measure the polarization of the CMB. Some large-scale polarizations and correlations with the intensity anisotropy have already been observed by the WMAP team and interpreted to measure the ionization history after the decoupling and the onset of reionization, extending the direct measurements of quasar absorption lines. But the current challenge is to measure the effects of primordial gravitational waves. If such waves were in equipartition equilibrium with other fluctuation events in the early universe, then there should be a statistical signature left. In analogy with electromagnetic fields, the observed polarization vectors of the CMB can be broken down into a curl

part with no divergence (B mode) and a divergence part with no curl (E mode). Primordial gravitational waves, unlike other cosmological perturbations, produce equal amounts of E and B modes. The mode of action is that the gravitational waves, still propagating at the epoch of decoupling, would be stretching and squeezing the primordial fluid so that there is a quadrupole intensity anisotropy at the time of the decoupling. This quadrupole anisotropy, incident on the electrons at last scattering, will result in polarization vector, proportional to two of the five components of the quadrupole term then. We then observe the polarization as a map of the spatial variation of that quadrupole. The predicted signal is very small. Nevertheless, calculation shows that the signal can be measurable, and hundreds of people are working on roughly ten different projects to do it. We cover this topic in more detail below.

2   CMB Spectrum Theory and Measurements

2.1   Major Questions and Spectrum Distortions

In this section we describe three predicted forms of distortion of the CMB spectrum and several effects that could alter the spectrum from the initially perfect pressure-cooker blackbody form. Did the universe really start with a hot Big Bang? Is there any effect of cosmic inflation on the spectrum of the CMB? Did some kind of matter decay or other energy source add energy to the CMB, in such a way that the effect could be seen today? Were there exotic processes like cosmic strings, explosive events, or abundant black holes in the early universe that could modify the CMB spectrum? When all the details about reactions and radiation transfer around the recombination are included, what difference do they make to the general history? Are there observable consequences of the atomic recombination sequences (H, He, He$^+$, Li) or molecules (LiH, H$_2$)? How does the CMB interact with the hyperfine structure of hydrogen, and what could redshifted 21 cm hydrogen emission and absorption tell us? What might make the unresolved excess background radiation seen at cm wavelengths? What is the history of structure formation? The history of reionization? What are the foreground sources, and how can we see past them?

2.2   Bose-Einstein μ Distortion

Wright et al. (1994) and Kogut et al. (2011) summarize the leading models for observable spectral distortions in the context of the FIRAS observations and the proposed PIXIE mission. Energy release within the first year of the expansion would simply be thermalized, without a change from the blackbody form, due to rapid Compton scattering and the double Compton process in which $e + \gamma \longleftrightarrow e + 2\gamma$.

But when the temperature drops sufficiently, this process becomes slow compared to the age of the universe. For redshifts from $z_y = 1.4 \times 10^5$ to $z_{\text{th}} = 2 \times 10^6$, energy added to the CMB field will not be fully thermalized, because the photons are no longer freely created or destroyed, resulting in a Bose-Einstein distribution with a dimensionless chemical potential μ. Electrons still produce Doppler shifts when scattering the photons, and multiple scatterings are enough to produce a pseudoequilibrium form for the photon occupation number: $\eta = 1/(e^{x+\mu} - 1)$. Detailed calculations are reported by Burigana et al. (1991), Daly (1991), and Hu et al. (1994).

In this case the chemical potential $\mu = 1.4\Delta U/U$, where ΔU is the energy added to the CMB and U is its total energy (Sunyaev and Zel'dovich 1970b; Illarionov and Sunyaev 1975a, b).

For wide ranges of ν, it is convenient to let μ be a function of ν, $\mu(\nu)$. Note also that a negative μ could be produced if the electron cloud is colder than the CMB, which can happen as matter cools adiabatically below the CMB temperature. Negative μ would produce a singularity in the brightness temperature of the CMB at zero frequency, but this does not happen because the free-free opacity is large at low frequencies. Chluba and Sunyaev (2012b) show that negative μ would only be produced at redshift $z > 50,000$. Khatri et al. (2011) discussed this in depth and described it as a Bose-Einstein condensation.

2.3 Compton *y* Distortion

At lower redshifts than $z_{th} = 1.4 \times 10^5$, multiple Compton scattering is too slow to produce an equilibrium spectrum. In that case, energy added to the CMB could retain some of its original spectrum. In particular, hot objects would produce additions to the short-wavelength end of the CMB spectrum, even though scattering would prevent observing them. In the absence of discrete hot objects or high energy photons, we consider the effects of scattering from warm electrons, heated above the CMB temperature by some energy source. Doppler shifts from Compton scattering by nonrelativistic electrons effectively produce a CMB spectrum that is a mixture of blackbodies at different temperatures. The resulting spectrum is parameterized by the Kompaneets y, where $y = \Delta U/4U$, and ΔU and U are the total energy release and the total energy, as before,

$$y = \int \frac{k(T_e - T_{cmb})}{m_e c^2} d\tau, \tag{13.1}$$

where T_e is the electron temperature, T_{cmb} is the CMB temperature at the time, and τ is the optical depth to electron scattering. A modification is required if the electrons are relativistic (Wright 1979) because individual scatterings can shift photons far into the short wavelength Wien tail of the spectrum.

2.4 Recombination Details

An obvious question is whether the details of the recombination process at the time of decoupling can produce a measurable effect on the anisotropy or spectrum of the CMB. The short answer is no because there are 10^9 photons per baryon. However, the scattering optical depth of the hydrogen and helium transitions to and from the ground state is also extremely large, so there is a calculable delay in recombination, a slightly nonequilibrium distribution of populations of the levels, and a small trace of the hydrogen lines in the CMB spectrum. Peebles (1968a) discussed the Lyman α line emission, and as did Zel'dovich et al. (1969), Varshalovich and Khersonskii (1977), and Dubrovich and Stolyarov (1995). Dubrovich (1975) was the first to mention recombination lines at high n. An H atom in the $n = 2$ state faces a bottleneck in reaching the ground level: either it decays by a two-photon path or it emits a Lyman α photon that must escape an optically thick cloud. This trapping means that each atom can produce many residual photons resulting from transitions among the excited states, leading to an amplification of the spectrum distortions, but they are still too small to observe directly now.

On the other hand, at 2 GHz, the fractional distortion may be as large as 2×10^{-7}, and on the Wien end of the spectrum, the fractional distortion is large and affects the chemistry calculations at low redshfits (e.g., Switzer and Hirata 2005; Coppola et al. 2012a).

Detailed computer simulations have now been done, keeping track of the reaction rates and the populations of individual atomic, ionic, and molecular states of H, He, and Li. Key recent papers include Seager et al. (1999, 2011), Chluba and Sunyaev (2006), Rubiño-Martín et al. (2008), Sunyaev and Chluba (2009), and Chluba and Sunyaev (2012b). Switzer and Hirata (2008) discussed primordial helium recombination, Ali-Haïmoud and Hirata (2011) described the HyRec code for hydrogen and helium recombination, and Alizadeh and Hirata (2011) discuss the effects of possible molecular H_2 at the recombination era ($z = 800 - 1,200$). Coppola et al. (2012b) review prior work back to 1983 and discuss a detailed analysis of the reaction rates and effects of the formation of molecular hydrogen H_2. Peak production rates would occur around redshift $z = 100$, and the rotational-vibrational transitions would emit radiation peaking around 2 µm wavelength.

The predicted spectral distortion from all of these factors is very small but not necessarily unobservable, now that technology and concepts have improved. The Lyman series of spectral lines are the strongest but are broad, and the contrast against the continuum is of order 10^{-8}. The Lyman α line is redshifted to around 130 µm, where Galactic and zodiacal dust emission are bright, and atomic and molecular transitions in the interstellar medium of the Milky Way and external galaxies would confuse the search for the recombination line.

The electron gas cools adiabatically far below the CMB temperature when it is no longer strongly coupled (thermally and kinematically) to the CMB, but this event occurs around a redshift $z = 150$, and of course the optical depth is then also small. Galli et al. (2008) report that the "delayed recombination" has important effects in determining cosmological parameters from the WMAP data, but would be less important when smaller angular scale data are included. Peebles et al. (2000) demonstrated the effect for the first time and gave it the name.

2.5 Free-Free Distortion

At long wavelengths the free-free opacity after decoupling is significant and can either cool or heat the CMB depending on whether the electrons have been cooled or heated. Chluba and Sunyaev (2012b) included this effect in their numerical simulations. For the case of cooled electrons, they find spectral distortions similar to a negative y at high frequencies, created at late times, and a negative μ at low frequencies (1 GHz), created well before recombination ($z > 50,000$).

2.6 Particle Decay and Annihilating Particles

As noted by Wright et al. (1994), rare photons with $h\nu \gg m_e c^2 / \tau_H$ would lose most of their energy by multiple Compton scattering and deliver their energy to the electron gas, which would then modify the spectrum of the CMB photons. In this formula, τ_H is the optical depth for electron scattering per Hubble time. Such photons must be rare; otherwise, we would have seen a large distortion of the CMB spectrum. The photons could come from the decay of rare particles or from the decay of common particles with small branching ratios. For instance, Fukugita and Kawasaki (1990) considered the decay of massive (20 keV) neutrinos at $z \approx 4,000$, which would produce a y distortion.

Some theories have posited that ordinary matter or dark matter may be slightly unstable. In the standard model of particle physics, baryon number is conserved, and the proton is the lightest baryon, so it must be stable. Observational limits on its lifetime are greater than about 10^{34} years. On the other hand, baryogenesis and the asymmetry between matter and antimatter are not understood, and some theories predict that protons are unstable. Also, since we do not know what particles comprise dark matter, perhaps it is the decay product of some other particles that might have had interesting lifetimes. A lifetime of one year corresponds to the time at which the CMB spectrum could begin to deviate from a blackbody form.

The dark matter might be neutralinos (supersymmetric partners of photons), which arise naturally in supersymmetry theories; there may be four neutralinos, of which only the lightest would be stable. The primordial supersymmetric particles, most of which are charged, could not be stable or we would still see them. Instead, annihilation of these charginos by their antiparticles would produce electromagnetic energy and neutralinos as dark matter. If dark matter particles are massive, then they would have cooled to low temperatures during the adiabatic expansion of the universe. If all the dark matter particles were produced in the first year of expansion, we would not see an effect on the CMB. But if they were produced later, and the energy could be coupled to the electromagnetic fields, then the CMB spectrum would be distorted.

Silk and Stebbins (1983), prior to the COBE launch, and later McDonald et al. (2001) reviewed some of the possibilities. According to de Vega and Sanchez (2010), CMB spectrum distortions would be most sensitive to neutralinos at a mass scale below 80 keV. Feng et al. (2003) computed the possible spectrum distortions as a function of particle lifetimes and electromagnetic energy release for two different particle models. They considered gravitinos (the supersymmetric partners of gravitons) as the dark matter and produced graphs illustrating the range of parameter space tested by CMB spectrum distortions. They show a range of the possible WIMP lifetime from 10^4 to 10^{12} s and a range of their energy release parameter ζ_{EM} from 10^{-12} to 10^{-7}.

Particles could also be annihilated by meeting their antiparticles, producing similar effects on the CMB spectrum. The CMB constraints on this process are already strong (Galli et al. 2008), as are those from the Fermi observatory, so predicted μ values are only a few times 10^{-9}.

2.7 Alternatives to the Hot Big Bang

Cold Big Bang. The current inflationary picture of the early universe provides a cold starting point, with a single scalar field rolling down into a potential well, and then radiating photons and other particles at extreme temperatures. But a more literal meaning, prior to the concept of inflation, held that the expanding universe was cold even after the particles were produced. If such a cold universe were unstable, then it could break up into clusters, galaxies, and stars, which would then liberate photons and dust, and then the dust would convert visible light into CMB. Lemaître (1931), immediately following the translation of his 1927 article, considered the instability of the early universe, as did Eddington and others. In those times there was also a theory that the cosmic rays are relics of the great explosion. Zel'dovich (1963) suggested that a zero-temperature early universe would undergo a phase transition and would then break up into condensations of planetary mass.

Layzer and Hively (1973) argued that the CMB could be produced in a cold Big Bang Model, if most of the matter in the universe were included in a population of stars at redshift 25–50.

The dust grains produced in these stars would thermalize the energy released by nuclear burning and supernova explosions. Aguirre (1999) reviewed the possibility of nucleosynthesis in such a cold Big Bang. He argues that the element abundances can be explained by a cold Big Bang and leaves open the question of whether the CMB could be astrophysically generated. His later paper Aguirre (2000) discusses the CMB and concludes that even with generous assumptions, the cold Big Bang idea is probably not correct.

Steady State Theory. The Steady State Theory held that the CMB (which had not been predicted by the theory) would be the accumulated, redshifted, thermalized radiation of all the stars. To achieve a steady state, it was necessary to posit an unobserved process of matter creation, to keep the mean density of the universe constant through time. The theory did not predict that the CMB should have a blackbody spectrum, and it also held that the temperature of the CMB should be independent of redshift, in conflict with observations of CN, CH, and [C II] lines in distant objects. Attempts to rescue the Steady State Theory in light of new data were increasingly ad hoc and required selective belief in certain observations and not others.

In both the Cold Big Bang and the Steady State theories, the optical depth and special optical properties of dust that would be needed to thermalize the CMB to the precise blackbody form would be quite unusual. Wright (1982) computed the properties of iron whiskers and outlined the tests to be made when a more precise spectrum of the CMB could be determined. But now that the CMB is known to have a precise blackbody form, the Cold Big Bang and the Steady State theories no longer match the data.

Of course, the radiation field produced by all the generations of stars, black holes, etc., and partially thermalized by dust does exist. It was measured at both near- and far-infrared wavelengths by the DIRBE team and is comparable in luminosity to all the visible classes of stars and galaxies. But it does not have a blackbody spectrum with emissivity near unity, as the CMB does.

2.8 Tests of Cosmic Inflation: Silk Damping

Do the primordial density fluctuations follow the power-law spectrum that has been tested so far by anisotropy measurements, and is its index different from the scale-invariant value? Below we discuss this in the context of direct measurements of the anisotropy. However, it is also possible to test this on small scales by searching for energy release at redshifts greater than 10^4, which would result in a distorted CMB spectrum. Primordial density fluctuations are frozen in place as the early universe inflates, and then come back into the horizon as expansion slows. As the smaller scale fluctuations come into view, the photons associated with them diffuse, the anisotropy is erased, and their energy can be converted to heat (Silk damping, Silk 1968; Sunyaev and Zel'dovich 1970b; Daly 1991; Hu et al. 1994). This effect is already taken into account in the prediction of anisotropies, but the effect on the spectrum would be too small to have been detected so far. The effect becomes a test of inflation because it is sensitive to primordial fluctuations on scales much smaller than those observable as CMB anisotropies. If those fluctuations were significantly stronger than the approximately scale-invariant prediction of inflation, then we would know from this measurement. Both y and μ distortions could be produced, depending on the physical scale at which the fluctuations deviate from the inflation prediction.

The limit set by the FIRAS instrument (below, Wright et al. (1994)) gives $|\mu| < 3.3 \times 10^{-4}$ (95% confidence). With this limit, the power law spectrum index of the fluctuations is less than

$1 + 6/7 \approx 1.9$. This result limits the fluctuations on scales much smaller than are accessible from the anisotropy measurements. PIXIE (see below) could do more than 4 orders of magnitude better, down to μ of 10^{-8}.

For later energy release, the first-order effect of Silk damping on the spectrum is again to mix together blackbodies at a range of temperatures, and $2y = \text{var}(T)/T^2$, where var() is the variance. Note that because this is quadratic, the y resulting from the measured anisotropy of 10^{-4} is only 5×10^{-9} and not yet measurable. On the other hand, future precise measurements will have to account for this effect. For earlier energy release between z_y and z_{th}, the spectrum equilibrates to the Bose-Einstein form with $\mu = 2.8\,\text{var}(T)/T^2$, also not yet detectable.

Chluba et al. (2012b) compute the effects of Silk damping of primordial acoustic waves, carrying the computations to second order in the perturbation amplitude and in the energy transfer. The acoustic energy can raise the temperature of the CMB (which we cannot distinguish from other effects) or it can cause both y and μ distortions. The μ distortion is particularly interesting because it occurs early. Future measurements of μ can set limits on the primordial fluctuations at scale sizes k from 50 to $10^4\,\text{Mpc}^{-1}$, even though these fluctuations are completely erased from the anisotropy and baryon distributions. Chluba et al. (2012a) show explicitly how powerful measurements of the CMB spectrum could be and that the COBE-FIRAS limit is already stronger than the primordial black hole limits.

2.9 Dark Energy

The cosmic acceleration has no predicted direct effect on the CMB except through modifying the expansion itself, and the CMB blackbody form is preserved. On the other hand, the details of the expansion history are critically important to the calculation of the anisotropy and its relation to present-day large-scale structure. The basic Sachs–Wolfe effect produces the primary anisotropies observed on large angular scales; dense regions cause gravitational redshifts of photons leaving them at decoupling. The integrated Sachs–Wolfe effect refers to the effect of the changing depth of the gravitational potential wells as the universe expands and dilutes the material and depends on whether the source of the gravitational potential includes radiation as well as matter.

2.10 Other Processes

Wright et al. (1994) summarize other exotic processes that might have occurred. Ostriker and Cowie (1981) considered an explosive scenario for galaxy formation; this is now ruled out as a general explanation. Gnedin and Ostriker (1992) considered massive black hole accretion and photodisintegration of He, but this is also ruled out. Cosmic strings have been ruled out as a primary source of the general anisotropy, and consequently, it is unlikely that there could be a direct effect on the CMB spectrum through energy release from the strings. On the other hand, a search for the spatial signature (anisotropy) of cosmic strings continues to be an active research area as better maps are obtained. Energy release by superconducting strings was considered by Ostriker and Thompson (1987) and Tashiro et al. (2012), and magnetic fields were discussed by Jedamzik et al. (2000).

2.11 Reionization History and the X-ray Background

The reionization of the intergalactic medium, presumably by UV from discrete sources such as the first stars and AGN, was accompanied by energy delivered to the CMB through the Compton scattering of the newly freed electrons. The reionization energy of about 10 eV per electron is small compared with the CMB energy of $2(1+z)$ MeV per electron, for $\Omega_B h^2 = 0.0125$ (Wright et al. 1994). The electrons left after decoupling, or produced by reionization, will be cooled fairly quickly by Compton processes until $z = 5$. If they are produced later, they might be relativistic and the CMB distortion need not follow a simple y form.

The hot electrons producing the X-ray background can be isotropically but not uniformly distributed; otherwise, they would produce a measurable distortion of the CMB spectrum. The FIRAS limit was that a hot IGM produces less than 10^{-4} of the X-ray background and conversely that the X-ray background comes from material with a filling factor less than 10^{-4}.

The Sunyaev–Zel'dovich (Sunyaev and Zel'dovich 1970a) effect is the result of Compton scattering by hot gas in clusters of galaxies and has now been observed directly as hot spots in the sky maps (at short wavelengths) and cold spots at long wavelengths. With enough precision, it should be possible to observe the cumulative effect of these clusters on the mean sky spectrum and to determine whether the cluster population explains the whole distortion seen.

2.12 Far-IR Background Sources

It is expected that AGN and star-forming galaxies would have produced significant far-infrared fluxes from dust emission and that if this occurred at a high enough redshift, it might add to the CMB spectrum in a way that would be hard to recognize. In total the far-IR background measured by the COBE DIRBE and FIRAS instruments is comparable in brightness to all the known categories of visible and near-IR sources so that of order 1/3 of the total (post-recombination) luminosity of the universe is in the far-IR. The measured far IR background has been partially resolved into discrete sources, particularly ULIRGs at modest redshift ($z = 1 - 2$). This is an active field of study using data from the ISO, Spitzer, and Herschel space observatories, the BLAST instrument, far-IR cameras on large ground-based telescopes, and submillimeter interferometers.

3 High-Precision Spectrum Measurements

The history of the measurements of the CMB spectrum is full of challenges and mistakes, later overcome by clever design, diligent pursuit of systematic errors, and careful measurement of foreground sources of radiation that might be mistaken for CMB. When the CMB was first predicted in 1948, a measurement had already been made by Dicke's group at MIT, producing an upper limit of 20 K, but no connection to the prediction was made at the time. Wright (2012) gives an online tutorial and argues that Dicke might have been able to discover the CMB if he had tried. But by the time Penzias and Wilson were hunting for excess noise in their system, receiver sensitivity had advanced orders of magnitude, enough that the extra 3 K they saw was a significant part of the equipment sensitivity. In addition, they knew that the full sensitivity

◘ **Table 13-1**

Summary of spectrum distortion parameter limits, with 95% confidence, or 2 σ. COBRA, FIRAS, and PIXIE report y, ARCADE 2 and TRIS report Y_{ff}. The proposed PIXIE mission would have sensitivity to measure many predicted spectrum distortions

Name	Freq. (GHz)	Y_{ff} or y	μ or $|\mu|$
COBRA (Gush et al. 1990)	90–480	0.002	0.008
FIRAS (Fixsen et al. 1996)	60–630	$-1 \pm 7 \times 10^{-6}$	$-1 \pm 4 \times 10^{-5}$
ARCADE 2 (Seiffert et al. 2011)	3–90	$<1 \times 10^{-4}$	$<6 \times 10^{-4}$
TRIS (Gervasi et al. 2008)	0.6–2.5	$[-6.3, -12.6] \times 10^{-6}$	$<6 \times 10^{-5}$
PIXIE (Kogut et al. 2011)	30–6,000	2×10^{-9}	10^{-8}

they wanted for telecommunication and astronomy would require an excellent antenna with very low sidelobes (response to signals from directions outside the main beam of the antenna). Also, scientific research projects now demanded liquid helium, which could be purchased commercially, so it was possible to design a calibration process that would compare the sky with a reference body at a low temperature. Finally, they were well aware that the Milky Way galaxy is bright and that the atmosphere might emit radiation, so they knew that they should measure these effects. All of these advances were crucial to their discovery and to the confirmation by the Princeton group months later.

In this section we first describe the foregrounds that obstruct precise measurements of the CMB spectrum and then describe the precise measurements already completed and the preparations now being made for even better measurements. Key projects include the COBE-FIRAS; its immediate confirmation by a similar but brief COBRA rocket experiment by H. Gush et al. and a balloon payload (ARCADE, Absolute Radiometer for Cosmology, Astrophysics, and Diffuse Emission) that has already flown to measure the cm-wave spectrum precisely; and the TRIS ground-based measurement at 0.6, 0.82, and 2.5 GHz. We discuss a proposed satellite mission (PIXIE, Primordial Inflation Explorer) that in principle could measure the CMB spectrum, anisotropy, and polarization and briefly describe the DARE (Dark Ages Radio Explorer), a proposed lunar satellite to search for redshifted 21 cm HI radiation that can be seen as spectral fluctuations of the CMB. We conclude with a discussion of the ultimate limits to CMB spectrum measurements.

We summarize the main results of the precise spectrum measurements in ❷ *Table 13-1*.

3.1 Minimizing Foregrounds

There are both diffuse and discrete foreground sources that limit the accuracy of CMB measurements. Excellent summaries have been published by both the WMAP (Gold et al. 2011; Bennett et al. 2003a) and Planck science teams (Planck Collaboration et al. 2011a and 25 additional articles in a dedicated journal issue), primarily addressing the effects on anisotropy measurements. Neither WMAP nor Planck measures absolute brightness, and hence both are insensitive to potential isotropic foreground radiation sources. Below, we discuss the Earth and its atmosphere, the Solar System, and Galactic electrons, dust, atoms, ions, and molecules.

3.1.1   Earth and Atmosphere

Terrestrial instrumentation must be protected from the brightness of the Earth, occupying 2π sr of solid angle immediately under the equipment. Typically the shield is made of reflective material but has a residual emissivity itself, which must be measured by for instance changing its temperature, varying the angles of incidence, etc.

In addition, the primary antenna must be made with extremely low sidelobes, and ideally those sidelobes must be mapped as a function of direction, polarization, and frequency. Many designs have been used. The Bell Labs antenna was called a Hogg horn, combining a very large pyramidal horn antenna with an off-axis parabolic reflector operating at $45°$ incidence to make a pattern with low response toward the ground. Other ground-based and low-altitude equipment has typically used much smaller horns with scrupulous attention to detailed design and test. One successful design uses a corrugated circular horn. These antennas have the advantage that the beam pattern is nearly Gaussian and nearly independent of polarization.
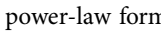
Above that is the atmosphere, which has a temperature gradient with altitude, moving invisible clouds of water vapor and visible clouds of water droplets or ice crystals. In mountain areas, the stratification of the atmosphere is not necessarily plane parallel, due to the wind blowing over the topography. The atmosphere also has complex chemistry, including the possible presence of water-vapor dimers that produce a continuum opacity. The primary atmospheric opacity at wavelengths where we wish to measure the CMB is due to water vapor, and there are also oxygen lines at 60 and 120 GHz and many submillimeter lines of ozone. There are excellent models for all of these except the water vapor dimers. Measuring and compensating for the atmospheric emission and opacity was critically important for ground-based measurements of the CMB spectrum. The primary technique is to measure the dependence of the measured CMB temperature on zenith angle.

3.1.2   Solar System

The diffuse zodiacal dust in the solar system, originating from the collisions of asteroids and comets with each other, is not bright at CMB wavelengths but can be detected. Its spatial distribution is concentrated in the ecliptic plane, but the cloud is thick and the contrast from ecliptic pole to ecliptic plane (at $90°$ elongation) is only about 1:3. According to theory and confirmed by measurements with the DIRBE instrument on the COBE mission, the dust density falls off with distance from the Sun as a power law $\rho \propto r^{-\alpha}$, where $\alpha = 1.34$ (Kelsall et al. 1998). The far-IR spectrum of the zodiacal dust was reported by Fixsen and Dwek (2002), based on the FIRAS and DIRBE observations. At wavelengths longer than 150 μm, the dust appears to have an emissivity proportional to ν^2, as expected from the Kramers-Kronig relations and causality, for dust grains significantly smaller than the wavelength, sufficiently hot, and not spinning.
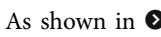
In any case, little can be done currently to avoid this foreground emission, as it is difficult and expensive to put the observatory outside the zodiacal dust cloud. But in the future, missions to the outer solar system will become more feasible, propelled by ion engines and powered by more efficient radio-thermal generators, nuclear reactors, or even huge solar collectors.

3.1.3 Galactic Electrons

Galactic electrons collide with protons to produce free-free (bremsstrahlung) radiation and orbit in magnetic fields to produce synchrotron radiation. Both have spatial structure that is highly concentrated toward the Galactic plane and the Galactic center, and both follow approximate power-law spectra because the underlying electron energy spectra also have nearly power-law form. As shown in ❯ *Fig. 13-2*, below about 1 GHz, the synchrotron radiation is brighter than the CMB, and below about 0.5 GHz the free-free emission is also. We estimate the contribution of these sources to the CMB spectrum by mapping the entire sky at longer wavelengths, where the electrons are dominant, and predicting the maps at higher frequencies. There are subtleties related to deviations from simple power-law behavior, variations of the power-law indices, and the effects of discrete sources and polarization on the modeling. In addition, differences between the angular resolution and sidelobe response of the antennas used at different frequencies must be modeled. Considering all these complexities, precise experiments are designed to have a wide range of wavelengths with the same antenna pattern at all wavelengths. The WMAP team reported that the spectrum steepens between 20 and 40 GHz, consistent with steeper spectrum synchrotron sources, or with spinning dust like models (Gold et al. 2011). They conclude that masking out the bright regions of the Galaxy leaves negligible contribution to the CMB anisotropy or polarization. Similar methods could be used to subtract Galactic foregrounds from future high-precision CMB spectrum measurements like PIXIE.

Early results from the Planck mission confirm the WMAP result that the Galactic emission is not fully represented by the simple models of free-free, synchrotron, and dust emission. For example, there is a widely extended residual "haze" around the galactic center. Maps of the haze resemble the maps of gamma-ray bubbles observed with the Fermi mission. Hooper and Linden (2011) consider the possibility that dark matter annihilation produces the haze. In any case, it is likely that the electron spectrum does not have the same power-law index everywhere, and indeed nature does not require it to be a power law at all. This is an active research area for radio astronomers as well as cosmologists.

3.1.4 Galactic Dust

As shown in ❯ *Fig. 13-2*, at wavelengths less than about 0.5 mm ($v > 600$ GHz), the thermal emission from interstellar dust grains is brighter than the CMB. Although interstellar dust grains cannot be easily collected, evidence suggests that there are many different kinds, shapes, sizes, and compositions and that they are not all at the same temperature even within a single cloud of dust and gas. Their properties evolve with time as they are sputtered by cosmic rays, or are heated in shocks or grain-grain collisions or near approaches to hot stars, or serve as condensation nuclei in cold gas clouds. Moreover, the grains can be aligned by magnetic fields, as we know from the polarization of starlight and scattered starlight, and therefore can emit partially polarized far-infrared radiation. In addition, the smallest grains can spin at frequencies of 10–100 GHz. They rotate because they absorb and scatter light preferentially from locations away from the center of mass, and their rotation rates are limited by their mechanical strength. They are also struck occasionally by high-energy atoms and cosmic rays (Draine and Lazarian 1998, 1999).

The nonspinning dust emission is typically represented by a power-law emissivity modifying a Planck function: $I_\nu \propto \nu^\beta B_\nu(T)$, with $\beta \approx 1.8$, not far from the Kramers-Kronig limit of 2. However, this effective index may simply approximate the sum of dust populations at different temperatures. The fitted temperatures range from 10 to over 20 K, depending on direction, and sometimes more than one component is required for a single direction.

3.1.5 Galactic Atoms, Ions, and Molecules

Only a few species of Galactic atoms, ions, and molecules emit strongly enough to be detectable (so far) in the wide bandwidths needed to measure the spectrum of the CMB. These are CO (up to the 8–7 line), [C I] at 370 and 690 μm, [C II] at 158 μm, [N II] at 122 and 205 μm, [O I] at 146 μm, and CH at 116 μm (Fixsen et al. 1999). They also found the 269 μm line of H_2O in absorption against the Galactic center. The CO lines are dominant cooling lines for cold clouds, and the [C II] line emits about 0.3% (Wright et al. 1991) of the dust luminosity of the Milky Way, so they are of great interest for astrophysics. Because these lines are concentrated in the Galactic plane and in molecular clouds, they have not limited the accuracy of CMB spectrum measurements. On the other hand, the CO lines appear in the passbands of some instruments designed to measure CMB anisotropy.

The lines also provide frequency calibration standards for CMB spectrometers. From these calibrations and the known values of the Planck and Boltzmann constants, it was possible to confirm and improve the thermometric accuracy of the COBE FIRAS.

3.2 COBE FIRAS

The most precise (50 parts per million) measurement of the CMB spectrum yet accomplished was made with the FIRAS (Far Infrared Absolute Spectrophotometer) on the COBE satellite (Fixsen et al. 1996). The COBE (Boggess et al. 1992) was launched Nov. 18, 1989 from Vandenberg Air Force Base near Lompoc, California. It still orbits 900 km above the Earth in a polar (94° inclination) Sun-synchronous orbit so that the orbit plane precesses at 1 rotation/year to remain approximately perpendicular to the line to the Sun. The COBE carries three instruments, all protected by a conical shield. The COBE was oriented so that the Sun was always a few degrees below the plane of the top of the shield, so the instruments were well protected. However, for about 2 months per year, the Earth limb rose slightly above the shield plane for about 20 min out of each 103 min orbit. A higher altitude orbit could have avoided this situation but would have caused higher rates of Van Allen belt particle bombardment. The FIRAS and DIRBE (Diffuse InfraRed Background Experiment) instruments were cooled to about 1.5 K inside a liquid helium cryostat. The third instrument, DMR (Differential Microwave Radiometers), was mounted around the circumference of the cryostat and inside the shield.

3.2.1 FIRAS Design

The FIRAS was sensitive to wavelengths from 100 μm to 1 cm, including the peak emission of the CMB around 2 mm, the Wien tail of the distribution for $\lambda < 1$ mm, and strong emission

from the interstellar dust. The instrument was based on the design of the balloon-borne spectrometer flown by UC Berkeley in the mid-1970s (Woody et al. 1975; Woody and Richards 1979). The instrument is a rapid-scan, symmetrical polarizing Fourier transform spectrometer with two inputs and two outputs, using the Martin and Puplett (1970) concept. The $7°$ instrument beam is defined by a Winston cone, a quasi-optical compound parabolic concentrator (Winston 1970). The orbit and orientation of the spacecraft meant that the spin axis and FIRAS line of sight were approximately $94°$ from the Sun at all times and so swept out an approximately great circle as the satellite orbited the Earth. The circle moved with the Sun so that over the course of 6 months, the beam scanned the entire sky, and in the 10 month duration of the liquid helium, about 60% of the sky was observed at intervals 6 months apart. The Winston cone attaches smoothly to an apodizing section, flared like a trumpet bell. Calibration was provided by a full-beam external blackbody that could be moved into the antenna, where it sealed the aperture. The interferometer mirrors were scanned smoothly in a sawtooth pattern, producing a time-dependent intensity at each detector, and there were two stroke lengths and two stroke speeds that could be chosen by command. The interferometer functions as a modulator that compares two inputs, one from the sky (or external calibrator) and one from an internal reference body. Each output of the instrument is split by a dichroic beamsplitter into short and long wavelength bands, separated at $\lambda = 0.5$ mm, so that there are four detectors altogether. Combining the two scan speeds, the two stroke lengths, the two sides, and the two wavelength bands, there are altogether 16 independent data sets (❯ *Figs. 13-3* and ❯ *13-4*).
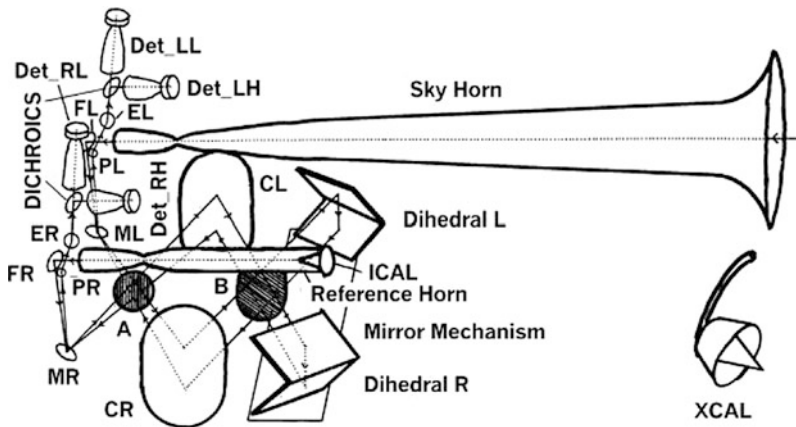
◼ **Fig. 13-3**

Drawing of the FIRAS instrument. Light enters the sky horn from the sky or the XCAL and the reference horn from the ICAL. After reflection from the folding flats (FL, FR), it bounces off the mirrors (ML, MR) and is analyzed by the polarizer (A). The collimator mirrors (CL, CR) recollimate the light before it is split by a second polarizer (B) at 45°. It is then reflected by the dihedral mirrors, with different paths set by the mirror mechanism. After reflection, the light retraverses the beam splitter, collimator mirrors, and analyzer. This time it is intercepted by the pickoff mirrors (PL, PR), which direct it into the elliptical mirrors (EL, ER), the dichroic filters, and, finally, the detectors (DetLH, DetLL, DetRH, DetRL)
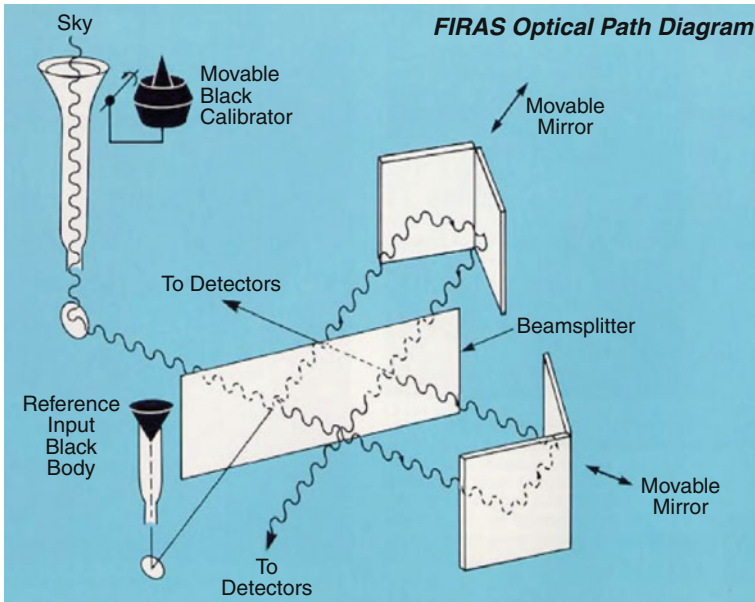
▣ **Fig. 13-4**
FIRAS calibration concept. The actual FIRAS used two wire grid polarizers with wires at 45°. The external calibrator nearly sealed the horn antenna when in place. The internal reference body was adjusted to nearly null the sky interferogram. Both horns and both blackbodies were controllable from about 2 to 20 K

3.2.2 FIRAS Detectors and Data Processing

The four detectors were composite bolometers, with noise equivalent powers of the order of $NEP = 4 \times 10^{-15}$ W/Hz$^{1/2}$. Each used a doped silicon thermometer chip, bonded to a large but thin diamond octagon, blackened with a thin film of bismuth, and all suspended by taut Kevlar fibers. Each was DC biased through a large resistor, and the signal was amplified by a heated JFET to feed the signal out the long coax cable to the warm electronics. The JFET was suspended inside a radiation-tight box on Kevlar fibers so that it could operate near its optimum temperature of about 60 K. The sensitivity was limited by charged particle impacts, which were very common in certain parts of the orbit near the horns of the Van Allen belts around the Earth's poles, and in the South Atlantic Anomaly, where the radiation belts are especially near to the Earth.

Data processing began with sorting the interferograms into groups according to observing mode, temperature settings of the horns and calibrators, detector bias, and line of sight. Then, interferograms were compared to optimally detect the impulses from cosmic rays, and these signatures were iteratively removed by a least squares fitting program.
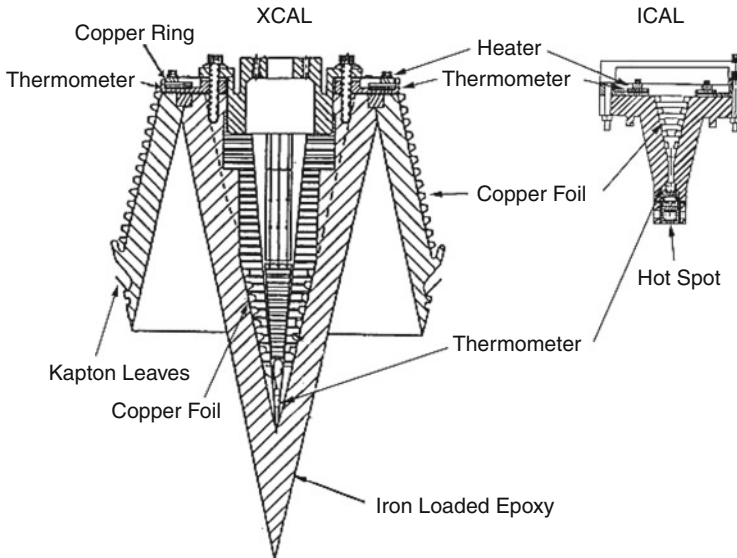
3.2.3 FIRAS Calibration

The operation of FIRAS in the vacuum and cold of outer space enables a nearly ideal configuration for comparison of the sky with a full-beam blackbody. If the calibrator body is perfectly black and isothermal, and there is no change of the instrument signal when the body is inserted

or removed from the beam, then the sky also has a perfect blackbody spectrum, regardless of the imperfections or calibration factors of the instrument or the uncertainty of the thermometer calibration. To reduce the dynamic range of the instrument, the internal reference body was adjusted to nearly null the modulated interferogram by setting its temperature close to the sky temperature. To be more quantitative, temperature controllers were provided to regulate the temperatures of the external calibrator and the internal reference body and of the Winston cone (sky horn) and its counterpart facing the internal reference body.

The calibration (Fixsen et al. 1996) was designed to measure the parameters of an instrument model that included the emissivities of the Winston cone (sky horn), the similar but smaller horn (reference horn) receiving signals from the internal reference body, the emissivity of the reference body, and systematic and temporary errors in thermometry. Although all the thermometers were calibrated to mK accuracy before installation, there was evidence that the calibrations were somewhat incorrect in flight. Fortunately, the thermometer errors do not limit the determination of whether the sky has a blackbody spectrum, but they do limit the accuracy of the determination of the absolute temperature. There were also small residual errors in the calibration data sets that showed that the mirror transport mechanism (MTM) was vibrating as it moved, as was known before launch, and that some light was making more than one pass through the interferometer, yielding the appearance of harmonic response. Models were made for these effects, and their parameters were determined from the data. In the end, there was a single calibration model representing all the observing modes and all the detectors, with a full covariance matrix for the errors (❯ *Fig. 13-5*).

The accuracy of the calibrator body is critical, and the design is reported by Mather et al. (1999). It is made of Eccosorb CR-110, cast in the form of a reentrant cone, like a trumpet

▣ Fig. 13-5
Cross section of the FIRAS calibrators. The XCAL is 140 mm in diameter, and the ICAL is 60 mm in diameter. Heaters and thermometers are indicated on the drawing. The Hot Spot heater was designed to null a high-frequency excess in the CMBR. No excess was seen, but the Hot Spot is part of the reason the ICAL has a reflectance of ~4%

mute. This is an epoxy loaded with iron powder to increase its permeability and absorption of microwaves; in this case it was also mixed with a fine silica powder to make it thixotropic (to resist the settling of the iron powder during casting). The calibrator material is cast onto a corrugated copper foil to control its temperature and make it as isothermal as possible. The support arm and the top of the calibrator are wrapped with multilayer insulation to protect against radiant heat flow from the warm rim of the sunshield.

There are several ways in which the calibrator could be imperfect. First, it could be partially reflective so that emission (or lack thereof) from parts of the spectrometer that are not at the same temperature would change the effective input. Since the spectrometer includes parts at many temperatures, this was the main worry. The relevant parts include the detectors, the mirrors, the beamsplitters, the horns, and the internal reference body, as well as the surrounding chamber. Only the horns and the internal reference body could be actively controlled. The effective reflectance of the calibrator in the horn was made as low as possible and was estimated to be less than 10^{-5}, depending on frequency. It was also measured with a value of -55.8 ± 1.5 dB at 33.4 GHz. When the calibrator is in the FIRAS horn, any ray reflected from the calibrator will bounce from the horn surface many times and almost always return to the calibrator for another chance to be absorbed, so the effective reflectivity of the calibrator in the horn is much lower than the actual reflectivity. (The other absorbers in this cavity are the aluminum horn and the exit port to the spectrometer.) Other potential errors include partial transparency of the calibrator material, allowing leakage from the insulated outer surface, which was slightly illuminated at some angles by rays from the solar shield around the cryostat. This effect, if important, would be maximum at the longest wavelengths, where the calibrator material had the least absorptivity, but no sign of a problem was seen. A third potential effect would be leakage through the gap between the calibrator and the horn. To control this leakage, two sets of aluminized Kapton leaflets were installed around the circumference of the calibrator, to make a direct optical seal of the gap, without transmitting any heat in case the calibrator and horn were at different temperatures. Measurements were made of the calibration signal as a function of the position of the calibrator in the horn, and no effect was seen until the calibrator had been moved about 12 mm. A fourth effect would be if the calibrator were not isothermal. In this case, it would emit a spectrum like the cosmic y distortion and enable a real cosmic y distortion to escape notice. However, the measured temperature gradients, and the known thermal conductivity, together with models of the potential heat flows, show this to be negligible on the scale of the FIRAS sensitivity.

Fixsen et al. (1996) and Fixsen (2009) developed alternate ways to redetermine the temperature scale. The wavelength scale of the FIRAS was determined precisely using the atomic and molecular spectrum lines of the Galaxy and used to cross-check the observations of the temperature dependence of the calibration signals. Also, the spectrum of the dipole anisotropy of the CMB as measured by FIRAS has its own spectral form (the derivative of the Planck function with respect to temperature) and can be used to determine yet another estimate of the monopole temperature. Fortunately, all these measurements are consistent at the level of 1 mK. Finally, the FIRAS results can be recalibrated using the WMAP dipole.

3.2.4 Foreground Removal for FIRAS

At the wavelengths observed by FIRAS, the main foreground is the dust emission from the Galaxy, concentrated in the Galactic plane. An adequate (in the sense of good χ^2) model for the dust emission in most lines of sight is a product of a power-law emissivity as a function of frequency and a Planck function for a single temperature. However, in the Galactic plane where

the dust is bright, there were many regions where this was not an adequate fit, and two or even three components at different temperatures were required. At high Galactic latitudes, the dust is too faint to measure in most individual lines of sight, so a smoothed Galactic model was used to fit the data. The smoothed model was not quite proportional to the cosecant of the Galactic latitude.

The spectrum lines of the interstellar atoms, ions, and molecules had a negligible effect on the measurement of the CMB spectrum because they are either faint, concentrated in the Galactic plane and Galactic center, or at frequencies well above the CMB frequencies. The [C II] line at 158 μm is so bright that it produces a recognizable cosine curve in the raw interferograms of the Galactic plane.

### 3.2.5 Limits on CMB Spectrum Distortion

Least squares fits to the FIRAS data produced the limits in Fixsen et al. (1996). The fitted parameters are correlated because the y and μ distortion spectra are not orthogonal to the derivative of the Planck function with respect to temperature $\partial B/\partial T$ or to the model spectra for the interstellar dust. In addition, the calibration model parameters are themselves correlated. The results were $|\mu| < 10^{-5}$ and $|y| < 15 \times 10^{-6}$, 95% confidence, including systematic errors. The RMS deviation between the measured spectrum and the blackbody is less than 50 parts per million of the peak brightness.

The most precise measurement of the CMB temperature was reported by Fixsen (2009), giving the value T_{cmb} = 2.72548 ± 0.00057 K, based on recalibration of the FIRAS data in comparison with the WMAP data, and other published data. This precise value is important for comparison with measurements at different wavelengths.

Fixsen et al. (1997) showed that the spatial fluctuations of the CMB as observed by the FIRAS instrument on a 7° scale have a thermal spectrum (actually, the derivative of the Planck function with respect to temperature), as they should if they are really temperature fluctuations. Stated another way, the FIRAS, an absolute instrument, detects the CMB anisotropy. The data also limit rms fluctuations in the Compton y parameter, observable via the Sunyaev–Zel'dovich effect, to $\Delta y < 3 \times 10^{-6}$ (95% CL) on 7° angular scales.

3.3 COBRA Rocket Experiment

The COBRA rocket instrument of Gush et al. (1990) was launched for the fifth time on Jan. 20, 1990, just 2 months after the launch of COBE. Built at the University of British Columbia, it included a rapid-scan Fourier transform spectrometer very similar in concept to the COBE FIRAS instrument, but using a dielectric beamsplitter instead of the polarizing configuration. In its 9 min of flight, it obtained excellent quality data, using a much colder detector (0.29 K) than the FIRAS to gain far higher sensitivity. In its short flight, there was no time or space to move an external calibrator body into the beam, so the instrument was calibrated on the ground before launch, using an external calibrator with emissivity >0.999. There was also no time to scan the sky or make a map. Nevertheless, it was immensely important that this instrument also observed the blackbody and that its measured temperature (2.736 ± 0.017 K) agreed well with the FIRAS result. (There was still the possibility that the FIRAS thermometers were not correctly calibrated.) The reported 95% confidence limits on y and μ were 0.001 and 0.008, respectively (❯ *Fig. 13-6*).
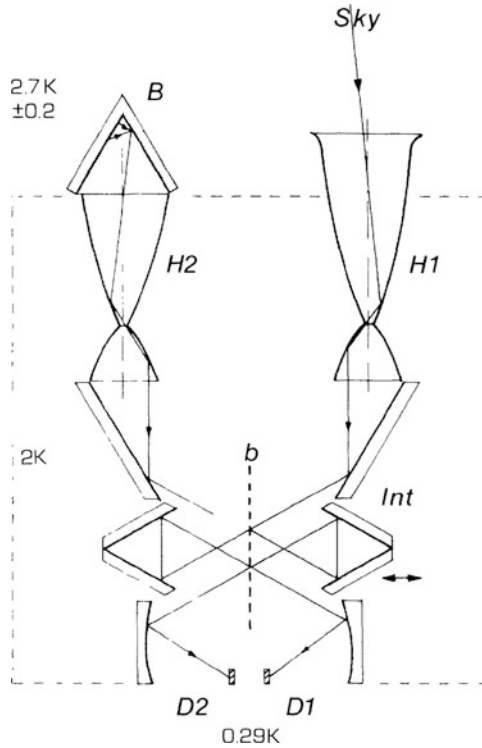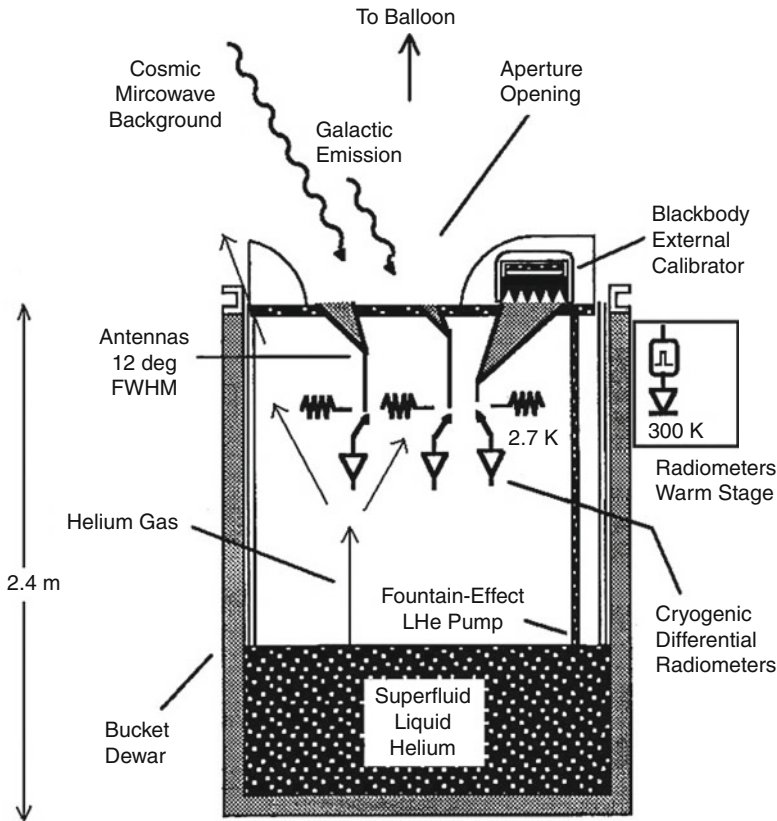
◼ Fig. 13-6
COBRA design of Gush et al. (1990) showing the principle of the apparatus. H1 and H2 are similar horn-type telescopes of 6° field of view. H1 receives radiation from the sky, whereas H2 is illuminated by a blackbody simulator B. Radiation issuing from the horns enters a two-beam interferometer (Int), with a beam splitter at b, from whence it emerges to be focused on two bolometric detectors, D1 and D2. As the path difference in the interferometer is changed, the signal generated by each detector (interferogram) is proportional to the *difference* in intensity of the sky and the blackbody. The numbers indicate temperatures of various sections of the spectrometer. One challenge of the design was making a reference load whose temperature could be changed reliably during the brief rocket flight.

3.4 ARCADE 2

The ARCADE 2 instrument (Absolute Radiometer for Cosmology, Astrophysics, and Diffuse Emission, described by Singal et al. (2011)) is the most ambitious yet built for measurement of the CMB spectrum at wavelengths out to 10 cm (3 GHz). It is a balloon-borne microwave radiometer with six frequencies (3, 5, 8, 10, 30, and 90 GHz), a double-nulled design with internal reference bodies and an external calibrator, and is completely windowless to enable all the radiometrically active parts to be cooled to 2.7 K. It extends the FIRAS concept as far as possible to long wavelengths, given the size and atmospheric constraints of balloon payloads. To improve on ARCADE 2 will require a redesigned top surface area or a space mission.

The key discovery that enables this design is that it is possible to achieve adequate flow velocities for gaseous helium, escaping in a controlled way from a 1,900 liter cryostat, to keep the

◼ Fig. 13-7

ARCADE 2 instrument schematic, components not to scale, as described by Singal et al. (2011). Cryogenic radiometers compare the sky to an external blackbody calibrator. The antennas and external calibrator are maintained near 2.7 K at the mouth of an open bucket dewar; there are no windows or other warm objects between the antenna and the sky. Cold temperatures are maintained at the *top* of the dewar via boil-off helium gas and tanks filled with liquid helium fed by superfluid pumps in the bath. For observing the sky, everything shown is suspended below a high-altitude balloon

atmosphere from condensing on the apparatus. Scale models of the aperture were built to simulate the flow on the ground, and in-flight cameras confirmed success. In addition, superfluid fountain-effect pumps lifted up to 55 l/min of superfluid helium to the top of the apparatus, to keep it cold. This is a remarkable feature of engineering that enables nearly ideal calibration to be performed. Although the calibrators are in flowing gaseous helium, they can reach the desired temperature of 2.725 K. The details and variations of heat flow and temperature gradients in the calibrator bodies are then the limiting factors for calibration accuracy (❯ *Fig. 13-7*).

The ARCADE 2 used corrugated circular antenna feeds to produce 11.6° FWHM Gaussian beams. In addition, it carried a 4° beam antenna at 30 GHz for useful cross-checks. All observed at 30° from the zenith, away from the balloon and the payload suspension (parachute, ladder, truck plate, and FAA transmitter). The beam profile of one of the horns was measured and

agreed extremely well with the theoretical predictions; it is almost independent of frequency within each observing band. The calculated radiometric effects of the balloon and suspension ranged from 2.3 to 42 mK, depending on frequency band.

The radiometers all used cryogenic HEMT amplifiers, which set the system sensitivity, followed by coax or waveguide links to warm amplifiers. The input to each cryogenic HEMT was switched to alternate between sky and reference load using a MEMS switch at 3 and 5 GHz and a latching ferrite waveguide switch for the higher frequency channels. The cold loads were in coax at the 3 and 5 GHz bands, and were made of steelcast wedges in waveguide for the other channels. The warm amplifiers were followed by frequency filters that divided each band into two parts, low and high, for improved spectral information.

3.4.1 ARCADE 2 Calibration

The critically important external calibrator was moved from one receiver aperture to another, so all shared the same thermometry and almost the same thermal environment, just as for the COBE-FIRAS. A precursor calibrator is described by Kogut et al. (2004) and the actual device by Fixsen et al. (2006). The calibrator surface was made from 298 sharp cones of steelcast, each 88 mm long and 35 mm in diameter, cast onto an aluminum core for thermal control. The measured reflectance of the calibrator ranged from −42.4 dB at 3 GHz to −62.7 dB at 10 GHz. These reflectances are so low that they are not a significant source of error. The harder problem is thermal gradient control, considering the flowing gaseous helium and the superfluid helium pumps. The measured thermal gradient from tip to base of the cones is 600 mK, but 98% of it occurs near the tip and involves only 3% of the absorber. The calculated calibrator emission was based on the measured thermal gradients, the known absorption properties of the material, and the known field distribution of the antenna pattern. There are systematic differences in heat flow according to the position of the calibrator over the different receiver apertures, but these were measured with many sensors. The calibration accuracy of ARCADE 2 could be improved up to an order of magnitude, by providing active control of the temperature of the top plate, to near 2.7 K instead of the 1.4 K achieved in the last flight.

3.4.2 ARCADE 2 Results

Seiffert et al. (2011) report the final results from the ARCADE 2 instrument after accounting for all calibration issues and the Galactic foreground. They find 2σ limits on the spectral distortion of $\mu < 6 \times 10^{-4}$ and $|Y_{ff}| < 1 \times 10^{-4}$. They also find that there is a residual signal that significantly exceeds the models of all known galactic and extragalactic sources. It has a power-law spectrum with amplitude 18.4 ± 2.1 K at 0.31 GHz and a spectral index of -2.57 ± 0.05 (❯ *Fig. 13-8*).

Vernstrom et al. (2011) consider the extragalactic source population in detail and conclude that their model does not explain the ARCADE 2 results. Seiffert et al. (2011) had suggested that there might be a population of sub-μJy sources down to 10 nJy at 1.4 GHz that add up to enough, and it might be possible if high z star-forming galaxies have a higher radio-to-far-IR ratio than local ones. Radio observations at greater depth than yet obtained could be made with the Expanded Very Large Array (EVLA) and the ALMA.
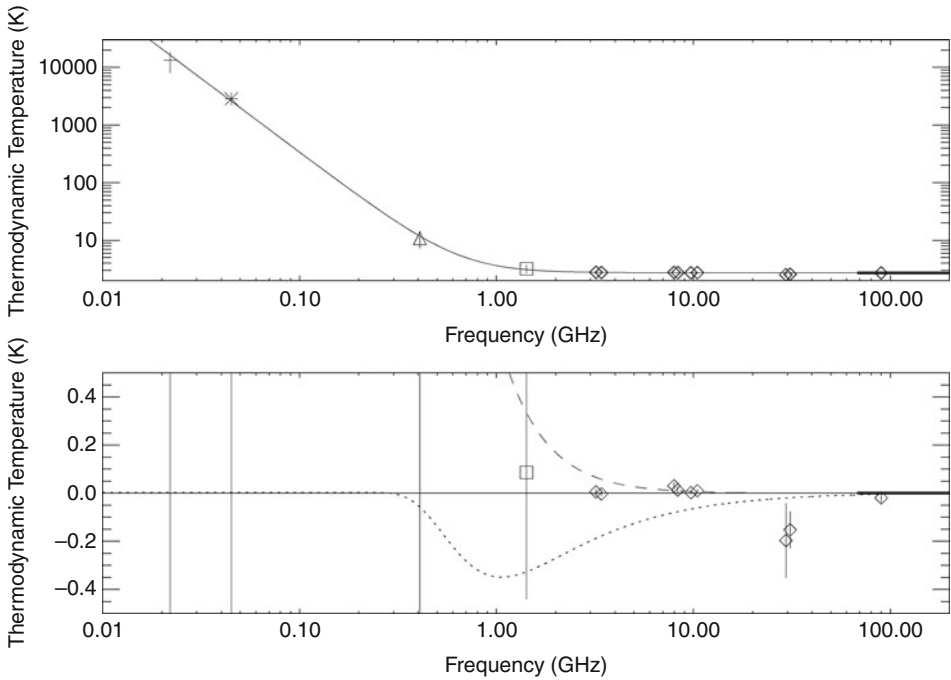
⬛ Fig. 13-8

ARCADE 2 results as described by Seiffert et al. (2011). Fit of ARCADE 2 data, FIRAS data, and data from low-frequency radio surveys. The *upper plot* shows (*solid line*) a fit with three components: a frequency- independent CMB contribution, a power-law amplitude, and a power-law index. The *lower plot* shows the fit residuals. The *dotted line* shows the expected shape of a μ distortion. The amplitude of the plotted distortion is 50 times the upper limit determined from FIRAS. The *dashed line* shows the shape of a Y_{ff} distortion with an amplitude equal to the 2σ upper limit. The addition of either a μ distortion or a Y_{ff} distortion as a free parameter is not supported by the data. Data points are from Roger et al. (1999), cross; Maeda et al. (1999), *asterisk*; Haslam et al. (1981), *triangle*; Reich and Reich (1986), *square*; ARCADE 2 (*diamonds*); and FIRAS (*heavy line*), corrected for Galactic emission and an estimate of extragalactic radio sources, as shown in Table 1 of Seiffert et al. (2011)

3.5 TRIS

Gervasi et al. (2008) report on the ground-based TRIS experiment (Zannoni et al. 2008), which improved the uncertainty of measurements at frequencies of 0.60 and 0.82 GHz by factors of 9 and 7, respectively, and agreed with prior measurements at 2.5 GHz. The improvements were obtained through better absolute calibration and better modeling of the Galactic foregrounds. The TRIS operated primarily by doing drift scans while pointed at the zenith. Absolute calibration was obtained using a cryogenic front end of each receiver, with a triple-throw switch to connect the receiver to the sky, a cold load (CL) near 4 K, or a warm load (WL) near 270 K (❯ *Fig. 13-9*).

The results for the spectrum distortion parameters were $-6.3 \times 10^{-6} < Y_{ff} < 12.6 \times 10^{-6}$ and $|\mu| < 6 \times 10^{-5}$, both at the 95% confidence level.
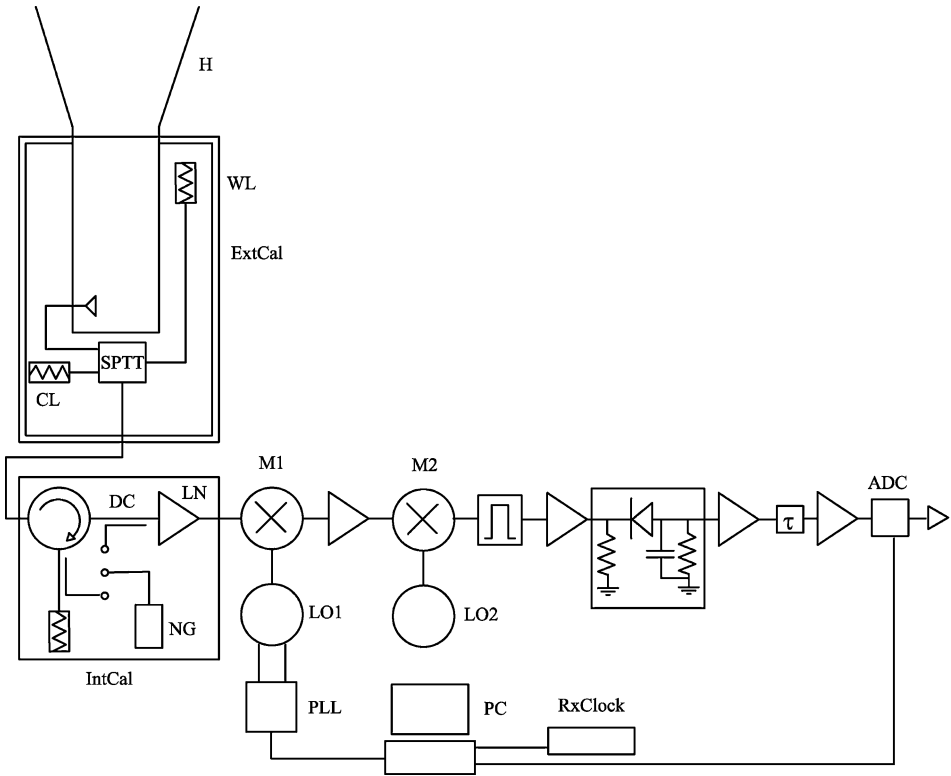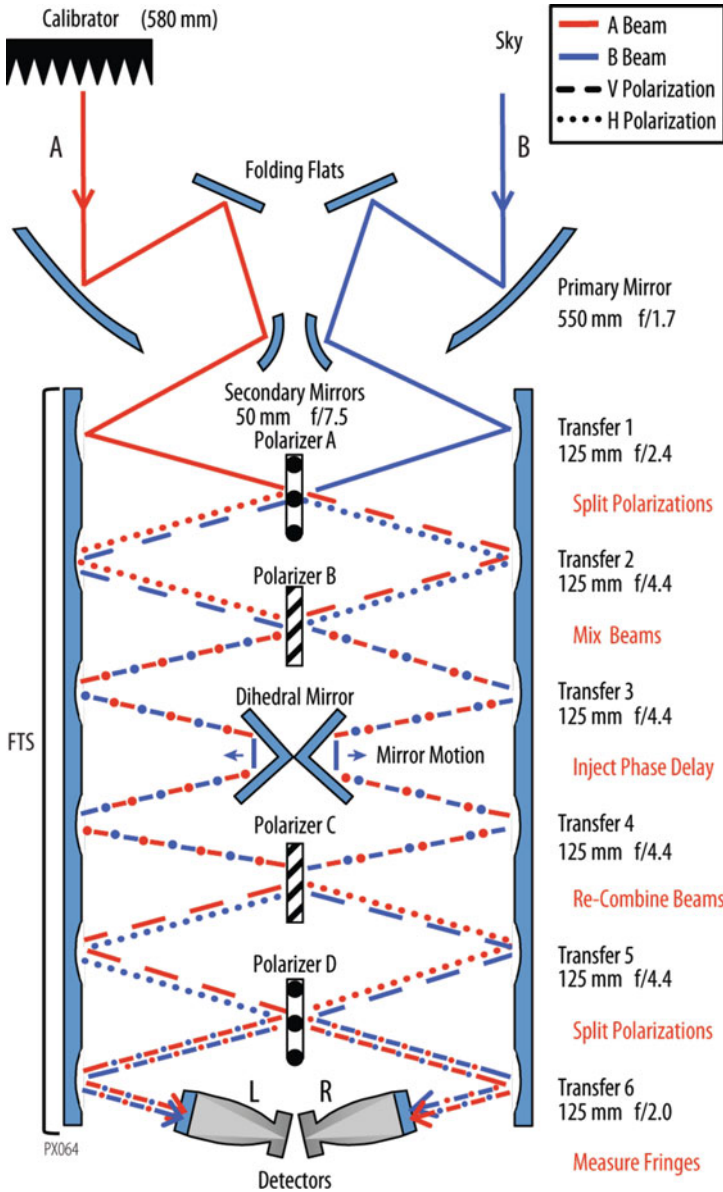
◼ Fig. 13-9

Block diagram of TRIS radiometers. *H* corrugated horn, *LN* low-noise amplifier, *LO1, LO2* local oscillators, *M1, M2* mixers, *PLL* phase-locked loop, τ system time constant; *ADC* analog-to-digital converter, *PC* personal computer, *RxClock* radio clock, *ExtCal* external calibrator (*WL* warm load, *CL* cold load, *SPTT* switch), *IntCal* internal calibrator (*C* circulator, *DC* directional coupler, *NG* noise generator)

3.6 PIXIE

The proposed Primordial Inflation Explorer (PIXIE) is a nulling polarimeter for cosmic microwave background observations as described by Kogut et al. (2011). It improves on the FIRAS in several ways, and it is able to measure the polarization and anisotropy of the CMB as well as its spectrum. It is fully symmetrical, unlike the FIRAS, and either of the two inputs can observe the sky or a full-beam reference blackbody. It would cover the range from 30 GHz to 6 THz (1 cm–50 μm wavelength) in 400 spectral channels and could map the Stokes *I*, *Q*, and *U* parameters over the whole sky. While the primary objective in today's context is the search for the polarization signature of primordial gravitational waves, the ability to test the CMB monopole spectrum against a blackbody is remarkable (❱ *Fig. 13-10*).

Improvements over the FIRAS concept include the use of 550 mm-diameter primary reflectors to define the beams on the sky, instead of the quasi-optical Winston cone used by the FIRAS. The PIXIE design preserves the polarization sensitivity, which was intentionally ignored in the
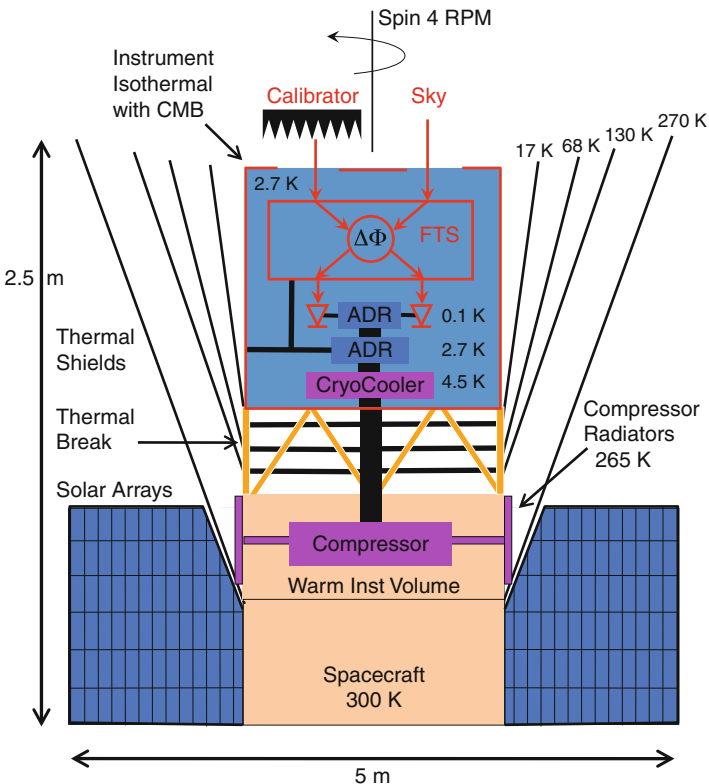
■ Fig. 13-10
Schematic view of the PIXIE optical signal path. As the dihedral mirrors move, the detectors measure a fringe pattern proportional to the Fourier transform of the difference spectrum between orthogonal polarization states from the two input beams (Stokes Q in instrument coordinates). A full-aperture blackbody calibrator can move to block either input beam or be stowed to allow both beams to view the same patch of sky

FIRAS. Each output is split into two polarization states following a square concentrator in front of the detectors so that there are four detectors in total. The beam size is smaller (2.6° top hat) than the FIRAS (7°) and is optimized for the low-order peak in the primeval B-mode polarization spectrum. Other instruments, many on the ground or balloons, appear capable of detecting the higher order polarization peak. But a full characterization of the low-order ($\ell < 20$) B-mode peak requires full sky coverage and a space mission. The étendue ($A\Omega = 4\,cm^2$ sr) is much larger than for FIRAS ($1.5\,cm^2$ sr), enabling good performance at longer wavelengths. The individual detector sensitivity is almost two orders of magnitude better (7×10^{-17} vs. 4×10^{-15} W Hz$^{-1/2}$), based on the use of lower detector temperature (0.1 K instead of 1.4 K). In addition, the entire instrument (except the detectors) is cooled to the mean temperature of the CMB (2.725 K) so that emissions and reflections within the instrument do not produce modulated signals. Finally, the PIXIE would be cooled by active refrigerators (a mechanical cryo-cooler and staged adiabatic demagnetization refrigerators), as well as passive radiators, so that its much-longer (4 year) lifetime is not limited by stored cryogens (▶ *Fig. 13-11*).

◼ **Fig. 13-11**

Cryogenic layout for the PIXIE instrument. An ADR and mechanical cryo-cooler maintain the instrument and enclosure at 2.725 K, isothermal with the CMB. A set of concentric shields surrounds the instrument to prevent heating by the Sun or Earth. Approximate dimensions of the deployed observatory are indicated

The entire PIXIE observatory would spin at 4 rpm, much faster than the COBE (0.8 rpm), for rapid modulation of the polarization in the shorter time that it takes for the line of sight to move one beamwidth across the sky. The orbit altitude (660 km) is lower than for COBE (900 km), reducing the cosmic ray rates on the detectors.

The predicted PIXIE sensitivity for polarization is 70 nK per $1°$ square pixel, corresponding to multipole orders up to about 200. Averaged over the best 75% of the sky, it would have a sensitivity of 3 nK for the B-mode polarization signal, well under the 30 nK predicted from large-field inflation models, and comparable to the predicted noise floor from gravitational lensing of the CMB. For the spectrum distortions, after accounting for foreground removal, the predicted PIXIE sensitivity is μ of 10^{-8} or y of 2×10^{-9}. For comparison, the FIRAS limits were $|\mu| < 10^{-5}$ and $|y| < 15 \times 10^{-6}$, 95% confidence, including systematic errors. So the PIXIE would have a distortion sensitivity of three to four orders of magnitude better, opening up many possibilities for tests or detections of unexpected cosmic phenomena.

3.7 DARE

The Dark Ages Radio Explorer (DARE, Burns et al. 2012) is a proposed space mission to measure the very long wavelength spectrum of the CMB with enough precision to detect the variations due to the redshifted 21 cm hydrogen line. Since the galactic synchrotron and free-free emissions all have smooth power-law spectra, deviations from those forms would be meaningful. Operating in the 40–120 MHz range, the mission would be sensitive to hydrogen at redshifts from 11 to 35. To obtain a quiet-enough environment, the instrument would orbit the Moon and would observe when it is protected from both the Sun and the Earth. The predicted spectrum distortions range from +30 mK around 100 MHz from the Hot-Bubble-dominated epoch, to −110 mK around 65 MHz due to accreting black holes. Instrument calibration at these low frequencies is done with noise diodes, and the antennas are short dipoles and hence very nondirectional. The predicted spectral features are relatively narrow (10%) so that they would be recognizable even in the presence of strong Galactic emission.

3.8 Ultimate Limits

The PIXIE instrument pushes the limits of what will be possible, as its estimated sensitivity is 3–4 orders of magnitude better than the COBE FIRAS. Measurements to detect the spectral distortions from the individual recombination lines at decoupling would require parts per billion sensitivity, but on the other hand, a template for all of them together might be more easily recognizable. It might well be possible to achieve adequate raw sensitivity with an advanced mission, but at this level every foreground component will be bright, including molecules with narrow spectral features. Is the Planck function correct? The calibration data for the FIRAS instrument and the proposed PIXIE instrument could be used to test it very well. Note that the cosmological results do not require a precise verification of the Planck formula; all they require is that the sky and the blackbody calibrator must match.

## 4 Historical Overview of Temperature and Polarization Anisotropy

The cosmic microwave background (CMB) radiation was detected by Penzias and Wilson (1965). After its discovery, a small number of experimentalists worked for years to better characterize the CMB as they searched for temperature fluctuations. It is uncommon that the beginning, emergence, and maturation of a scientific field can be seen so clearly. The anisotropy was discovered nearly 20 years ago (Smoot et al. 1992). In that time, the temperature power spectrum has been mapped out through eight acoustic peaks, the best-fit cosmological model identified, and the polarization anisotropy (an independent check of the model, in this case) measured to high accuracy. As of this writing, we await the release of the Planck data. In the following, we briefly review the set of measurements that got us to where we are, summarize the current state of the data and its interpretation, and then indicate some future promising directions. In a separate contribution, Hanany et al. (2012), CMB instrumentation is discussed, so that is not included here.

4.1 Anisotropy Searches Prior to COBE

One of the primary reasons for believing that the Penzias and Wilson discovery was cosmological in origin was that the radiation was isotropic. Immediately, one wanted to know "how isotropic is it?" The instrumentation for measuring anisotropy is quite different than that used for the absolute temperature measurements. The first dedicated instrument was the Wilkinson and Partridge (1967) "isotropometer." The instrument had a beam width of $5.5°$ at a frequency of $9.4\,\text{GHz}$ and was used to set an upper limit of $3.2\,\text{mK}$ on the dipole amplitude at a declination of $-8°$, and a limit on smaller-scale anisotropy of $\sqrt{\ell(\ell+1)C_\ell/2\pi} < 2{,}700\,\mu\text{K}$ at $\ell \sim 10$. Given estimates of galaxy peculiar velocities, it was apparent early on (Peebles and Wilkinson 1968; Bracewell and Conklin 1968) that a dipole term should exist at an amplitude of roughly $3\,\text{mK}$. This term tells us our velocity with respect to a cosmic reference frame. The first measurement of the dipole, consistent with the modern value and direction (3.358 ± 0.017 in direction $\alpha = 11.19^h$ at $\delta = -6.9°$), was made by Ned Conklin from White Mountain in California (Conklin 1969), although there were lingering doubts about the accounting of foreground emission (Webster 1974). Clearer detections were later reported by Corey and Wilkinson (1976) and Smoot et al. (1977).

This velocity dipole, or "aether drift," was the first CMB anisotropy observed. However, it was clear that if cosmic structure grew from the Big Bang, then it had to leave an imprint as anisotropy in the CMB. The magnitude of the anisotropy was uncertain. The expansion rate, geometry, and composition of the universe were all poorly known. It was not clear just how large the foreground signals were relative to the anisotropy or if the reionization of the universe erased the anisotropy en route.

Before COBE, there were over 30 different experiments, including the RELIKT satellite mission, aimed at searching for the anisotropy, as detailed in Peebles et al. (2009). Many experiments yielded multiple observations in different configurations. The search took place over a range of angular scales and at many frequencies. As the bounds tightened, theories of structure formation evolved. There was a remarkable and steady advance that drove the development of new detector technologies: masers, heterodyne systems, bolometers, and new ways of observing the cosmos. Observations were made from balloons, airplanes, and on the ground from Saskatoon, Canada to the South Pole. At last, in 1992, almost 30 years after the discovery of the CMB, the anisotropy was discovered by the DMR instrument aboard the
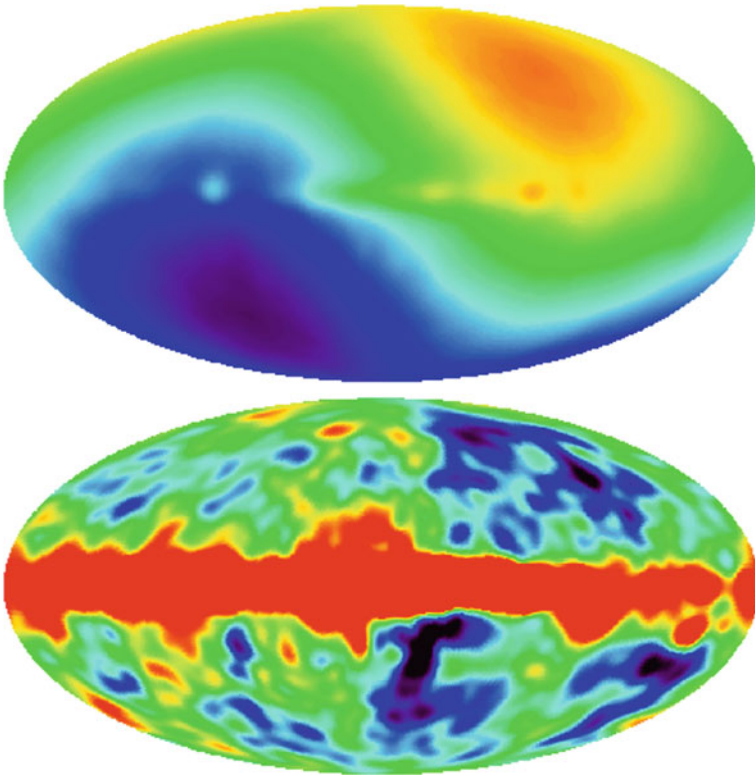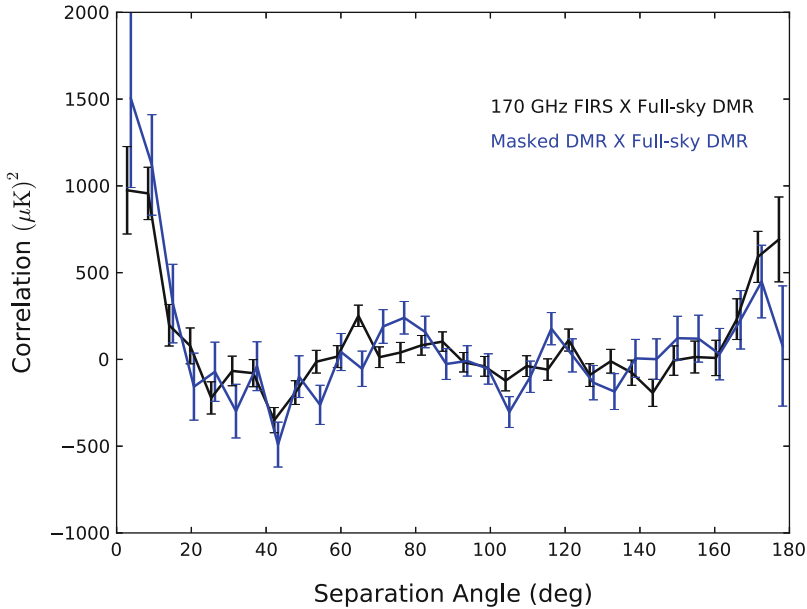
◘ Fig. 13-12

The COBE-DMR 4-year, 53 GHz sky map. The *top panel* shows the map with the dipole anisotropy included. This contribution is understood to arise from the proper motion of the Solar System barycenter with respect to the rest frame of the CMB, with a velocity of 369.3 km/s. The *bottom panel* shows the map with the best-fit dipole anisotropy subtracted off. The *red band* is microwave emission from the Milky Way, but the structure above and below the Galactic plane is CMB anisotropy that originates at the epoch of last scattering (The figure is adapted from Bennett et al. (1996))

COBE satellite (Smoot et al. 1992). The sky map from DMR's most sensitive 53 GHz band is shown in ❯ *Fig. 13-12*. By that time, the measured anisotropy level was somewhat higher than expected from theory. The interpretation paper, from Wright et al. (1992), reports "The observed anisotropy is consistent with all previously measured upper limits and with a number of dynamical models of structure formation. For example, the data agree with an unbiased cold dark matter (CDM) model with $H_0 = 50$ km/s Mpc and $\delta M/M = 1$ in a 16 Mpc radius sphere. Other models, such as CDM plus massive neutrinos [hot dark matter (HDM)], or CDM with a nonzero cosmological constant are also consistent with the COBE detection and can provide the extra power seen on 5–10,000 km/s scales."

By the time of the COBE-DMR discovery, receiver technology had advanced to the point where the anisotropy could, in principle, be detected in one night of observation. Using data taken from before the COBE launch, the FIRS team soon confirmed the COBE discovery as shown in ❯ *Fig. 13-13*.
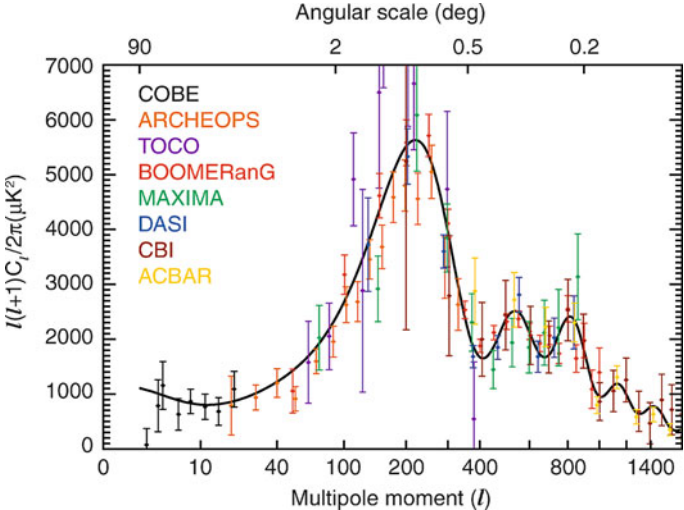
◼ Fig. 13-13
The cross-correlation between the 170 GHz FIRS survey map and the COBE-DMR "Fit Technique" reduced galaxy map (*black*), compared to the autocorrelation of the DMR map (*blue*). FIRS covered roughly a quarter of the sky in a one-night balloon flight. Both estimates use the same portion of the sky to facilitate the comparison and excise data with $|b| < 15°$. The similarity is striking: the fluctuations in DMR were also present in FIRS. The uncertainties are correlated between angular bins, so assessing statistical significance is subtle, but the confirmation by FIRS is highly significant (The figure is adapted from Ganga et al. (1993))

4.2   From COBE to WMAP

The COBE-DMR experiment had relatively coarse angular resolution: $7°$ FWHM. The casual horizon size at decoupling, when the CMB photons were last scattered, is only $1.2°$[1], so DMR was insensitive to causal physical processes occurring on these subhorizon scales. In particular, there were predictions that acoustic waves in the primordial plasma could have a coherence that would impart distinctive structure in the CMB anisotropy on subdegree (subhorizon) scales. Thus the COBE detection opened eyes to the potential for what the anisotropy on smaller angular scales could tell us. There were many questions: How large was the foreground emission on these scales? Did reionization erase the anisotropy at intermediate angular scales? Were acoustic features present, or did the power spectrum have less ringing? Did cosmic strings play a role in structure formation? Were the fluctuations produced by an isocurvature process, rather than an adiabatic one?

---

[1]We follow the conventions in Komatsu et al. (2011) because they are clearly defined but note that the often used scaling of $\Delta\theta \sim 180°/\ell$ gives different results.

If the primordial fluctuations were adiabatic, meaning that the constituent species of matter and radiation were perturbed in phase by the source mechanism, then the small-scale CMB anisotropy should exhibit a series of "acoustic peaks." Measuring the spacing and amplitude of the peaks would allow one to infer a number of fundamental cosmological parameters: the geometry and age of the universe, the abundance of baryonic and dark matter, and the slope of the primordial power spectrum of dark matter fluctuations. The fact that COBE-DMR was able to measure CMB anisotropy above the level of the galactic foregrounds on large angular scales gave the community hope that extracting the full potential of the CMB was within reach.

It is not possible to do justice to all the experimental work that took place in the decade between COBE and WMAP. There were roughly 25 independent efforts using a host of technologies and methods, all discussed in Peebles et al. (2009). The excitement of the science drove advances in detector and receiver technology. Over the decade, there were no major missteps, just a steady progression of more and more precise measurements. Immediately after COBE, there was a flurry of detections: the first measurement of the degree-scale power spectrum came from Saskatoon (Netterfield et al. 1997), while the existence and position of the first acoustic peak was identified by Miller et al. (1999), Knox and Page (2000), and Mauskopf et al. (2000). A tremendous advance by the Boomerang (de Bernardis et al. 2000) and Maxima (Hanany et al. 2000) teams revealed the CMB landscape with high precision. The next few acoustic peaks then revealed themselves over the next few years (Netterfield et al. 2002; Halverson et al. 2002; Ruhl et al. 2003) as did the Silk damping tail (Readhead et al. 2004; Kuo et al. 2004). The status of CMB anisotropy measurements just prior to WMAP is shown in ❯ *Fig. 13-14*.
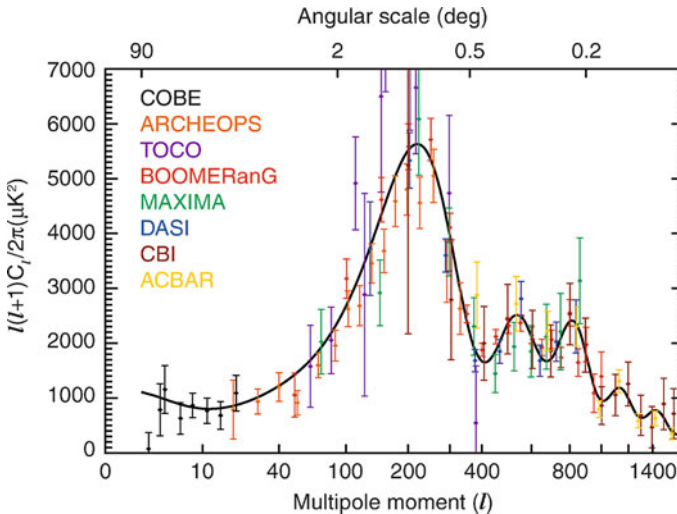
❑ **Fig. 13-14**

Compilation of CMB power spectrum measurements immediately preceding the first WMAP results. The *black curve* shows the best-fit ΛCDM model from the first-year WMAP data for comparison. On average, the pre-WMAP data agree well with the WMAP power spectrum. The references for the previous data are as follows: COBE (Tegmark 1996); ARCHEOPS (Benoît et al. 2003); TOCO (Miller et al. 2002); BOOMERANG (Ruhl et al. 2003); MAXIMA (Lee et al. 2001); DASI (Halverson et al. 2002); CBI (Pearson et al. 2003); ACBAR (Kuo et al. 2004) (Figure from Hinshaw et al. (2003))

13   Cosmic Microwave Background

5   WMAP

In 1995, following the COBE-DMR discovery of CMB anisotropy, and contemporaneous with the experimental efforts noted above, the Microwave Anisotropy Probe (MAP) mission was proposed to measure CMB fluctuations with greater precision and accuracy than was possible with the DMR. Specifically, MAP was tailored to have an angular resolution of better than $1/3°$ in order to resolve the CMB's acoustic oscillation features expected to be present at subhorizon distance scales (about $2°$ across the sky at the distance of the last scattering surface). If present, the features would allow one to deduce detailed information about the shape, content, and age of the universe, among other things.

As MAP was being developed, the guiding principle was control of systematic errors (Bennett et al. 2003b). Among the design features incorporated into the mission were:

- A symmetric differential design
- Rapid large-sky-area scans
- Four switching/modulation periods
- A highly interconnected and redundant set of differential observations
- An L_2 orbit to minimize contamination from Sun, Earth, and Moon emission and allow for thermal stability
- Multiple independent channels
- Five frequency bands to enable a separation of galactic and cosmic signals
- Passive thermal control with a constant Sun angle for thermal and power stability
- Control of beam sidelobe levels to keep the Sun, Earth, and Moon levels <1 μK
- A main beam pattern measured accurately in-flight (using Jupiter)
- Calibration determined in-flight to the subpercent level (from the CMB dipole and its modulation from MAP's motion)
- Low cross-polarization levels (below −20 dB)
- Precision temperature sensing at selected instrument locations

Because of these multiple cross-checks, the MAP data could be understood in great detail. As discussed, the precision, accuracy, and reliability made possible by this has set the foundation for the standard model of cosmology.

   ❯ *Figure 13-15* shows a side view of the MAP's differential observatory, indicating two lines of sight to the sky which are sensed by the differential receivers located in the focal plane assembly (FPA), directly underneath the telescope. The FPA itself, shown in the lower right, prior to its integration on the spacecraft, houses 10 "differencing assemblies" spanning frequencies from 23 to 94 GHz.

   MAP was launched at 15:47 EDT on 30 June 2001 from Cape Canaveral, FL aboard a Delta 7425–10 rocket. The satellite executed a sequence of phasing loops to position itself for a lunar swingby en route to the second Sun-Earth Lagrange point, L_2. MAP commenced cosmological observations from L_2 on 10 August 2001. The first results from MAP – based on one year of data – were released in February 2003. A few months prior to the first release, one of the leading figures in CMB research, and a founding member of the MAP team, Dave Wilkinson of Princeton University, passed away. The satellite was renamed the Wilkinson Microwave Anisotropy Probe (WMAP) in his honor. Subsequent data releases, based on 3, 5, and 7 years of data at L_2 were released in 2006, 2008, and 2010, respectively; and each release subsumes the earlier data and incorporates improved data processing algorithms. In this chapter we only discuss the most recent results based on 7 years of data.
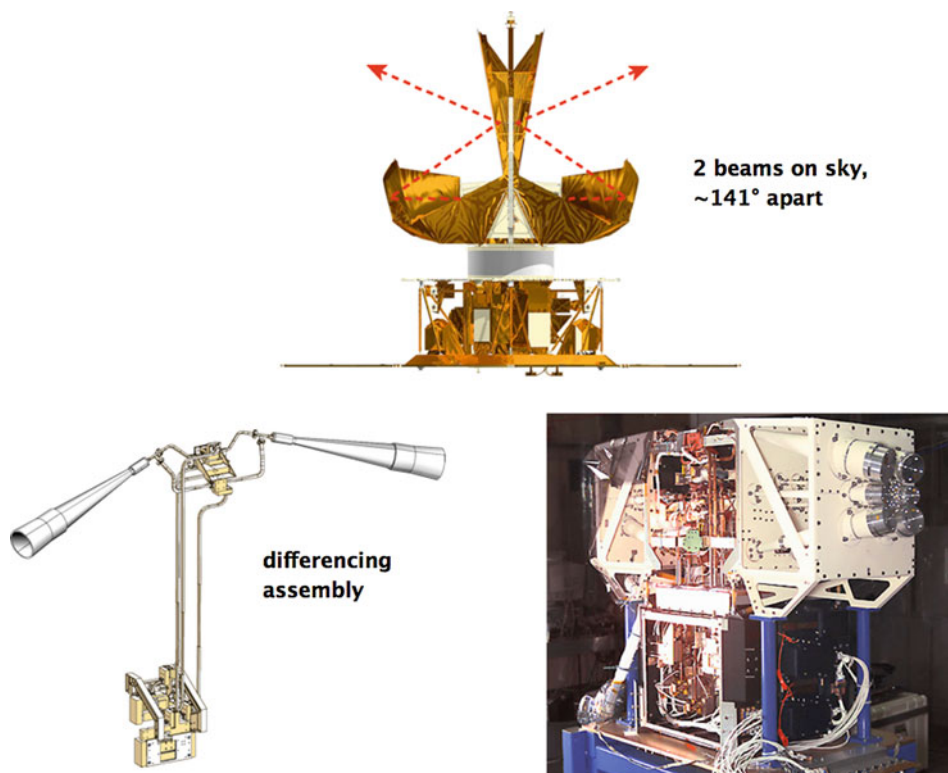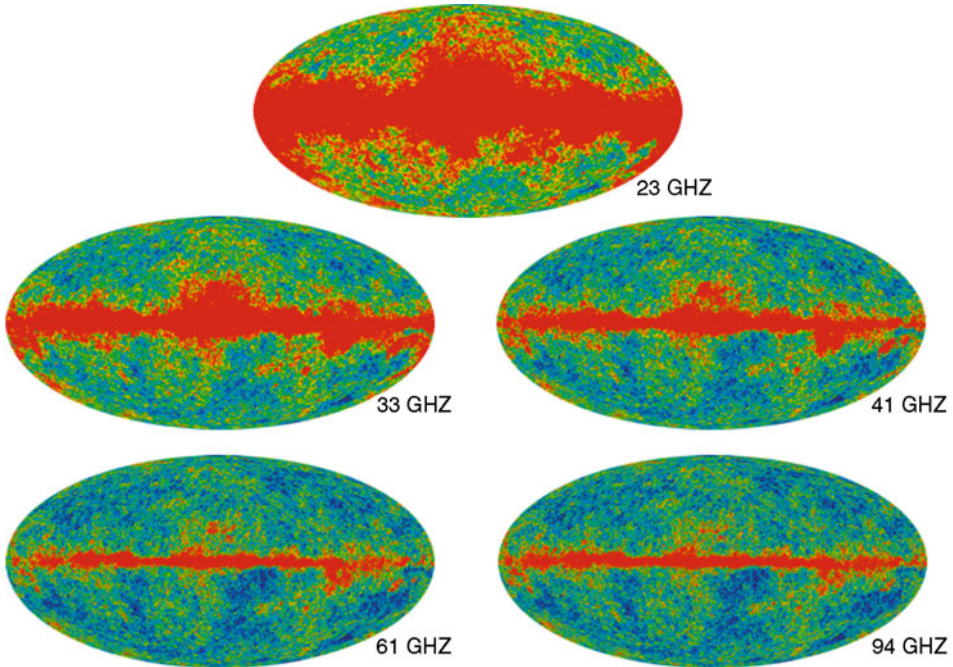
◼ Fig. 13-15
The WMAP instrument consists of back-to-back Gregorian optics (*top*) that feed sky signals from two directions into ten 4-channel polarization-sensitive receivers called differencing assemblies (*bottom-right*). The HEMT amplifier-based receivers cover five frequency bands from 23 to 94 GHz. Each pair of channels is a rapidly switched differential radiometer (*bottom-left*) designed to cancel common-mode systematic errors. The signals are square-law detected, voltage-to-frequency digitized, and then downlinked

5.1 WMAP Sky Maps

The five frequency band maps produced from 7 years of WMAP observations at L2 are shown in ❯*Fig. 13-16* (temperature anisotropy) and ❯*Fig. 13-17* (polarization anisotropy). These full-sky maps are the primary product of the WMAP mission since they represent the most compressed form of the mission data one can produce without essential loss of information. The temperature maps show significant emission in the galactic plane due to synchrotron, free-free, and dust emission, but the CMB emission – seen clearly in the maps at high galactic latitude – is constant in thermodynamic temperature units. The polarization maps also show clear Galactic emission, primarily from synchrotron radiation, but the polarized CMB emission is only detected statistically – no specific feature seen in the polarization maps can be ascribed to the CMB.
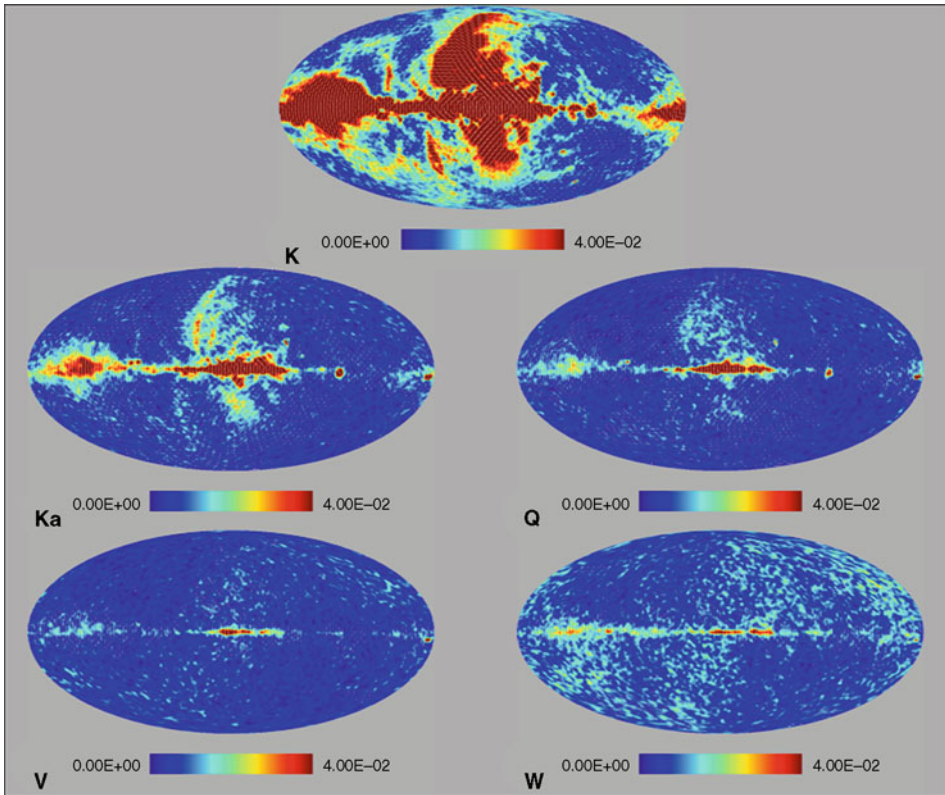
◨ **Fig. 13-16**

The WMAP 7-year frequency band maps in galactic coordinates from 23 to 94 GHz. Note the strong frequency dependence of the galactic microwave emission and the constancy of the CMB fluctuations at high galactic latitude

The frequency spectrum of the Galactic emission is very different from the CMB. ❷ *Figure 13-18* shows the frequency spectra of the known galactic emission components, in antenna temperature units, compared to CMB anisotropy in the same units. The vertical range of each emission band indicates the *rms* signal level as a function of frequency if 77% (lower) or 85% (upper) of the sky is retained. The five WMAP frequency bands, which are each ~20% wide, span the minimum of the galactic foreground window. There are a variety of techniques that can be employed to separate the CMB component from the Galactic emission, each with their own advantages and disadvantages. Conceptually, the simplest approach is to form a linear combination of the frequency bands in such a way as to cancel signals with a Galactic spectrum while preserving signal with a CMB spectrum. This approach has been taken by the WMAP team to produce the "Internal Linear Combination" (ILC) CMB map shown in ❷ *Fig. 13-19* (Bennett et al. 2003a; Gold et al. 2011).

The CMB map depicted in ❷ *Fig. 13-19* looks like random noise, and in a very specific sense, that is exactly what it is. There is no theory of cosmology that predicts any specific feature in the CMB, only the statistical properties of the fluctuations in the map. As a result, we must analyze the map using statistics that can be compared to theoretical models. Perhaps the most remarkable feature of the CMB map is that there is a preferred angular scale in the data. One way to see this is via a stacking analysis: take every isolated hot spot (local maximum) in the map and excise a postage stamp image of the data in its vicinity. Now coadd the postage stamp images
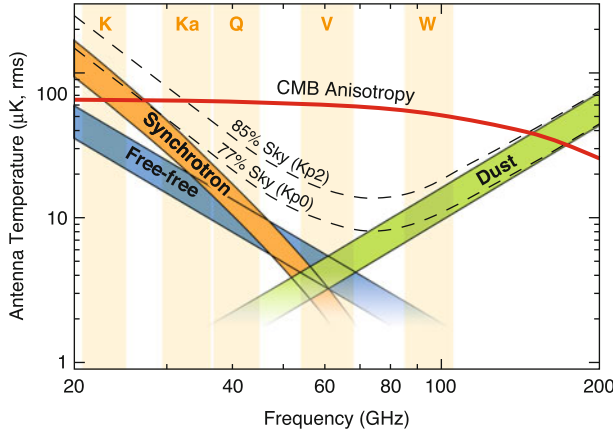
⊡ Fig. 13-17

The WMAP 7-year frequency band polarization maps from 23 to 94 GHz. The maps are dominated by galactic synchrotron and dust emission

with each one centered on the location of its respective temperature peak. Repeat the procedure for the locus of cold spots. The results of this stacking are shown in ❯ *Fig. 13-20*. The remarkable feature in the temperature data (left panels) are the concentric rings 1.2° from the central hot and cold spots. These features are the remnants of acoustic waves that propagated in the primordial plasma for 400,000 years until the electrons and protons "recombined" in the cooling plasma to form neutral gas which could no longer support acoustic waves. From this time on, CMB photons have propagated across the universe largely unimpeded, carrying with them the image of the last scattering or decoupling epoch, and all the information that it encodes.

5.2 WMAP Angular Power Spectrum

As noted above, cosmological models do not predict specific features in the CMB anisotropy, only their statistical properties. The simplest models predict that the CMB fluctuations are Gaussian distributed with random phase. We define the precise meaning of this shortly, but

◘ Fig. 13-18
The frequency spectra of CMB and galactic foreground emission in units of antenna temperature. WMAP observed in five bands because the foreground emission from our own Galaxy has a different frequency spectrum than the CMB (which is constant in the units used by WMAP), and the multifrequency data enables a separation of the two components
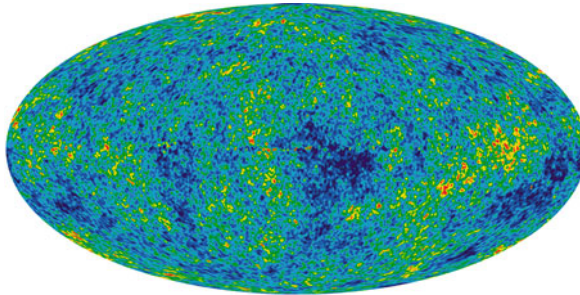

◘ Fig. 13-19
The WMAP 7-year CMB map formed from an internal linear combination ("ILC") of the five frequency band maps, in such a way as to null emission with galactic frequency spectra

we note first that a Gaussian, random-phase field can be completely characterized by its 2-point correlation function, or equivalently, its angular power spectrum. Higher-order moments can be uniquely related to the 2-point (variance) statistics.

True for many analyses, it is convenient to expand the temperature anisotropy map, $T(\mathbf{n})$, in the basis of spherical harmonic functions, $Y_{\ell m}(\mathbf{n})$,

$$T(\mathbf{n}) = \sum_{\ell,m} a_{\ell m} Y_{\ell m}(\mathbf{n}). \tag{13.2}$$

(The inclusion of the monopole and dipole terms ($\ell = 0,1$) in this expansion are a matter of convention. Processes associated with these terms are distinct from those of the higher-order anisotropy. These contributions are discussed earlier in this article.) The leading explanation for the origin of the $\ell > 1$ anisotropy is that it arises from perturbations generated during inflation.
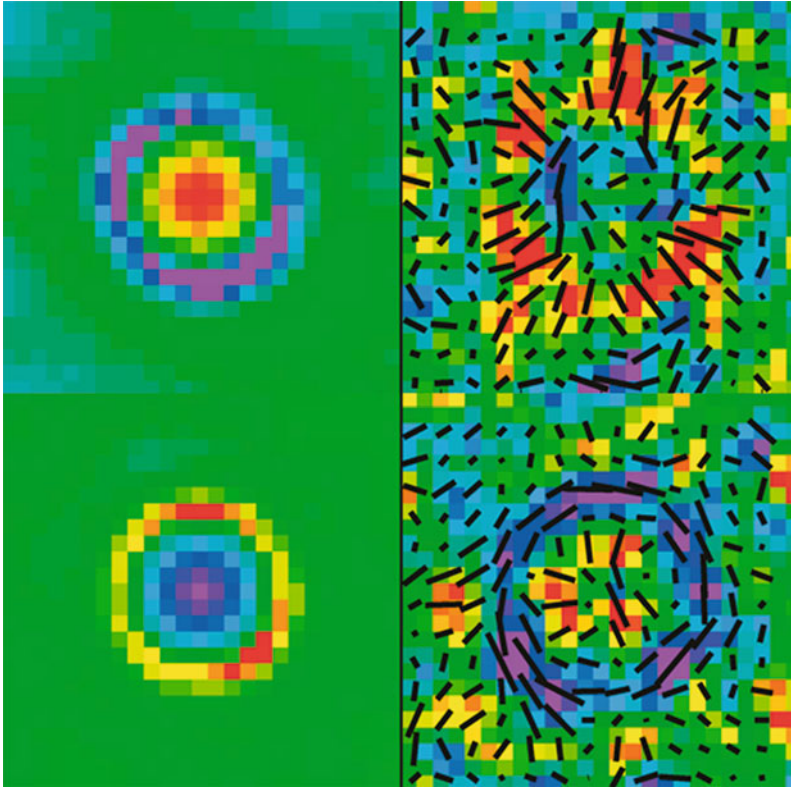
◘ Fig. 13-20

The WMAP 7-year temperature and polarization maps stacked by location of hot spots (*top panels*) and cold spots (*bottom panels*). The temperature data are on the *left*, the polarization on the *right*. Each of the four panels represents a 5° × 5° square of sky. As discussed in the text, these images display the remnants of acoustic oscillations in the primordial plasma

We cannot predict the map $T(\mathbf{n})$ (or, equivalently, the $a_{\ell m}$ coefficients) but rather only the statistical properties of the $a_{\ell m}$. If the fluctuations are indeed Gaussian, distributed with random phases, then the $a_{\ell m}$ distribution is completely specified by its angular power spectrum,

$$C_\ell \equiv \langle |a_{\ell m}|^2 \rangle, \qquad (13.3)$$

where the angle brackets indicate ensemble average, in this case over an ensemble of widely separated cosmic observers, each of whom samples a statistically independent realization of the cosmic fluctuation field. The primary goal of anisotropy measurements is to estimate the underlying power spectrum as accurately as possible from the data since this is the observable that allows one to constrain cosmological parameters.

In practice, since we have only one sample of the cosmic fluctuation field on our own surface of last scattering, our ability to infer the parent spectrum, C_l, is limited by "cosmic variance." Conceptually, if we have a full-sky anisotropy map, we can invert (❯ 13.2) to obtain

the measured $a_{\ell m}$ and use them to estimate the power spectrum observed in our sky,

$$C_\ell^{\text{sky}} = \frac{1}{2\ell + 1} \sum_m |a_{\ell m}|^2. \tag{13.4}$$

Since each multipole, ℓ, has only $2\ell + 1$ independent m modes, the cosmic variance uncertainty inherent in the estimator C_ℓ^{sky} is

$$\Delta C_\ell = C_\ell \sqrt{\frac{2}{2\ell + 1}}. \tag{13.5}$$

For the quadrupole (ℓ = 2) power, this implies an irreducible uncertainty of 63%; at high ℓ, the fractional uncertainty falls as $\ell^{-1/2}$, becoming subdominant to instrument noise at suitably high ℓ. As of this writing, the measured spectrum uncertainty is limited by cosmic variance up to $\ell = 550$. The C_ℓ measurement by the Planck satellite is expected to be cosmic variance limited to $\ell \approx 1,500$.

Readers more comfortable with position space than Fourier space may prefer to characterize the fluctuation properties by the angular correlation function, $C(\theta)$. This is related to the angular power spectrum by a Legendre transform

$$C(\theta) = \frac{1}{4\pi} \sum_\ell (2\ell + 1) \, C_\ell \, P_\ell(\cos \theta), \tag{13.6}$$

which can be estimated directly from a sky map by averaging the product of all temperature measurements separated by an angle θ,

$$C^{\text{sky}}(\theta) = \langle T(\mathbf{n}) T(\mathbf{n}') \rangle, \tag{13.7}$$

where the average is taken over all direction pairs, $\mathbf{n}, \mathbf{n}'$ such that $\mathbf{n} \cdot \mathbf{n}' = \cos \theta$ (to within some finite bin size in θ).

In practice, real world effects such as instrument noise, systematic errors, and contamination from Galactic emission force us to adopt significantly more difficult methods for estimating the power spectrum and its uncertainty. However, due to clever work by a great number of researchers in the field, these hurdles have been largely overcome, and they do not qualitatively alter the simple description given above.

The angular power spectrum inferred from the 7-year WMAP data is shown in ❯ *Fig. 13-21*. The red curve is the best-fit ΛCDM model fit to the data (see ❯ Sect. 6). The error bars plotted with the data show the uncertainty due to WMAP's instrument noise, while the gray band centered on the ΛCDM curve indicates the cosmic variance associated with that model. We expect the power spectrum observed in our sky to fluctuate from the underlying smooth curve by an amount characterized by the gray band, even in the absence of instrument noise, and our inference of the best-fit model must account for this cosmic variance.

5.3 Beyond WMAP

Aside from WMAP, the flurry of experimental activity that preceded it has continued to the present day. ESA's Planck satellite is remapping the CMB sky with exquisite sensitivity and angular resolution more than twice that of WMAP's. Planck was launched on May 14, 2009, from Kourou, French Guiana. The cryogenic HFI instrument observed for over 2.5 years before its cryogens depleted in January 2012, while the H_2 sorption pump cooled LFI instrument
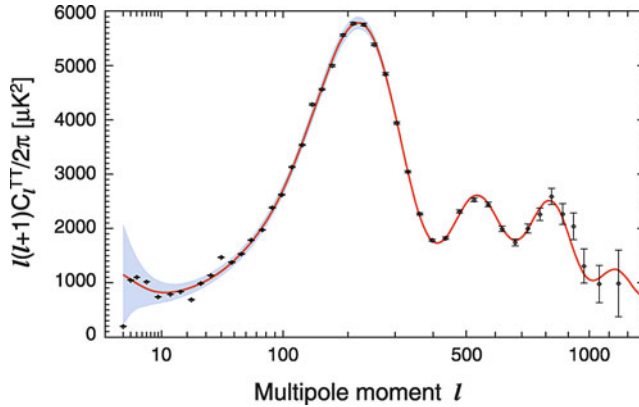
■ Fig. 13-21

**The 7-year WMAP power spectrum. The** *black points* **with error bars show the data, the** *red line* **shows the best fit model, and the** *gray swath* **shows the cosmic variance, as discussed in the text. Although at first glance it may appear that some points are discrepant with the model, this is not supported by a statistical analysis. In particular, recall that roughly 1/3 of the data points should lie outside the cosmic variance swath**

continues to observe as of this writing. The first cosmological results from Planck are expected in early 2013, and the community eagerly awaits them.

In the meantime, two flagship ground-based telescopes have each been deployed for a few years now: the South Pole Telescope is a 10-m observatory situated at the South Pole station, while the Atacama Cosmology Telescope (ACT) is a 6-m observatory deployed at an elevation of >5,000 m in the Atacama Desert in Chile. Both of these systems are equipped with state-of-the-art bolometric receiver systems that render them capable of measuring temperature anisotropy up to multipole moments of $l \sim 10,000$. Both SPT and ACT extend the reach of CMB observations well beyond that obtainable by WMAP (and even Planck, though the latter will have superior power spectrum sensitivity up to $l \sim 2,000$ due to its full sky coverage). A compilation of the WMAP, SPT, and ACT power spectrum measurements is shown in ❯ *Fig. 13-22*. The cosmological implications of these measurements are discussed next.

6   The Standard Cosmological Model

In this section, we interpret the CMB data and other observations in terms of a handful of cosmological parameters. We take as a starting point that the dynamics of the universe are governed by General Relativity and that the Cosmological Principle applies, namely that on suitably large scales, the universe is homogeneous and isotropic. In the context of General Relativity (a metric theory of gravity), the Cosmological Principle requires that the metric of space-time be of the Robertson-Walker form. This metric can have positive, negative, or zero spatial curvature, and the relative size of the universe can be described by a dimensionless scale factor, $a(t)$, whose dynamics are governed by the Friedmann equations: the Einstein equations applied to the Friedmann-Robertson-Walker metric. The specific behavior of $a(t)$ depends on the initial
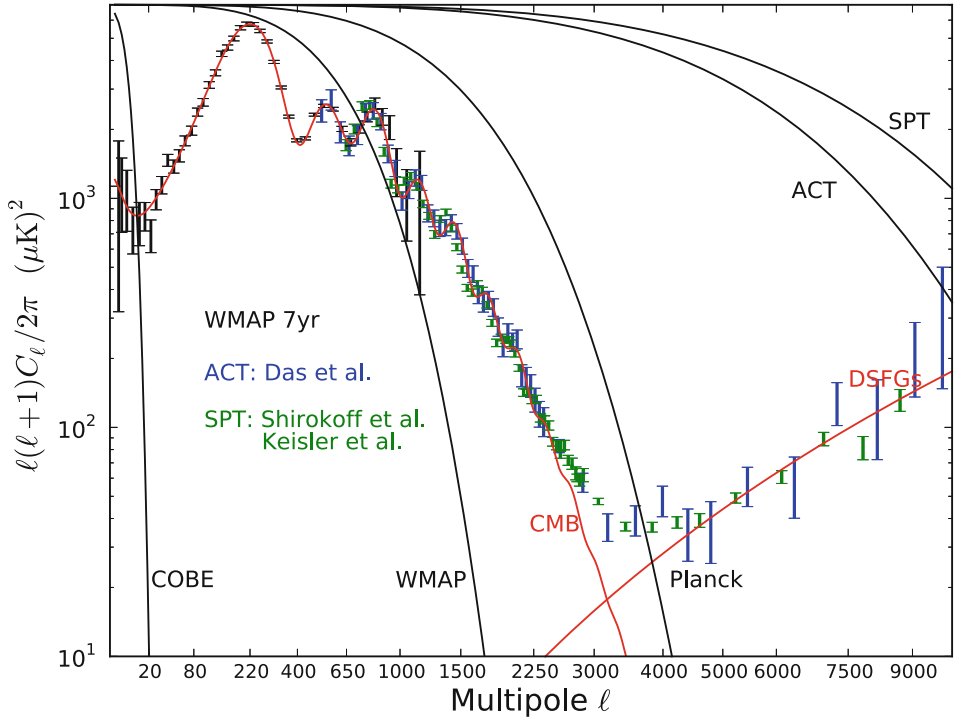
■ **Fig. 13-22**

A compilation of the most sensitive CMB power spectrum measurements published c. 2012 (Larson et al. 2011; Shirokoff et al. 2011; Das et al. 2011a; Keisler et al. 2011). The best-fit ΛCDM cosmological model (*solid red*) dominates the signal up to *l* ∼ 3,000. The model power spectrum for $\ell > 3{,}000$ is due to Poisson noise from confusion-limited dusty star-forming galaxies (DSFGs) observed at 150 GHz. The *black lines* indicate the angular resolution of various instruments, as measured by their window functions (the degree to which beam smoothing suppresses variance as a function of angular scale). The *l*-axis is scaled as $l^{0.45}$ to emphasize the middle range of the anisotropy spectrum. The increasing size of the WMAP uncertainties near *l* = 2 and 1,000 are due to cosmic variance and finite beam resolution, respectively. The cosmological implications of these data are discussed in ❯ Sect. 6

conditions and on the matter and radiation content of the universe, but to our knowledge, it has been monotonically increasing throughout time.

As discussed earlier, the blackbody spectrum of the CMB provides compelling evidence for a hot early universe that was in thermal equilibrium and which has expanded and cooled adiabatically. As we discuss later, the detailed expansion history is a topic of intense current research. The isotropy of the CMB brightness suggests an isotropic universe, consistent with the Cosmological Principle. While isotropy does not require homogeneity, isotropy without homogeneity would require that we occupy a special place in the universe, which seems untenable. Further, the observation that galaxies recede from us, on average, at a speed proportional to their distance, implies a homogeneous expansion; indeed, homogeneous expansion requires this proportionality. And, while some argue that there is no definitive evidence for a cutoff in the

scale at which galaxies cluster, most workers in the field accept that at scales beyond ~1,000 Mpc, the clustering of matter becomes insignificant. Thus, throughout most of this chapter, we adopt the homogeneous and isotropic Hot Big Bang Model as our paradigm.

6.1 The Origin of Structure

The notion that the universe is homogeneous is a useful approximation, but it obviously breaks down at some point because there is clearly structure in our universe. On scales smaller than ~100 Mpc, the contrast between overdense and underdense regions exceeds unity; and on scales comparable to our Solar System, it far exceeds unity! In contrast, anisotropy in the CMB limits structure in the radiation field to be of order one part in 10^5, which implies corresponding limits on baryonic matter fluctuations on large scales, at early times. The basic paradigm for structure formation is that some process seeded fluctuations in the very early universe – cosmic inflation is the leading mechanism – and that these fluctuations grew in time by gravitational accretion to form the structure we see today. In fact, much of what we know about our universe comes from observing the evolution of cosmic structure over a range of scales. CMB anisotropy provides the cleanest probe of structure because it is weak, and therefore a product of simple linear physics, but later observations of structure as traced by galaxies are also crucial to constrain cosmological models.

It is beyond the scope of this chapter to cover perturbation theory in General Relativity, or the technology of N-body simulations that are required to study nonlinear structure. Rather, we will focus on what the current observations of structure tell us about cosmological models.

For the purpose of interpreting CMB anisotropy, the most important concept to understand is that of "baryon acoustic oscillations" (BAO). We imagine that some process like cosmic inflation imparted a spectrum of density perturbations to the universe at very early times – effectively $t = 0$ – and we wish to track how those perturbations evolve between then and the time when the CMB was decoupled 400,000 years later. The basic physics of acoustic oscillations was worked out in the late 1960s (Peebles and Yu 1970; Sunyaev and Zel'dovich 1970a; Silk 1968) and has been refined ever since, to the point where numerical codes that solve the Boltzmann transport equations can now predict matter and radiation perturbation spectra to an accuracy of better than 1% (Howlett et al. 2012).

If the initial fluctuations were "adiabatic," meaning that the various species of matter and radiation perturbed in phase, then an initial overdensity of baryonic matter will propagate outward as a sound wave front with a speed that is determined by the bulk modulus of the relativistic plasma, $c_s \approx c/\sqrt{3}$, where c is the speed of light. When the cosmic plasma becomes neutral at the epoch of recombination, the sound waves in the photon-baryon fluid "freeze out" due to the loss of photon pressure. The distance traveled by these wave fronts is called the sound horizon (or the BAO scale) and is known very precisely from the propagation velocity and the travel time, both of which only depend on the matter to radiation ratio, which is now quite well measured.

The effect of BAO on the radiation is to impart a feature in its 2-point correlation function or angular power spectrum. Specifically, we expect a coherent series of peaks in the power spectrum, corresponding to the harmonics of the propagating sound wave fronts. The detailed spacing and amplitude of these peaks contain a wealth of information about the geometry and contents of the universe. Indeed, the mere *existence* of these peaks is a remarkable triumph for

theoretical cosmology. The fact that such structure was predicted long before it was considered observable is an excellent reminder that cosmology is a predictive science.

It is worth emphasizing this point once again. The relatively narrow width and coherence of the eight acoustic peaks seen in ❯ *Figs. 13-21* and ❯ *13-22* are an indication that the initial fluctuations were predominantly adiabatic. Specifically, the WMAP7 data limits out-of-phase "isocurvature" perturbations to be less than ~10% of the total signal. The fact that we are able to resolve these peaks at all is the key feature that makes the CMB such a powerful probe of cosmological parameters. The universe could have easily been much more complicated than it has turned out to be so far.

6.2 Geometry of the Universe

In the context of the General Relativity and the Friedmann-Robertson-Walker metric, a flat universe is an unstable fixed point. That is, any positive or negative spatial curvature present in the universe grows with time. In order for the universe to be within an order of magnitude of flat today – as measured by the total energy density, Ω_0 – it must have been extremely close to unity in the past. This fine-tuning problem, known as the flatness problem, was one of the motivating factors for cosmic inflation. Inflation addresses the flatness problem by invoking a period of accelerated expansion in the very early universe, which dilutes any existing spatial curvature to negligible levels. Generically, inflation predicts that the geometry should be should be flat to a part in 10^4.

CMB anisotropy probes geometry by measuring the angular size of the sound horizon, as probed by the position of the first acoustic peak in the power spectrum. If we know the distance to the last scattering surface, we can complete the triangle and determine the shape of light-like geodesics that span the space between us and the last scattering surface. Unfortunately, the distance to the last scattering surface is not known a priori, since it depends on the low-redshift normalization of the distance-redshift relation, that is, the Hubble constant. We illustrate this degeneracy in ❯ *Fig. 13-23*.

On the left are two hypothetical triangles with the same opening angle and sound horizon but different lengths. To first order the CMB is unable to distinguish between these two geometries. This is shown quantitatively in the right panel which shows allowable models that are consistent with the WMAP data. Each point in the panel represents a cosmological model that falls within the 95% confidence region of the WMAP7 data. The points are color-coded by the value of the Hubble constant required to produce the correct angular size of the sound horizon (as measured by the first acoustic peak position). The solid line with $\Omega_0 = \Omega_\Lambda + \Omega_m$ corresponds to a flat universe; points to the right of that line correspond to a closed universe. The WMAP7 data alone give $\Omega_0 = 1.0080^{+0.093}_{-0.071}$, but this jointly requires a low value for the Hubble constant, $H_0 = 53^{+13}_{-15}\,\mathrm{m\,s^{-1}\,Mpc^{-1}}$. If, in addition, we invoke the independent measurement of the Hubble constant by, for example, Riess et al. (2011) of $H_0 = 73.8 \pm 2.4$, the limits on curvature tighten to $\Omega_0 = 1.0023^{+0.056}_{-0.054}$, as shown by the blue contours on the right panel of ❯ *Fig. 13-23*. Remarkably, the Hubble constant measurement breaks the geometric degeneracy in the CMB right where the spatial geometry is flat (Euclidean). ❯ *Figure 13-24* illustrates the geometric degeneracy in the CMB in the context of the observable power spectrum. For the remainder of this chapter, we adopt a flat universe unless otherwise noted.
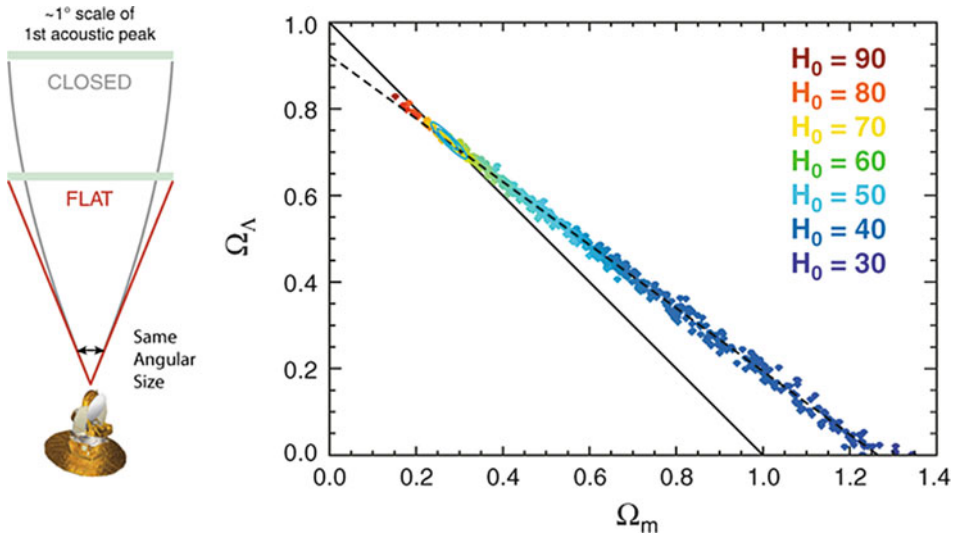
◼ Fig. 13-23
The geometric degeneracy inherent in CMB anisotropy is shown as the *dashed line* – see text for details. The small blue contours in the *right panel* indicate that the combination of WMAP7 data and a recent measurement of the Hubble constant strongly favor a flat universe
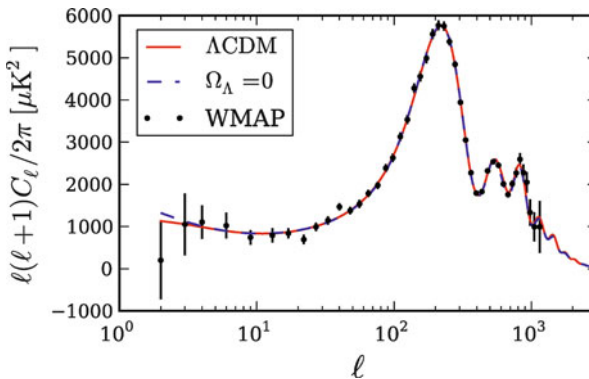
◼ Fig. 13-24
The geometric degeneracy in the CMB angular power spectrum. The *red curve* is the standard ΛCDM model with $\Omega_\Lambda = 0.73$ and $\Omega_m \approx 0.26$. The *blue curve* corresponds to $\Omega_\Lambda = 0$ and $\Omega_m \approx 1.3$. The models are not significantly distinguishable with WMAP data *alone* (The figure is from Sherwin et al. (**2011**))

6.3   The Matter Content of the Universe

Given the interpretation of a flat universe, we turn to the matter and energy content required to produce $\Omega_0 = 1.0023^{+0.056}_{-0.054}$. The acoustic peak spectrum is sensitive to both the total matter density, Ω_m, and separately to the baryonic matter density, Ω_b. The sensitivity to both arises because

the total matter density acts as a driving term to the acoustic oscillations, while the baryons – which participate in the oscillations – act as a small drag term. The odd and even harmonics in the acoustic spectrum correspond to modes that froze out at maximum compression and maximum rarefaction, respectively. Because of baryon drag, there is a small asymmetry between the compression and rarefaction in the BAO, which gives rise to a feature in the CMB power spectrum, namely that the even peaks will be suppressed relative to the odd ones as the fractional contribution of baryons to the total matter density, Ω_b/Ω_m, is increased.

If one restricts the cosmological model parameter space to the six parameters of the flat ΛCDM model: the physical baryon density, $\Omega_b h^2$; the physical cold dark matter density, $\Omega_c h^2$; the cosmological constant in units of the critical density, Ω_Λ; the slope of the primordial power spectrum, n_s; the optical depth of the reionized medium, τ; and the overall amplitude of the fluctuations, A, the 7-year WMAP data alone gives the following constraints on the matter densities: $100\Omega_b h^2 = 2.258 \pm 0.057$ and $\Omega_c h^2 = 0.1109 \pm 0.0056$, corresponding to $\Omega_b = 0.0449 \pm 0.0028$ and $\Omega_c = 0.222 \pm 0.026$ (Larson et al. 2011). If one combines WMAP with SPT data, the constraints tighten by 15–25% to $100\Omega_b h^2 = 2.22 \pm 0.042$ and $\Omega_c h^2 = 0.112 \pm 0.0048$ (Keisler et al. 2011).

Reducing the uncertainty on Ω_m is of interest for future tests of physics beyond the standard ΛCDM model since the matter abundance is coupled to CMB probes of neutrino physics and to the details of how dark energy affects the expansion history of the universe. The current uncertainty in Ω_m is dominated by uncertainty in the amplitude of the third acoustic peak, which is still limited by noise in the WMAP data, and by calibration uncertainty in the SPT and ACT data. The Planck satellite should produce a cosmic variance limited measurement of the third acoustic peak which will substantially improve the uncertainty in our knowledge of this key parameter.

6.4 The Age of the Universe

Given the assumption of a flat universe and the above determination of the matter and energy content (which explicitly assumes that $\Omega_\Lambda = 1 - \Omega_m$, ignoring the negligible present-day radiation density), we can derive the age of the universe by solving the Friedmann equations for the expansion history. The age is interpreted to be the elapsed time since $a(t) = 0$ (i.e., the "Big Bang"). This procedure also predicts the present-day expansion rate, $\dot{a}$ from which we can derive the Hubble constant, $H_0 \equiv (\dot{a}/a)_0$, where the subscript 0 means evaluated at the present time.

For the 7-year WMAP data, the age of the universe is determined to better than 1% precision: $t_0 = 13.75 \pm 0.11$ Gyr, with a predicted Hubble constant of $H_0 = 70.4^{+1.3}_{-1.4}$ km s^{-1} Mpc^{-1}. The latter is in good agreement with the independently determined (Riess et al. 2011) value noted above, $H_0 = 73.8 \pm 2.4$ km s^{-1} Mpc^{-1}. If we relax the assumption of flatness, but invoke the independent Hubble constant measurement to constrain the Friedmann solution, we derive a consistent age with an uncertainty of just under 2%, $t_0 = 13.86 \pm 0.26$ Gyr (Komatsu et al. 2011).

Note that these results assume that dark energy has the form of a cosmological constant. If the dark energy equation of state has a more "exotic" form that makes dark energy more significant in the early universe (as a fraction of the total energy density), the expansion history, and hence the age of the universe, could be somewhat different than the ΛCDM model predicts. There is currently no evidence to support such a model, but it cannot presently be ruled out.

6.5 Initial Conditions: The Inflationary Parameters

The inflation mechanism (Guth 1981; Linde 1982; Albrecht and Steinhardt 1982; Sato 1981) was proposed to resolve a number of problems with the "classical" Big-Bang Model. The main problems were the following: (1) "The monopole problem." In Grand Unified theories, there should be a sea of magnetic monopoles in the universe. None have been observed. (2) "The flatness problem." A slight deviation from flatness in the early universe is amplified by the cosmic expansion. The universe is so close to being flat today (❯ Sect. 6.2) that there seems to have been some kind of fine tuning at work to make the early universe extremely flat. (3) "The horizon problem." Two regions on the sky separated by more than $\theta_h = 1.2°$ at the time of decoupling are causally disconnected given the standard expansion history. Yet the CMB is isotropic to a part in 10^5, implying that our entire observable universe evolved from a region that was once in thermal equilibrium, and thus in causal contact. Inflation resolves these problems by postulating a period of accelerated (likely exponential) expansion in the very early universe, possibly associated with a symmetry-breaking phase transition when the temperature of the universe was at the scale of grand unification, $T \sim 10^{16}$ GeV, $t \sim 10^{-35}$ s.

Inflation solves the above three problems as follows: if inflation takes place after the production of magnetic monopoles, their abundance will be diluted to negligible levels. Similarly, curvature decreases during accelerated expansion; if the overall growth factor experience during inflation is sufficient, the curvature will be reduced to negligible levels. Finally, during a period of accelerated expansion, the horizon becomes much larger than was previously inferred from "classical" decelerating expansion. In order for inflation to quantitatively solve these three problems, the universe must have inflated by a factor of at least 50–60 e-folds in the scale factor. This implies that the current energy density of the universe should be within about one part in 10^4 of the critical density, $\rho_c = 3H^2/8\pi G$. It will likely be a while before this level of measurement precision is reached.

A remarkable prediction of inflation is that all structure in the universe today was ultimately a product of quantum mechanical fluctuations in the microscopic preinflationary universe. During inflation, these fluctuations became "classical" density fluctuations on astrophysical length scales, and they subsequently evolved into the web of cosmic structure we observe today. The simplest physical models of inflation are driven by a single scalar "inflaton" field, and these models predict that the density fluctuations should be Gaussian distributed with random phases. In particular, if we have a density fluctuation field $\delta(\mathbf{x})$, and we Fourier transform it,

$$\delta(\mathbf{x}) \equiv \frac{\rho(\mathbf{x})}{\bar{\rho}} - 1 = \int d^3k\, \delta(\mathbf{k})\, e^{i\mathbf{k}\cdot\mathbf{x}}, \tag{13.8}$$

then the Fourier modes are Gaussian distributed with variance,

$$\langle \delta(\mathbf{k})\delta(\mathbf{k}') \rangle = \frac{2\pi^2}{k^3}\delta^3(\mathbf{k} - \mathbf{k}')P(k), \tag{13.9}$$

where $P(k)$ is the primordial power spectrum of density fluctuations. Single-field inflation models predict that the primordial spectrum should be well approximated by a power law over the range of scales we can observe with cosmic structure, $P(k) \propto k^{n_s-1}$, where n_s is the spectral index of the fluctuation spectrum. Note that $P(k)$ gives the variance of fluctuations as a function of wave vector, k, which is roughly equivalent to angular scale on the fixed surface of last scattering.

Inflation further predicts the slope or "tilt" of the primordial power spectrum, as measured by n_s (Mukhanov and Chibisov 1981; Hawking 1982; Guth and Pi 1982; Starobinsky 1982; Bardeen et al. 1983).[2] As inflation proceeds, the inflaton potential energy and $P(k)$ decrease with time. Since the largest length scales inflate past the horizon first and "freeze out," the primordial spectrum is generically expected to have a "red" tilt, meaning that large scales should have a slightly higher primordial variance than small scales, that is, $n_s < 1$.

CMB data now indicate that the $P(k)$ is indeed lower at smaller scales. The 7-year WMAP data gives $n_s = 0.963 \pm 0.014$. The smaller scale SPT and ACT data expand the lever arm of physical scales over which to fit the primordial slope and give even more precise constraints. For example, the combination of WMAP and SPT gives $n_s = 0.9663 \pm 0.0112$. This is an amazing observation. Before inflation, Harrison, Peebles, and Zel'dovich posited $n_s = 1$ on the grounds of naturalness. Today, all indications are that n_s is less than unity at the 3σ level, which points to the need for a detailed physical model for the origin of fluctuations. Inflation provides one such class of models, which can now be put to the test with data. The idea that we can think of testing physics at the energy scales implied by inflation is nothing short of incredible.

Limits on deviations from a power law, as measured by the running index parameter, $\alpha = dn_s/d\ln k$ (Kosowsky and Turner 1995), show that α is within 2σ of zero.

Many models of inflation predict that there should be a background of primordial gravitational waves: propagating perturbations in space-time. In contrast to density fluctuations, which are associated with scalar perturbations in the space-time metric, gravity waves are associated with tensor perturbations. Single-field inflation models robustly predict that the amplitude of the gravity wave background is proportional to the energy scale at which inflation occurred (Baumann et al. 2009):

$$P_t(k) = \frac{2}{3\pi^2} \left. \frac{V}{M_{pl}^4} \right|_{k=aH},\qquad(13.10)$$

where $P_t(k)$ is the power spectrum of tensor perturbations (analogous to the density perturbation spectrum noted above), V is the energy scale of inflation, and H is the Hubble parameter during inflation.[3] The detection of primordial B-modes would impact far more than just cosmology. It would be the first example of an empirical connection between gravity and quantum field theory.

Observationally, the amplitude of the gravity wave background is parameterized by the "tensor to scalar" ratio,

$$r \equiv \left. \frac{P_t(k)}{P_s(k)} \right|_{k=0.002\,\mathrm{Mpc}^{-1}},\qquad(13.11)$$

which is simply the ratio of tensor to scalar power spectra, evaluated at a particular wavelength. Both types of perturbations contribute to temperature anisotropy in the CMB, via the Sachs-Wolfe effect, but their relative contributions as a function of physical or angular scale are different, so they can be roughly distinguished on the basis of features in the temperature power spectrum. The current limit on r from CMB temperature measurements is $r \lesssim 0.2$ (95% cl) (Komatsu et al. 2011; Dunkley et al. 2011; Keisler et al. 2011). ❯ *Figure 13-25* shows the joint constraints on n_s and r from the 7-year WMAP data. In the limit that $r \lesssim 0.1$, the contribution of tensors to the temperature fluctuations becomes so small that they negligibly affect

---

[2]This prediction is not unique; for example, the cyclic model (Khoury et al. 2003) makes a similar prediction.
[3]Cyclic models predict no gravitational waves, and thus, if the waves are detected, these models will be ruled out.
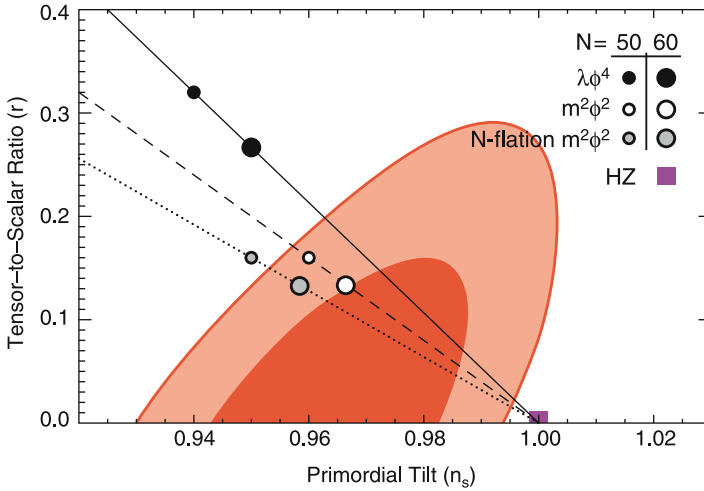
■ **Fig. 13-25**

The joint constraints on the scalar spectral index, n_s and the tensor (gravity wave) amplitude, expressed in terms of r. These constraints arise from the 7-year WMAP temperature data. (The figure is from Komatsu et al. (2011))

the power spectrum. Consequently, we need another channel for probing a weak gravitational wave background. Fortunately, there appears to be such a channel in the CMB polarization anisotropy.

6.6 Gravitational Waves and CMB Polarization

As noted above, both scalar and tensor perturbations contribute to temperature anisotropy in the CMB, via the Sachs-Wolfe effect. They both also contribute to polarization anisotropy in the CMB via Thomson scattering. However, the scalar symmetry of density perturbations restricts the polarization field these modes can produce. To understand this better, recall that polarization is a spin-2 field: any given pixel on the sky is characterized by a polarized amplitude and direction, the latter of which is invariant to rotations by $180°$.[4] Two degrees of freedom are required to describe linear polarization, the most common of which are the two Stokes parameters Q and U (Hanany et al. 2012). In analogy to vector fields, which can be decomposed into gradient and curl components, an arbitrary polarization field can also be decomposed into so-called E-mode and B-mode components (Kamionkowski et al. 1997; Zaldarriaga and Seljak 1997). The symmetry of the scalar perturbations guarantees that they can only produce the gradient-like E-mode polarization. Thus, B-mode polarization provides a unique probe of propagating gravity waves at the epoch of recombination.

Since tensor perturbations are subdominant to scalar perturbations (see above) and since tensor perturbations can produce both E-mode and B-mode polarization, while scalars produce

---

[4]We specifically consider linear polarization here. Some astrophysical sources produce circular polarization, but we do not address those.
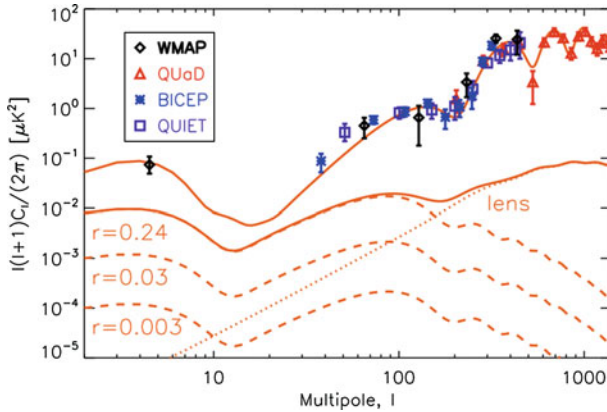
■ Fig. 13-26

Recent measurements of the CMB polarization at medium to large angular scales. The *top line* shows the E-mode spectrum in the same units as ❯ *Fig. 13-21*. The spectrum has already been quite well measured. The data are from WMAP (*diamonds*, Larson et al. (2011)), QUaD (*triangles*, Brown et al. (2009)), BICEP (asterisks, Chiang et al. (2010)), and QUIET (*squares*, QUIET Collaboration et al. (2011)). Primordial B-mode spectra are shown as *dashed lines* for different levels of primordial gravitational wave amplitude, *r*. The *top curve r* = 0.2 is disfavored at the 95% confidence level. The two peaks arise from reionization (*l* ≈ 5) and decoupling (*l* ≈ 100). The *dotted line* shows the B-mode spectrum induced by gravitational lensing of the primordial E-mode spectrum (*top*). The lensing signal is comparable to or larger than the *r* = 0.02 primordial spectrum for *l* > 20 and will be challenging to separate. Polarized foreground emission is not shown. Thus far, there is no detection of B-mode polarization in the CMB (The figure is from Katayama and Komatsu (2011))

only E-mode, it follows that B-mode polarization will be subdominant everywhere in the CMB. This makes them challenging to detect, but the rewards of doing so are high. At large angular scales, B-modes are produced by primordial gravitational waves. At all angular scales, they are produced by the gravitational lensing of E-mode polarization (Zaldarriaga and Seljak 1998). Lensing has the effect of displacing polarization "arrows," which contaminates the symmetry of the E-mode signal induced by scalar perturbations at the surface of last scattering. We discuss these two phenomena in more detail below. ❯ *Figure 13-26* shows the E-mode and B-mode power spectra predicted and measured on medium to large angular scales.

As of this writing, there has been no observation of a significant B-mode signal in the CMB polarization anisotropy. The best direct limit on B-modes comes from the BICEP team, *r* < 0.74 (95% cl) (Chiang et al. 2010).

6.7 Building on the Standard Model

The standard ΛCDM model of cosmology, a flat, expanding universe dominated by dark matter and dark energy, with a nearly scale-invariant spectrum of density fluctuations, has been been around for roughly a decade. Observations that support the model have been made over a wide

range of redshifts and wavelengths using many different cosmological observables, beyond just the CMB. To date, there are no observations in serious disagreement with the model. This is a remarkable state of affairs.

With the standard model as a foundation, there are many aspects of the model that remain to be understood. Did inflation occur in the very early universe? If so, what is the physical mechanism driving it? Is it related to spontaneous symmetry breaking? The most promising observational probes of inflation still reside in the CMB in the form of searches for B-mode polarization and non-Gaussianity in the temperature fluctuations. What is the nature of the dark energy that is driving the current acceleration of the universe? Present observations suggest a "vanilla" cosmological constant, but physicists are at a loss to understand its observed amplitude: they predict its natural value should be 10^{120} times higher than observed! Future observations of the expansion history of the universe may point to something other than a cosmological constant. What is the physics and astrophysics of cosmic structure formation? The former appear to be deeply tied to the physics of inflation; searches for primordial non-Gaussianity may be fruitful in this regard. Understanding the astrophysics is a key element of understanding how we came to be, and it may hold further clues about the nature of the dark matter.

On a different front, one may use the CMB to measure the amount of helium in the universe at the time of decoupling. This can be compared to the amount predicted by Big Bang nucleosynthesis at $z \sim 10^{10}$ and to the abundance observed today. Making sure these pieces of the puzzle fit together is an important step in cementing our understanding of Big Bang cosmology. And on yet another front, new measurements of the CMB hold the potential to constrain the sum of the neutrino masses. As discussed below, gravitational lensing of the CMB is providing a powerful new tool for probing the physics of our universe. There is much more to be done.

7 Anisotropy and Polarization Measurement Frontiers

The WMAP satellite is cosmic variance limited up to $\ell = 550$, and the Planck satellite is expected to be cosmic variance limited up to $\ell \approx 1,500$ as discussed above. In other words, assuming that the foregrounds have been properly accounted for and that any form of non-Gaussianity is negligible, all the information that can be extracted from the temperature anisotropy alone up to $\ell = 1,500$ will be present in the Planck maps. Planck will also measure the so-called E-mode polarization in the CMB and be cosmic variance limited on them to $\ell \approx 1,000$. The primordial B-modes are another independent observable that have yet to be detected. As we discuss below, there is at least one known cosmic source of non-Gaussianity. The source is the gravitational lensing of the CMB. Thus, there is an immediate motivation for pushing below the cosmic variance limit. In addition, there may be some form of primordial non-Gaussianity. Its detection would have a dramatic impact on our knowledge of how the universe began.

The two frontiers in the Planck era are the search for the large angular scale B-modes and the polarization and temperature anisotropies at fine angular scales, beyond Planck's resolution. It will be quite some time before the full sky is mapped again at Planck-like resolution with better sensitivity.

7.1 Large Angular Scale B-mode Experiments

Gravitational waves, as observed through the B-mode polarization, are a pristine probe of the early universe. This can be appreciated as follows: Quantum fluctuations in the primordial fields give rise to both scalar modes (variations in density as a function of position) and tensor modes (variations in strain – gravitational waves – as a function of position). Both scalar and tensor modes produce temperature and E-mode polarization anisotropies, but only tensor modes produce the B-mode polarization. Thus, the B-mode is distinctive. Although the gravitational waves are revealed to us through Thomson scattering off free electrons, they are unaffected by any cosmic process other than the expansion of the universe. They come to us directly from the inflation epoch.

Outside of experimental sensitivity, there are two astrophysics limitations to measuring B-modes. First, gravitational lensing of the E-mode signal masks the primordial B-mode signal for $\ell > 200$ as seen in ❯ *Fig. 13-26*. At $\ell \sim 100$, the lensed signal corresponds to $r \sim 0.02$. While it is possible to subtract the lensing, one pays a price in signal to noise. Secondly, the ultimate limit will be set by galactic foreground emission (Bock et al. 2006). Fortunately, models suggest that in the low-dust/low-synchrotron regions of sky, (Dunkley et al. 2009) we may reach $r \approx 0.02$ at 150 GHz before foregrounds become a limitation. At the largest angular scales, $\ell \lesssim 10$, polarized foreground emission dominates an $r \sim 0.02$ signal by over an order of magnitude (Page et al. 2007; Gold et al. 2011).

Measuring B-modes is challenging. Our confidence in any detection will be bolstered by multiple levels of redundancy, internal cross-checks, and agreement among experiments. The ability to identify and control systematic errors will ultimately determine the best approach (or approaches), which is not yet known. The set of experiments in ❯ *Table 13-2*, a snapshot of the current efforts focused on large angular scales, cover a wide range of technique.

◼ **Table 13-2**
This information comes from a variety of sources (papers, conversations, presentations, web pages) and is intended only for a high-level comparison between efforts. The focal planes are different and not all have two detectors (D) per feed (F). ABS has an all-cryogenic cross-Dragone style telescope and observes from Chile. CLASS, also to be sited in Chile, will target circular as well as linear polarization. KECK/BICEP has observed for a number of years from the South Pole. QUBIC, the merging of the MBI (Timbie et al. 2006) and BRAIN (Charlassier for the BRAIN Collaboration 2008) efforts, is a novel bolometric interferometer that is anticipated to benefit from the same level of control of systematic errors enjoyed by its coherent predecessors. QUIET, a cross-Dragone, is based on coherent "polarimeters on a chip" as opposed to bolometric detectors. EBEX, PIPER, and SPIDER are balloon borne

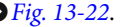| Name	Res.	Freq. (GHz)	# Feeds/Dets
ABS (Essinger-Hileman et al. 2010)	0.5°	150	240F
CLASS (Marriage, 2012, private communication)	~1°	40, 90, 150	. . .
BICEP2/KECK (Sheehy et al. 2011)	0.7°	150	256F/5x256F
QUBIC (The QUBIC collaboration et al. 2011)	0.4°	150	400F
QUIET (QUIET Collaboration et al. 2011)	0.5°	40, 90	19F/90F
EBEX (Reichborn-Kjennerud et al. 2010)	0.2°	150, 250, 410	≈1, 500
PIPER (Eimer et al. 2010; Benford et al. 2010)	~0.5°	200, 270, 350, 600	5120D
SPIDER (Crill et al. 2008)	1.1°–0.4°	90, 145, 220	1856

7.2   Small-Scale Anisotropy, $\ell > 2{,}000$

Precise measurements of the small-scale anisotropy, $\ell > 2{,}000$, are a new frontier for CMB studies and a critical complement to the Planck satellite. Because of dramatic advances in detector and receiver technology, much of it driven by CMB-experimentalists, the sky is now being observed with arcminute-level resolution with cryogenic arrays of thousands of detectors. Thousands of square degrees of sky are being mapped with sensitivities measured in tens of microKelvin per square arcminute with special purpose telescopes: the Atacama Cosmology Telescope (ACT, Fowler et al. (2007) and Swetz et al. (2011)), located in Chile, and the South Pole Telescope (SPT, Ruhl et al. (2004) and Carlstrom et al. (2011)). Soon these receivers will be polarization sensitive. Additional instruments with a range of resolutions (e.g., POLARBEAR, The Polarbear Collaboration et al. (2010), POLAR-1, Kou, 2012, private communication) will soon come on line as well. In the not-too-distant future, one expects an order-of-magnitude improvement over current sensitivities.

The scientific questions that can be addressed with these measurements include: (1) What is the scalar spectral index and to what degree is its determination contaminated by foreground emission? (2) What is the sum of the neutrino masses and are there more than three relativistic species in the early universe? (3) Did the dark energy act differently before $z = 1$? (4) Where are the missing baryons? Big Bang nucleosynthesis and CMB-derived baryon densities are not in accord with the observational census. (5) Did the early universe have only Gaussian fluctuations? The discovery of primordial non-Gaussianity, perhaps from cosmic strings or multifield inflation, would revolutionize cosmology. (6) How did the universe evolve and how did cosmic structure form? Are there cluster of galaxies so massive and distant that they challenge the Lambda-dominated cold-dark-matter model of the universe?

The questions are addressed by investigating the CMB in a number of ways. For example, at small angular scales, one may think of the CMB as a backlight with precisely known statistical properties at a precisely known distance. This light is affected by structure between us and the decoupling surface. In the Sunyaev–Zel'dovich (SZ) effect, for example, the hot electrons in galactic clusters reveal their presence by scattering the CMB with a characteristic frequency signature. In another mechanism, mass concentrations throughout the universe gravitationally lens the CMB. This lensing can be determined by examining the correlations it imposes on the CMB. Through a rich set of lensing cross-correlations with other X-ray, optical, mm-wave, and radio surveys, we can probe the formation of structure. Through yet another mechanism, we can observe the decoupling process with the CMB polarization.

At angular scales corresponding to $\ell < 2{,}000$ the anisotropy may be thought of as a direct probe of the response of the CMB to perturbations laid down in the early universe as seen at the decoupling surface at $z = 1{,}090$. The fluctuations are a part in 10^5 of the background and thus well described with linear perturbation theory. The predictions for the CMB power spectrum may be computed with exquisite accuracy. The agreement between detailed predictions and precise measurements is the foundation for our faith in the standard model of cosmology as discussed above.

As one moves to finer angular scales, new phenomena are evident as shown in ❯ *Fig. 13-22*. In the structure formation process, aggregations of dark matter result in the formation of clusters of galaxies and galaxies. At 150 GHz, after accounting for discrete radio sources, the dominant term in the power spectrum is due to confusion noise from unresolved dusty star-forming galaxies (DSFGs). They formed at redshifts between $z \sim 1$–4 and carpet the sky. Their contribution can be minimized by observing at lower frequencies but at some point a similar background from unresolved radio sources becomes important. The DSFGs are generally

described by a Poisson distribution, that is with C_ℓ is independent of ℓ, although there are correlations and clumping which lead to departures from this simple scaling (Bond 1996; Scott and White 1999; Viero et al. 2009; Hall et al. 2010; Addison et al. 2012).

Subdominant to the CMB and DSFGs at 150 GHz is the power spectrum from galactic clusters due to the Sunyaev–Zel'dovich (SZ) effects. There are two contributions. One is from the thermal effect in which the 10^7–10^8 K gas in clusters inverse Compton scatters CMB photons producing a unique frequency spectrum. When the cluster is viewed against the CMB, $T < T_{cmb}$ for frequencies below 220 GHz, and $T > T_{cmb}$ at higher temperatures. This effect was first observed in Birkinshaw et al. (1984). The second effect is from the Doppler shift of the CMB by the peculiar velocity of the cluster. In effect, the clusters act as moving mirrors. This effect was first observed by Hand et al. (2012) through stacking CMB measurements on the positions of many clusters.

Clusters are the largest gravitationally bound objects. The clusters that contribute to the power spectrum are being detected in blind surveys (Staniszewski et al. 2009; Hincks et al. 2010; Planck Collaboration et al. 2011b). They have masses greater than a few $10^{14} M_\odot$. However, roughly 50% of the amplitude comes from clusters with masses less than 2×10^{14} which will be difficult to detect in blind surveys. The SZ power spectra are produced from large simulations. The physical processes that determine the overall amplitude are all "sub grid" and must be modeled. Identifying the best description of clusters that explains X-ray, SZ, and optical data is an active area of research.

The SZ signal is approximately independent of redshift, and so clusters can be observed to great distances. The gas temperature goes as the depth of the gravitational well that led to the cluster formation and is nearly redshift independent. At high redshift, the cluster would naively appear dimmer, but back then the CMB was hotter and this compensates for the greater distance. Their mass function, $dN(> M)/dM$, that is, number distribution as a function of mass, is a sensitive probe of cosmology. Currently, the limiting factor for using clusters as cosmological probes is determining a precise mass. A typical error on the mass is 15%. Looking ahead, one anticipates the detection of over 10^5 clusters through their X-ray signature and roughly 10^4 clusters through their SZ signature. We can think of clusters as beacons positioned in a manner that lets us investigate the evolution of space-time. This will lead to a powerful check of the standard cosmological model and will undoubtedly tell us more about how cosmic structure forms and about the role of various cosmic constituents.

In the following sections we discuss three aspects of the small-scale anisotropy that will become increasingly important in the next few years. We discuss polarization and lensing, new modalities for CMB observations, and what we might learn from them. We conclude with a discussion of assessing the sum of neutrino masses through observations of the CMB.

7.2.1 Small Angular Scale Polarization

The CMB polarization is produced by different mechanisms than the temperature anisotropy and thus is sensitive to different physical processes. At small angular scale, the polarization probes the evolution of the decoupling. The polarization was predicted by Rees (1968) and Basko and Polnarev (1980) and first measured by Kovac et al. (2002). The signal is generated by Thomson scattering of a local quadrupolar radiation pattern by free electrons. The scattering of the same quadrupolar pattern in a direction perpendicular to the line of sight to the observer

has the effect of isotropizing the quadrupolar radiation field. The net polarization results from a competition between these two effects. Basko and Polnarev (1980) show that the ratio of the polarization anisotropy (E_{rms}) to the temperature (T_{rms}) signal in a flat cosmology is given by

$$\frac{E_{rms}}{T_{rms}} = \frac{\int_0^\infty \left[e^{-0.3\tau(z')} - e^{-\tau(z')}\right]\sqrt{1+z'}dz'}{\int_0^\infty \left[6e^{-\tau(z')} + e^{-0.3\tau(z')}\right]\sqrt{1+z'}dz'}, \qquad (13.12)$$

where $\tau(z) = c\sigma_T \int_0^z n_e(z')dz'(dt/dz')$ is the optical depth. Here, σ_T is the Thomson cross section, c is the speed of light, and n_e is the free-electron density. Using a typical optical depth (e.g., Peebles 1968b; Zel'dovich et al. 1969), one finds $E_{rms} \approx 0.05\, T_{rms}$. The difference in brackets in the numerator sets the range in z over which polarization is generated. For example, if the decoupling epoch entailed an instantaneous transition from an extremely high optical depth ($\tau \gg 1$) to transparency ($\tau = 0$), there would be no polarization signal. Thus, the polarization is produced at a particular time. In contrast, the processes that lead to the temperature anisotropy take place over a much longer time.

At decoupling, the polarization producing quadrupole results from velocity gradients in the flow of the primordial plasma. More specifically, in the rest frame of an electron in such a flow, the radiation background has a quadrupolar pattern proportional to the velocity gradient, $\nabla \vec{v}$, and the mean free path between scatterings, λ. Just before decoupling, $z > z_{dec}$, the photons are tightly coupled to the electrons, and λ is small. Thus, the polarization is small. As decoupling proceeds, λ increases and the quadrupole magnitude increases. The process is cut off at lower redshift because the optical depth drops so rapidly. In the context of inflationary cosmology, Harari and Zaldarriaga (1993) show that in Fourier space the polarization signal is $\propto kv\Delta$, where k is the wavevector and $\Delta \approx \lambda$ is the width of the last scattering surface.

❯ *Figure 13-27* shows a snap shot of the $\ell > 200$ polarization spectrum along with predictions for what Planck will measure. The plot also shows the levels achievable with the current generation of polarization-sensitive experiments aimed at high ℓ. With E-mode polarization, one may probe the damping tail more deeply than with temperature and therefore better measure n_s. In addition, since the E-mode polarization arises from different physical processes, alternative models can be tested. For example, current power spectrum data indicate that temperature fluctuations are adiabatic to within 9% and 2% for axion and curvaton-type dark matter (Komatsu et al. 2009; Sollom et al. 2009). Small-scale temperature and polarization data will provide a new test of these alternative models.

As discussed above, our most direct probe of the infant universe is the scalar spectral index, n_s, and its change with scale. The formal accuracy on n_s from the Planck satellite is 0.5%. However, our confidence in the result will depend on detailed knowledge of the transition from the linear regime (primary CMB) to the nonlinear regime (secondary CMB). This transition can only be measured through the fine-scale anisotropy. In addition, we will want to be certain that n_s is not being affected by foreground emission, point sources, or low levels of secondary anisotropies. This is best done through the polarization.

The promise of the polarization as a new probe of cosmology is noteworthy. The CMB polarization was first observed just a decade ago. Now it looks like the cleanest measure of the CMB power spectrum over an appreciable range in ℓ may come not from the temperature but from the polarization.
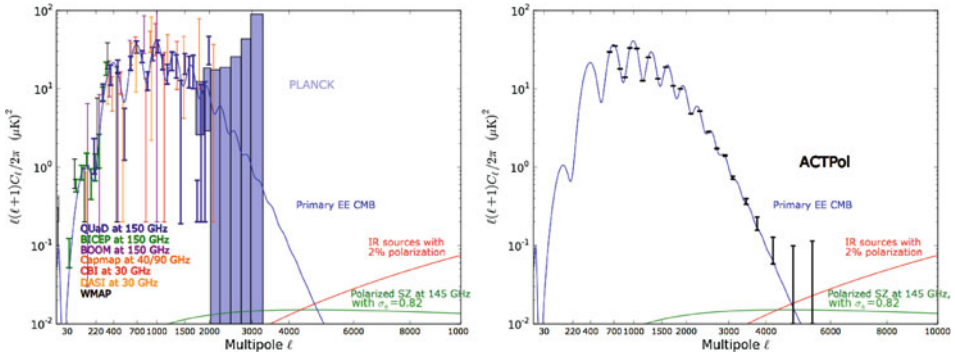
⬛ Fig. 13-27

Left: **The current state of measurements of the E-mode polarization spectrum plotted over the best-fit ΛCDM model. Data are from QUaD (Brown et al. 2009), BICEP (Chiang et al. 2010), Boomerang (Montroy et al. 2006), CAPMAP (Bischoff et al. 2008), CBI (Sievers et al. 2007), DASI (Kovac et al. 2002), and WMAP (Larson et al. 2011). The Planck-projected errors are shown as *blue boxes*. The foregrounds are conservative estimates for IR point sources and a 1% net polarization of the SZ effect.** *Right:* **Projection of the errors from polarization-sensitive receivers on ACT and SPT. Note that the CMB is significantly more polarized than the foreground emission, permitting a detailed investigating of the damping tail and lensing**

7.2.2 Lensing of the CMB

One of the forefronts of CMB observations is the lensing of the CMB by matter fluctuations between us and the surface of last scattering. We see in many optical telescope images magnificent pictures of distant galaxies being gravitationally lensed by a large cluster of galaxies between us and the very distant galaxies. ❯ *Figure 13-28* shows an example. One thing to note is that the lensed objects are highly distorted. They can be magnified and elongated.

For the CMB, one replaces the distant galaxies by the CMB itself, and instead of the intervening galaxy, one has a universe full of matter fluctuations. The same power spectrum, $P(k)$, that gives rise to the temperature anisotropy also gives rise to the clumpiness of the universe between us and the surface of last scattering. In place of seeing beautiful images of distorted galaxies, the hot and cold spots in the CBM are subtly distorted but in such a manner as to not change surface brightness.

CMB lensing is described in a number of seminal papers (e.g., Blanchard and Schneider 1987; Seljak 1996) and in several recent review articles (e.g., Lewis and Challinor 2006; Smith et al. 2009). It is quantified as follows. When we measure the temperature at a given spot we find

$$T(\boldsymbol{n}) = T^u(\boldsymbol{n} + \vec{d}(\boldsymbol{n})), \tag{13.13}$$

where T^u is the unlensed temperature distribution, $\boldsymbol{n}$ is the direction of the observation, and $\vec{d}$ is the deflection field transverse to the direction. The deflection field may be written as the gradient of a potential, $\vec{d} = \nabla_{\boldsymbol{n}}\phi$. In turn, the lensing potential is related to the distribution of the gravitational potential throughout the universe, Ψ, as

$$\phi(\boldsymbol{n}) = -2 \int_0^{z_{\text{dec}}} \frac{\Psi(z, D(z)\boldsymbol{n})}{H(z)} \left(\frac{D(z_{\text{dec}}) - D(z)}{D(z_{\text{dec}})D(z)} \right) dz. \tag{13.14}$$
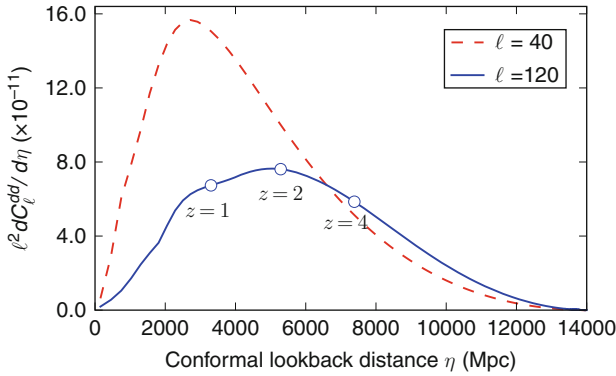
◾ Fig. 13-28

A Hubble Space Telescope image of the galaxy cluster MACS J1206.2-0847 from the CLASH survey. The distortion of the distant galaxies is clearly evident. Such a cluster also distorts the CMB although the observations are not as dramatic

For CMB lensing, the source is fixed at the decoupling surface at a redshift of z_{dec}. The quantity $D(z)$ is the comoving distance to an object at redshift z. Inside the large parentheses, one sees the familiar expression for the geometry of an object at z_{dec} being deflected by a lens at $D(z)$. The integral sums up contributions over Ψ, the source of the deflections. The power spectrum of ϕ is given by

$$C_\ell^{\phi\phi} = \frac{8\pi^2}{\ell^3} \int_0^{z_{\text{dec}}} \frac{D(z)}{H(z)} \left(\frac{D(z_{\text{dec}}) - D(z)}{D(z_{\text{dec}})D(z)} \right)^2 P_\Psi(z,k) dz, \tag{13.15}$$

where $P_\Psi(z,k)$ is the power spectrum of the gravitational potential as a function of redshift and k-vector, with $k = (\ell + 1/2)/D(z)$. In the literature, one sees a number of expressions for the lensing power spectrum. For the power spectrum of the deflection angle, $C_\ell^{dd} = \ell^2 C_\ell^{\phi\phi}$. For numerical work, the convergence, $\kappa = \frac{1}{2}\nabla \cdot \vec{d}$, is particularly convenient. In this case, $C_\ell^{\kappa\kappa} = \ell^2 C_\ell^{dd}/4$.

❷ *Figure 13-29* shows the lensing kernel, the integrand in (❷ 13.15), as a function of the conformal look-back distance η for two different values of ℓ. Most of the dependence on ℓ arises because different values of ℓ pick out different ranges of wavelengths k from the power spectrum $P_\Psi(k = (\ell+1/2)/D(z), z)$. Note that the kernel picks out a broad distribution at relatively high z. This is why lensing is especially sensitive to the sum of neutrino masses and early time dark energy.

◼ Fig. 13-29

The CMB lensing kernel as a function of conformal look-back distance, η. The decoupling surface is at η_{dec} = 14,000 Mpc for z_{dec} = 1,090. Note that different values of ℓ weight contributions from our past differently (Figure courtesy of Sudeep Das)

For the CMB, the lensing distortion leads to a change in statistical distribution of the fluctuations. Without lensing, the distribution of CMB temperature fluctuations is Gaussian, and the phases are uncorrelated. Lensing correlates the phases, as is so evident in ❯ *Fig. 13-28*, and adds kurtosis (4-pt function) to the Gaussian. The source of the correlations may be seen in (❯ 13.13). An expansion gives $T(\boldsymbol{n}) = T^u(\boldsymbol{n}) + \nabla T^u(\boldsymbol{n})\vec{d}(\boldsymbol{n}) + \ldots$. The second term is significant when the CMB temperature gradients and deflections are large. From ❯ *Figs. 13-21* and ❯ *13-22* we see that the temperature gradients are high on the degree angular scales corresponding to the first peak. These correspond to $\ell \sim 100$. From (❯ 13.14), one finds that the rms deflection is roughly 2.5 arcmin. This angular scale corresponds to $\ell \sim 3,000$. CMB lensing is dominated by deflections of 2.5 arcmin that are coherent over degree angular scales. Thus, the power spectrum of $\ell^2 C_\ell^{dd}$ has a broad hump near $\ell = 50$.

To observe lensing, one wants arcmin resolution maps of the CMB that have good statistical properties at degree angular scales. Currently, the Planck, ACT, and SPT maps satisfy these criteria. The connection between the CMB maps and the above is made with an optimal quadratic estimator (Hu and Okamoto 2002; Das et al. 2011a):

$$(2\pi)^2 \delta(L - L') C_L^{\kappa\kappa} = |N^\kappa(L)|^2 \int \frac{d^2\ell}{(2\pi)^2} \int \frac{d^2\ell'}{(2\pi)^2} |g(\ell, L)|^2$$
$$\times \{ T^*(\ell) T^*(L - \ell) T(\ell') T(L' - \ell') - < T^*(\ell) T^*(L - \ell) T(\ell')$$
$$T(L' - \ell') >_{\text{Gauss}} \}, \qquad (13.16)$$

where ℓ and ℓ' are for the high-resolution CMB maps, g is a filter that can be tuned to optimize signal-to-noise, and N is a normalization. ❯ Equation 13.17 manifestly shows that the convergence power spectrum is related to the four-point function. The second term in brackets is the Gaussian part of the four-point function. This must be subtracted from the full expression to isolate the terms that are responsible for correlating the phases. The Gaussian part can be determined by randomizing the phases in the 2D transform of the map (Dvorkin and Smith 2009; Hanson et al. 2011; Das et al. 2011a).
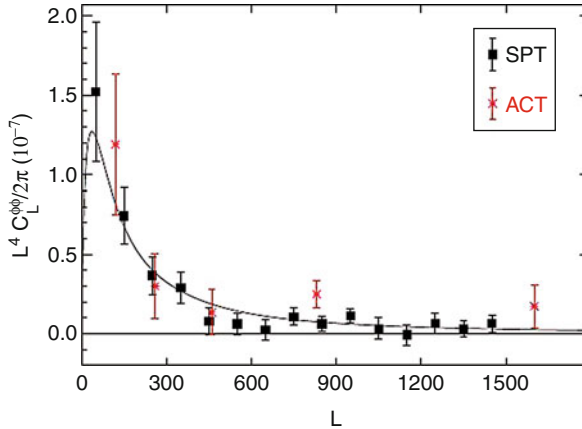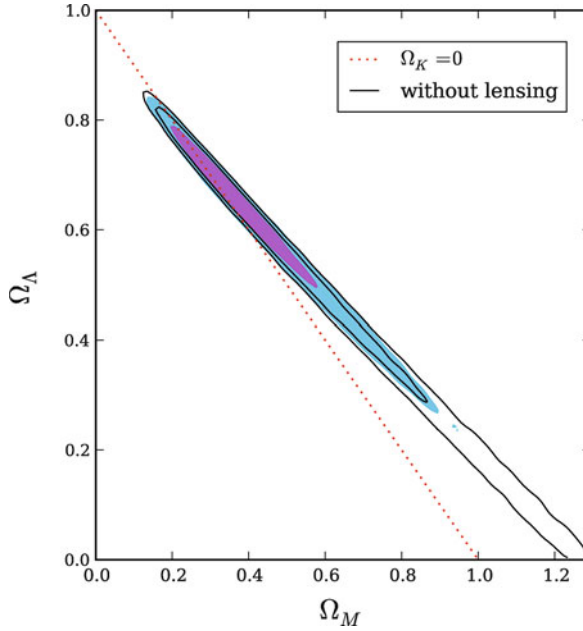
◼ Fig. 13-30
The CMB lensing power spectrum, $C^{\kappa\kappa}$, and measurements from the ACT and SPT teams. The theoretical power spectrum peaks at $L \sim 50$ (Figure from van Engelen et al. (2012))

Lensing of the CMB was first clearly seen through a cross-correlation with radio galaxy counts (Smith et al. 2007) and the Sloan Digital Sky Survey (Hirata et al. 2008). There was also $\sim 3\sigma$ evidence for it from the power spectrum of the CMB (Lueker et al. 2010; Das et al. 2011b). The first detection that was rooted in the characteristic aspects of lensing of the CMB alone was reported in Das et al. (2011a) and based on the ACT data. The lensing power spectrum, $C^{\kappa\kappa}$, was detected at 4σ. Next, van Engelen et al. (2012)) reported a more than 6σ detection of $C^{\kappa\kappa}$ from the SPT. The results are shown in ❷ *Figs. 13-30* and ❷ *13-31*.

CMB lensing is a new observational handle on the cosmos. The deflection field is a measure of the effects of the matter fluctuations between us and the decoupling surface and thus probes different physical processes than does the primary anisotropy. Thus, with lensing, one uses the CMB to extract information about the volume of the universe and breaks the "geometric degeneracy" associated with the primary anisotropy. This is an exciting direction for observations of the CMB. For example, it means that with only the CMB, we can determine the geometry of the universe or, in other words, using only the CMB, one can deduce that there must be a dark-energy term. Because the signal is intrinsically non-Gaussian, it also means that there is reason to push beyond the cosmic variance limited measurements of the temperature anisotropy.

❷ *Figure 13-32*, adapted from Smith et al. (2009), shows the sensitivity of the lensing power spectrum to various cosmological parameters of interest. To connect with the measurements we just discussed, we examine curvature. At $L \sim 300$, the change in $C_L^{\kappa\kappa}$ with Ω_k is -0.4. In other words, to constrain Ω_k to 25%, one must measure $C_L^{\kappa\kappa}$ to 0.1. This is roughly the size of the error bars in ❷ *Fig. 13-30*.

A number of studies have been made about how well one could do in principle on the parameters to which lensing is particularly sensitive. A review based on a possible future satellite mission is given in Smith et al. (2009). For an instrument with a resolution of 5 arcmin and a sensitivity of 4 μK-arcmin (1σ noise of 4 μK for each 1 arcmin square pixel) over the full sky, one can reach a 1σ sensitivity on the mass of the neutrino of 0.05 eV, on the equation of state for early time dark energy of 0.15, and on Ω_k of 0.0025. One obtains similar sensitivities by observing a quarter of the sky with 2 arcmin resolution to a depth of 5 μK-arcmin. As a point of reference, at 150 GHz the Planck satellite has a resolution of roughly 7 arcmin and is expected

◘ Fig. 13-31
The space of models that fit the CMB alone similar to those shown in ❯ *Fig. 13-23*. The *solid black* lines show the 1σ and 2σ contours for what may achieved with the CMB alone without lensing. Note that an $\Omega_\Lambda = 0$, $\Omega_m = 1.23$ is a perfectly acceptable model. The colored contours show the same constraints but with the ACT lensing included (Sherwin et al. (2011)). The geometric degeneracy is broken and $\Omega_\Lambda = 0$ is excluded at 3.8σ
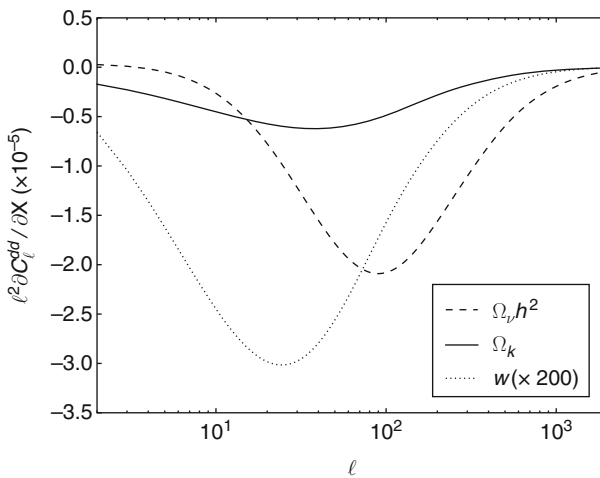
◘ Fig. 13-32
The sensitivity to the lensing power spectrum (❯ *Fig. 13-30*) to the sum of neutrino masses, early dark energy, and spatial curvature, Ω_k (Figure courtesy of Sudeep Das)

to achieve an average of $\approx 50\,\mu K$-arcmin over the whole sky. From the ground, ACT and SPT are achieving $\approx 20\,\mu K$-arcmin with a resolution of 1–1.5 arcmin over significant regions of sky.

The CMB lensing deflection field may also be correlated with the SZ effect, galaxy shear, quasars, the LRGs, and a host of other phenomena to find the growth rate of structure. The growth rate in turn is another probe of dark energy and the mass of the neutrino. CMB lensing may be combined with many other cosmic probes. For example, when combined with the LSST and Planck (e.g., Joudaki and Kaplinghat 2011), one may in principle determine the equation of state of the early dark energy to better than a percent and curvature to 0.06%.
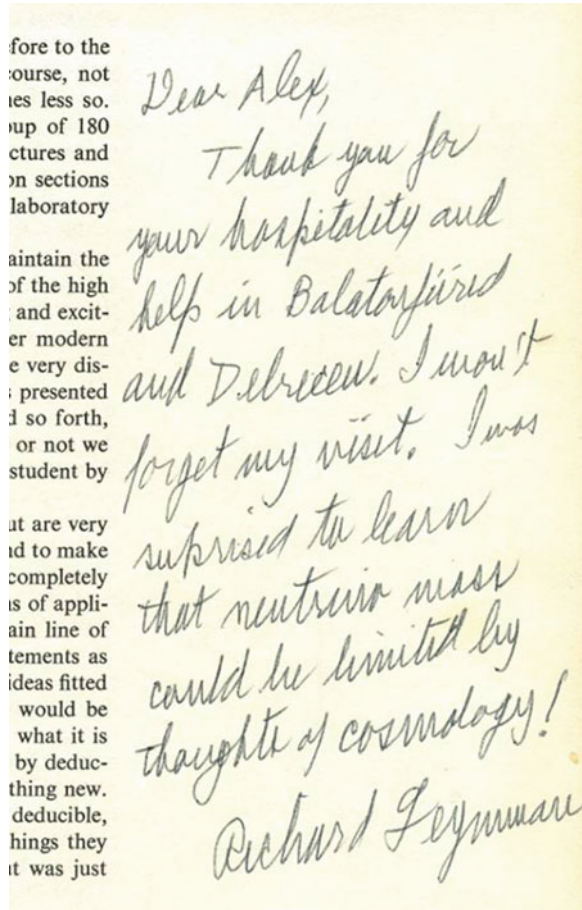
7.2.3 Neutrinos

The properties of neutrinos affect the appearance of the CMB. To be more precise, a weakly interacting relativistic particle in the early universe can affect the CMB just as neutrinos would. But because neutrinos exist, we associate them with this primordial constituent. There could well be neutrinos plus additional weakly interacting relativistic particles, but for the purposes of this chapter, we will lump them all together. Neutrinos affect the CMB through their response to gravity. Thus, from the CMB we cannot tell that the particles are, for example, Dirac or Majorana particles (the signature is the same for both) or even if they are spin 1/2. However, we can tell the number of relativistic species and the sum of the neutrino masses. With the technologies currently being developed, we will be able to determine the mass sum in multiple independent ways to a level of roughly 0.06 eV, near the current *lower* limit set by atmospheric neutrino oscillations.

Before getting into details, it is worth noting that neutrinos have been part of the cosmological picture since the earliest days. Understanding them was critical to Big Bang nucleosynthesis. At one point, hints of a 30 eV mass led many to consider them as a major cosmological constituent. In 1972, Alex Szalay was a college student at the Eötvös University in Hungary. Following the advice of Zel'dovich, he computed how one could find the neutrino mass from cosmological observations as part of his undergraduate thesis. That year, the Neutrino '72 conference meet in Balatonfüred, Hungary. Szalay's work on neutrinos was presented at the conference. After the conference, Feynman wrote him the note in ❯ *Fig. 13-33*. His undergraduate work grew into his Ph.D. thesis; computing the effect of neutrinos on density fluctuations would later become Szalay and Marx (1976). The first link between the CMB and neutrino mass was presented in Doroshkevich et al. (1981) and Bond and Szalay (1983).

First consider electron neutrinos. At a redshift of ~10^{10}, electrons,[5] positrons, and photons were strongly coupled through the reaction $\gamma + \gamma \leftrightarrow e^+ + e^-$. In turn, the electrons and positrons were coupled to the neutrinos through $\nu + \bar{\nu} \leftrightarrow e^+ + e^-$. All the particles were highly relativistic. At these early times, the energy density in photons was σT_γ^4 and that of neutrinos was $(7/8)\,\sigma T_\nu^4$ with $T_\nu = T_\gamma$ and σ the Stefan-Boltzmann constant. The factor of 7/8 is from the integral over a Fermi-Dirac distribution as opposed to a Bose-Einstein distribution. When the temperature of the universe cooled to $T \approx m_e c^2 / k$, or $z \approx 2 \times 10^9$, the vast majority of electrons and positrons annihilated and dumped their energy into the photons. This increased the temperature of the photons relative to the neutrinos by $T_\gamma = (11/4)^{1/3} T_\nu$. Thus, today $T_\nu = 1.95$ K.

The neutrinos today are still distributed according to an orbital occupation number of $n_\nu = \frac{2}{e^{q/kT_\nu}+1}$, where $q = pac$ with p the relativistic momentum, $T_\nu = 1.95$ K, a the scale factor, and

---

[5] $m_e c^2 \sim 0.5$ MeV corresponds to $T = 6 \times 10^9$ K.
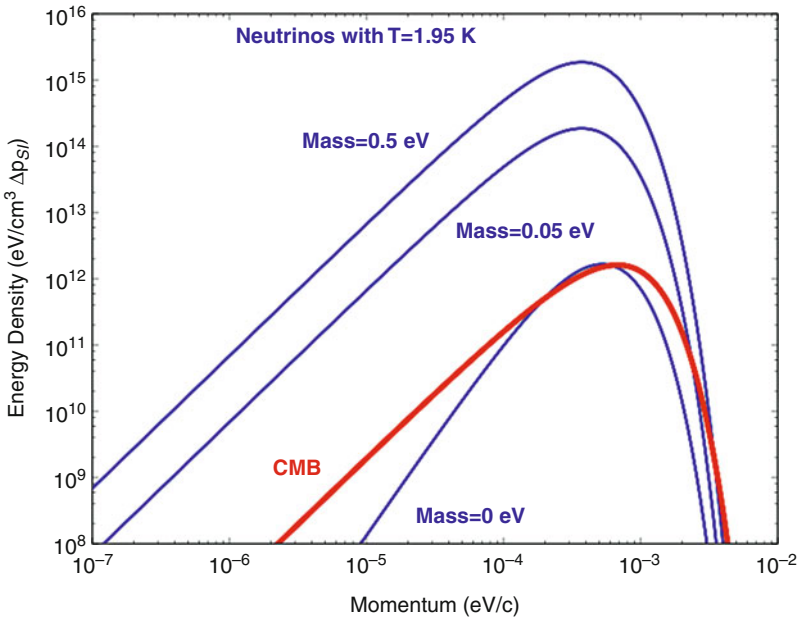
◘ Fig. 13-33
Note from Richard Feynman to Alex Szalay inscribed inside Szalay's copy of the Feynman lectures

the factor of 2 accounts for the two spin states. This occupation number does not change if the neutrinos are massive. In other words, the occupation is set when they are highly relativistic. Because the expansion of the universe is adiabatic, the neutrinos do not change orbitals as the universe evolves.

The energy density today for a single species is given by

$$\rho = \frac{8\pi}{(hc)^3} \frac{1}{a^4} \int_0^\infty q^2 n_v \sqrt{q^2 + m_v^2 c^2 a^2} \, dq. \tag{13.17}$$

In ❯ *Fig. 13-34*, the distribution of the neutrino background (the integrand of (❯ 13.17)) is compared to that of the Planck distribution for the CMB. If $m_v = 0$, then the energy density as a function of momentum, p, is similar to that of the photons, but the peak is shifted to the left because the neutrinos are slightly colder. In addition, the low momentum tail falls off more quickly than for photons due to the "+" sign in the denominator of n_v as opposed to "−" sign for photons. As the neutrino mass increases, the energy term in (❯ 13.17) becomes independent of q, and thus the low momentum tail of the distribution is proportional to q^2. The photons have
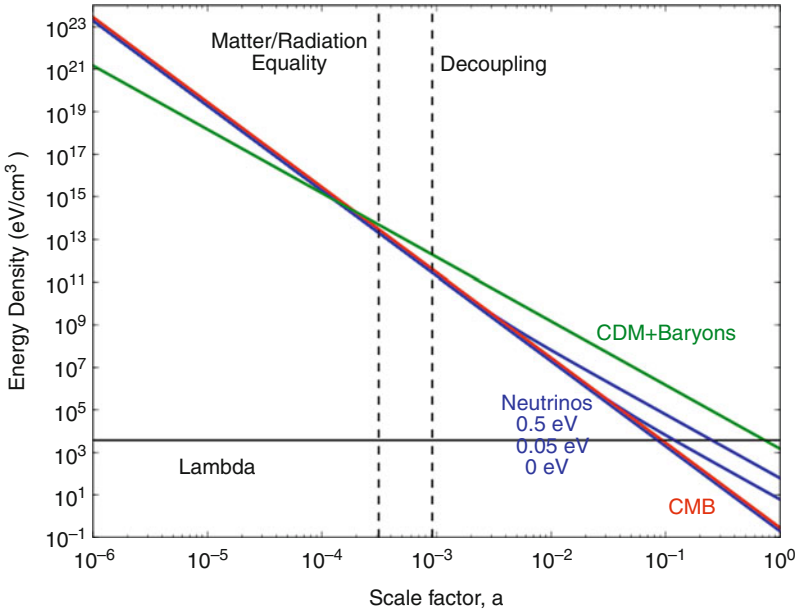
◼ Fig. 13-34

The neutrino energy distribution as a function of neutrino momentum. The integral of the *top curve* tells us that the current energy density for a species of neutrino with a mass of 0.5 eV is 55 eV/cm³. We know the mass of one species must be at least 0.05 eV, and so for these the energy density is 5.5 eV/cm³. For the CMB, the energy density is 0.28 eV/cm³ today

the same distribution at low momentum but for a different reason; here, the q dependence in the denominator of the occupation number cancels the q in the energy dependence.

When thinking about neutrinos, the two most important times in cosmic evolution are matter-radiation equality and decoupling. In the the standard six-parameter, Λ-dominated flat cosmology, these occur at $z_{eq} = 3,140$ and $z_{dec} = 1,090$ respectively (Komatsu et al. 2011). The essential feature of z_{eq} is that for $z > z_{eq}$ the expansion rate of the universe slows down and the formation of cosmic structure can begin. Neutrinos, for any mass compatible with the data, act relativistically at matter-radiation equality. By relativistic we mean $kT_{\nu} \gtrsim m_{\nu}c^2$. ❷ *Figure 13-35* shows the energy density of various cosmic constituents as a function of scale factor of the universe. For neutrinos, blue lines, this is simply ρ in (❷ 13.17). The energy density in radiation (the CMB) scales as $1/a^4$, the energy density in matter scales as $1/a^3$, and the energy density in a cosmological constant is independent of a.

From ❷ *Fig. 13-35* we can gain an intuition for how neutrinos affect the CMB. First, let us examine the number of relativistic species, N_{eff}. We know there are three families of neutrinos, and so from particle physics, expect $N_{eff} = 3$. In the cosmological context, we define N_{eff} through

$$\rho_{rad} \equiv \left(1 + \frac{7}{8}\left(\frac{4}{11}\right)^{4/3} N_{eff}\right)\rho_{\gamma}. \tag{13.18}$$

◼ Fig. 13-35

The scaling of the cosmic constituents with scale factor *a*. Green is for CDM and baryons, *blue* is for neutrinos of three different rest masses, 0.5, 0.05, and 0 eV, *red* is the CMB, and *solid black* is the cosmological constant. Note that for all viable neutrino masses, neutrinos scale with the expansion like radiation before $a \approx 2 \times 10^3$ and like matter now. The mass corresponding to $T_\nu = 1.95$ K is $m_\nu = 0.2$ meV

Because the annihilation of e^+ with e^- does not result in all of the energy going into photons alone, some goes to the neutrinos, and thus $N_{\text{eff}} = 3.04$ in (❷ 13.18) (Mangano et al. 2005; Kneller and Steigman 2004). If $N_{\text{eff}} > 3.04$, then in ❷ *Fig. 13-35*, the blue lines near z_{eq} and z_{dec} are shifted up. As a result, z_{eq} is closer to z_{dec}. This means that prior to decoupling, the higher N_{eff}, the greater the expansion rate. This is a result of the fact that a radiation-dominated universe expands more rapidly than does a matter-dominated one. As pointed out in Bashinsky and Seljak (2004) and Hou et al. (2011), this leads to increased Silk damping and thus a suppression of the anisotropy at $l > 1,000$. An outline of the argument is as follows: the diffusion scale of a photon, r_d, scales as $1/\sqrt{H}$, where H is the expansion parameter prior to decoupling. If r_d increases, there is more diffusion and thus more Silk damping. One way to view the scaling (Hou et al. 2011) is that r_d increased as $t^{1/2}$ as one would expect of diffusion. However, as H increases, t decreases and r_d decreases. For the CMB, the other key scale is the acoustic horizon, $r_A = \theta_A D_a$ with D_a the angular diameter distance, and θ_A the angle. The quantity θ_A is precisely determined by the $\ell < 500$ anisotropy data to be $\theta_A = 0.5953 \pm 0.0014°$ (Komatsu et al. 2011). The sound horizon, r_A, is essentially the sound speed multiplied by time and so scales as $1/H$. Since θ_A is so well constrained by the data, the relevant quantity is r_d/r_A which scales as H. Thus, the more relativistic species there are, the larger H at the decoupling era and the larger the damping scale relative to the acoustic scale. The result is more suppression of the $l > 1,000$ damping tail relative to the acoustic peaks.

The damping tail is also affected by the fraction of helium. The more helium, the more electrons are bound up in atoms, the longer the diffusion length for a photon, and therefore the greater the suppression of the CMB fluctuations. As a result, there is some degeneracy between the primordial helium fraction and the number of relativistic species. The two effects, though, can be separated (see, e.g., Jungman et al. 1996; Dunkley et al. 2011).

Massive neutrinos affect how we interpret the CMB in a number of ways. For example, for all allowed mass sums ($0.05 < \Sigma_\nu < 0.5$ eV), the neutrinos are nonrelativistic today and should be counted as part of the matter budget as indicated on the right hand side of ❯ *Fig. 13-35*. However, for the same mass range, they are part of the radiation budget at decoupling. Thus, to constrain the mass, one compares measures of the mass fluctuations at low redshift, for example, with the σ_8 parameter, to the fluctuations that give rise to the CMB.

The mass of the neutrino also directly affects the acoustic peak structure and the growth rate of structure. There are multiple effects at play as discussed in, for example, Dodelson et al. (1996) and Ichikawa et al. (2005) (see also Hannestad and Brandbyge 2010). The driving concepts are that at z_{dec} the neutrino temperature is roughly 2,000 K corresponding to 0.1 eV, and so massive neutrinos are in the process of becoming nonrelativistic. Also, while photons in the decoupling epoch diffuse out of potential wells as they scatter off electrons, neutrinos free stream out of potential wells as their interactions are minimal. The net effect is that the phase and amplitudes of the acoustic peaks are slightly altered and that the more massive the neutrino, the greater the suppression of the formation of cosmic structure at small scales.

This suppression of structure leads to a decrease in the CMB lensing signal as evident in ❯ *Fig. 13-32*. Note that this signal is based solely on CMB observations and does not depend on additional measures of galaxy spectra or σ_8. As noted above, the signal can be extracted from the non-Gaussianity of the CMB. Also note how characteristic the signal is in the lensing spectrum. There is a second way to see the neutrino mass signature that offers a built-in cross check. At high ℓ, B-mode polarization is produced by the gravitational lensing of the E-modes (Zaldarriaga and Seljak 1998). This is the same mechanism that leads to a confounding astrophysical signal at low ℓ that hides the primordial B-modes. It is convenient that in polarization this region is relatively free of foreground emission. ❯ *Figure 13-36* shows the effect. If the neutrino mass sum is 0.5 eV, the lensing B-mode signal is suppressed by roughly 25%.

7.3 The Future

There is still much to be learned from the CMB. The advantages of observing from space are so strong that we should anticipate a future satellite mission. Space offers long uninterrupted periods of observation from a platform whose thermal stability can be measured in milliKelvin. This combination enables a myriad of possible consistency checks for various systematic effects. The history of the field is one of great advances made with ground-based and suborbital experiments that then inform a satellite design. Detector sensitivities near 2 mm wavelength are approaching levels where they will be limited by the photon noise from the CMB itself. Soon this will be the case across the frequency band where the CMB dominates. We have learned how to produce polarization-sensitive arrays of hundreds to thousands of detectors that are read out with low-power superconducting electronics. There are no known impediments to even larger arrays. Many groups are investigating new kinds of radiometers based on technologies ranging from multimoded detectors and optics to multichroic detectors with broad-band optics. There are advances with both bolometric and coherent systems. The field is dynamic. The instruments
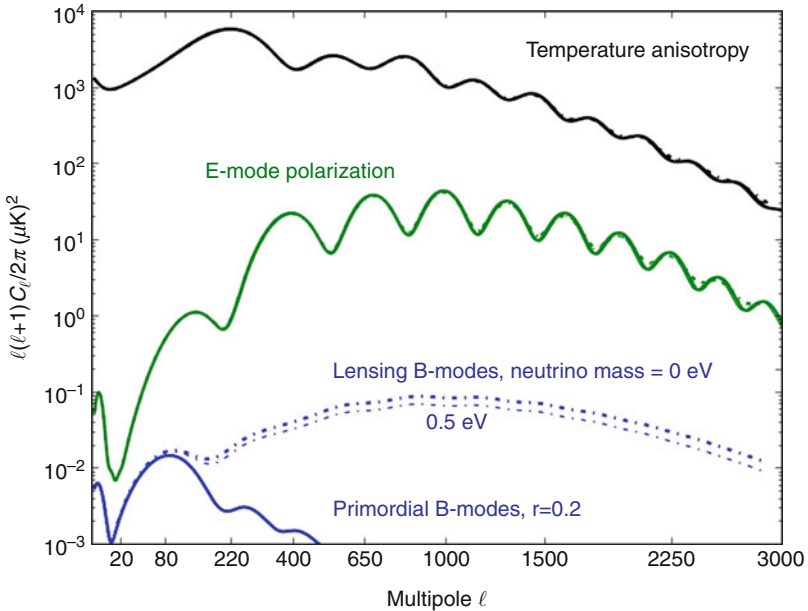
◼ Fig. 13-36

The effect of massive neutrinos on the CMB polarization spectrum. Matter fluctuations between us and the surface of last scattering lens the CMB. This can be detected directly in at least two ways. One can isolate the non-Gaussian aspect part of the temperature anisotropy and extract the B-mode signal from that. Another way is to measure B-modes that result from lensing of the E-modes. This is a particularly clean signal near these wavelengths. This figure shows the difference in the B-mode signal for neutrinos with a 0 mass sum and those with an 0.5 eV mass sum. For comparison, the primordial B-mode signal with $r = 0.2$ is also shown. Current error bars on the temperature anisotropy are near $1\,\mu K^2$, and so measuring the high-ℓ B-modes is not far off

being developed define the forefront in receiver technology. We expect many more exciting results over the coming years. However, as we probe ever deeper to search for more subtle aspects of nature, a future space mission will be required.

Acknowledgments

manuscript and made many useful comments. We thank Sudeep Das for useful comments and for providing figures on CMB lensing. Shaul Hanany, Colin Hill, Bill Jones, Akito Kusaka, Avi Loeb, and Suzanne Staggs made a number of helpful comments.

References

Addison, G. E., et al. 2012, ApJ, 752(2), article id. 120

Aguirre, A. 1999, ApJ, 521, 17

Aguirre, A. N. 2000, ApJ, 533, 1

Albrecht, A., & Steinhardt, P. J. 1982, Phys. Rev. Lett., 48, 1220

Ali-Haïmoud, Y., & Hirata, C. M. 2011, Phys. Rev. D, 83, 043513

Ali-Haïmoud, Y., Hirata, C. M., & Dickinson, C. 2009, MNRAS, 395, 1055

Alizadeh, E., & Hirata, C. M. 2011, Phys. Rev. D, 84, 083011

Alpher, R. A., & Herman, R. C. 1948, Phys. Rev., 74, 1737

Bardeen, J. M., Steinhardt, P. J., & Turner, M. S. 1983, Phys. Rev. D, 28, 679

Bashinsky, S., & Seljak, U. 2004, Phys. Rev. D, 69, 083002

Basko, M. M., & Polnarev, A. G. 1980, MNRAS, 191, 207

Baumann, D., et al. 2009, in American Institute of Physics Conf. Ser. 1141, ed. S. Dodelson, D. Baumann, A. Cooray, J. Dunkley, A. Fraisse, M. G. Jackson, A. Kogut, L. Krauss, M. Zaldarriaga, & K. Smith, 10–120

Benford, D. J., et al. 2010, in Society of Photo-Optical Instrumentation Engineers (SPIE) Conf. Ser., 7741

Bennett, C. L., et al. 1996, ApJL, 464, L1

Bennett, C. L., et al. 2003a, ApJS, 148, 97

Bennett, C. L. et al. 2003b, ApJ, 583, 1

Benoît, A., et al. 2003, A&A, 399, L19

Birkinshaw, M., Gull, S. F., & Hardebeck, H. 1984, Phy. Rev. Lett., 309, 34

Bischoff, C., et al. 2008, ApJ, 684, 771

Blanchard, A., & Schneider, J. 1987, A&A, 184, 1

Bock, J., et al. 2006, ArXiv Astrophysics e-prints

Boggess, N. W., et al. 1992, ApJ, 397, 420

Bond, J. R. 1996, in Cosmology and Large Scale Structure, Les Houches Session LX, ed. R. Schaeffer, J. Silk, M. Spiro, & J. Zinn-Justin (London: Elsevier), 469

Bond, J. R., & Szalay, A. S. 1983, ApJ, 274, 443

Bondi, H., & Gold, T. 1948, MNRAS, 108, 252

Bracewell, R. N., & Conklin, E. K. 1968, Nature, 219, 1343

Brown, M. L., et al. 2009, ApJ, 705, 978

Burigana, C., et al. 1991, ApJ, 379, 1

Burns, J. O., et al. 2012, Adv. Space Res., 49, 433

Carbone, C., Baccigalupi, C., Bartelmann, M., Matarrese, S., & Springel, V. 2009, MNRAS, 396, 668

Carlstrom, J. E., et al. 2011, PASP, 123, 568

Charlassier, R., for the BRAIN Collaboration 2008, in Proceeding of the 43rd "Rencontres de Moriond" on Cosmology, La Thuile, Italy, March 15–22, 2008

Chiang, H. C., et al. 2010, ApJ, 711, 1123

Chluba, J., Erickcek, A. L., & Ben-Dayan, I. 2012a, ArXiv e-prints

Chluba, J., Khatri, R., & Sunyaev, R. A. 2012b, ArXiv e-prints

Chluba, J., & Sunyaev, R. A. 2006, A&A, 458, L29

Chluba, J., & Sunyaev, R. A. 2012a, MNRAS, 419, 1294

Chluba, J., & Sunyaev, R. A. 2012b, MNRAS, 419, 1294

Conklin, E. K. 1969, Nature, 222, 971

Coppola, C. M., D'Introno, R., Galli, D., Tennyson, J., & Longo, S. 2012a, ApJS, 199, 16

Coppola, C. M., D'Introno, R., Galli, D., Tennyson, J., & Longo, S. 2012b, ApJS, 199, 16

Corey, B. E., & Wilkinson, D. T. 1976, in Bulletin of the American Astronomical Society, Vol. 8, 351

Crill, B. P., et al. 2008, in Society of Photo-Optical Instrumentation Engineers (SPIE) Conf. Ser., 7010

Daly, R. A. 1991, ApJ, 371, 14

Das, S., et al. 2011a, Phys. Rev. Lett., 107, 021301

Das, S., et al. 2011b, ApJ, 729, 62

de Bernardis, P., et al. 2000, Nature, 404, 955

de Oliveira-Costa, A., Kogut, A., Devlin, M. J., Netterfield, C. B., Page, L. A., & Wollack, E. J. 1997, ApJL, 482, L17

de Vega, H. J., & Sanchez, N. G. 2010, MNRAS, 404, 885

Dicke, R. H., Peebles, P. J. E., Roll, P. G., & Wilkinson, D. T. 1965, ApJ, 142, 414

Dodelson, S., Gates, E., & Stebbins, A. 1996, ApJ, 467, 10

Doroshkevich, A. G., Khlopov, M. I., Sunyaev, R. A., Szalay, A. S., & Zeldovich, I. B. 1981, Ann. NY Acad. Sci., 375, 32

Draine, B. T., & Lazarian, A. 1998, ApJ, 508, 157

Draine, B. T., & Lazarian, A. 1999, ApJ, 512, 740

Dubrovich, V. K. 1975, Sov. Astron. Lett., 1, 196

Dubrovich, V. K., & Stolyarov, V. A. 1995, A&A, 302, 635

Dunkley, J., et al. 2009, in American Institute of Physics Conf. Ser., 1141, ed. S. Dodelson, D. Baumann, A. Cooray, J. Dunkley, A. Fraisse, M. G. Jackson, A. Kogut, L. Krauss, M. Zaldarriaga, & K. Smith, 222–264

Dunkley, J., et al. 2011, ApJ, 739, 52

Dvorkin, C., & Smith, K. M. 2009, Phys. Rev. D, 79, 043003

Eimer, J. R., et al. 2010, in Society of Photo-Optical Instrumentation Engineers (SPIE) Conf. Ser., 7733

Einstein, A. 1917, Sitzungsberichte der Königlich Preußischen Akademie der Wissenschaften (Berlin), Seite 142–152., 142

Essinger-Hileman, T., et al. 2010, in Astrophysics - Instrumentation and Methods for Astrophysics, Astrophysics - Cosmology and Extragalactic Astrophysics. Proceedings of the Thirteenth International Conference on Low-Temperature Detectors

Feng, J. L., Rajaraman, A., & Takayama, F. 2003, Phys. Rev. D, 68, 063504

Fixsen, D. J. 2009, ApJ, 707, 916

Fixsen, D. J., & Dwek, E. 2002, ApJ, 578, 1009

Fixsen, D. J., Cheng, E. S., Gales, J. M., Mather, J. C., Shafer, R. A., & Wright, E. L. 1996, ApJ, 473, 576

Fixsen, D. J., Hinshaw, G., Bennett, C. L., & Mather, J. C. 1997, ApJ, 486, 623

Fixsen, D. J., Bennett, C. L., & Mather, J. C. 1999, ApJ, 526, 207

Fixsen, D. J., Wollack, E. J., Kogut, A., Limon, M., Mirel, P., Singal, J., & Fixsen, S. M. 2006, Rev. Sci. Instrum., 77, 064905

Fowler, J. W., et al. 2007, Appl. Opt., 46, 3444

Friedman, A. 1922, Z. Phys., 10, 377

Fukugita, M., & Kawasaki, M. 1990, ApJ, 353, 384

Galli, S., Bean, R., Melchiorri, A., & Silk, J. 2008, Phys. Rev. D, 78, 063532

Ganga, K., Cheng, E., Meyer, S., & Page, L. 1993, ApJL, 410, L57

Gervasi, M., Zannoni, M., Tartari, A., Boella, G., & Sironi, G. 2008, ApJ, 688, 24

Gnedin, N. I., & Ostriker, J. P. 1992, ApJ, 400, 1

Gold, B., et al. 2011, ApJS, 192, 15

Guth, A. H. 1981, Phys. Rev. D, 23, 347

Guth, A. H., & Pi, S.-Y. 1982, Phys. Rev. Lett., 49, 1110

Gush, H. P., Halpern, M., & Wishnow, E. H. 1990, Phys. Rev. Lett., 65, 537

Hall, N. R., et al. 2010, ApJ, 718, 632

Halverson, N. W., et al. 2002, ApJ, 568, 38

Hanany, S., et al. 2000, ApJL, 545, L5

Hanany, S., Niemack, M., & Page, L. 2012, CMB Optics (Springer), Planets, Stars and Stellar Systems (PSSS)

Hand, N., et al. 2012, ArXiv e-prints

Hannestad, S., & Brandbyge, J. 2010, JCAP, 3, 20

Hanson, D., Challinor, A., Efstathiou, G., & Bielewicz, P. 2011, Phys. Rev. D, 83, 043005

Harari, D. D., & Zaldarriaga, M. 1993, Phys. Lett. B, 319, 96

Harrison, E. R. 1970, Phys. Rev. D, 1, 2726

Haslam, C. G. T., Klein, U., Salter, C. J., Stoffel, H., Wilson, W. E., Cleary, M. N., Cooke, D. J., & Thomasson, P. 1981, A&A, 100, 209

Hawking, S. W. 1982, Phys. Lett. B, 115, 295

Herzberg, G. 1950, Molecular Spectra and Molecular Structure. Vol.1: Spectra of Diatomic Molecules (New York: Van Nostrand Reinhold)

Hincks, A. D., et al. 2010, ApJS, 191, 423

Hinshaw, G., et al. 2003, ApJS, 148, 135

Hinshaw, G., et al. 2009, ApJS, 180, 225

Hirata, C. M., Ho, S., Padmanabhan, N., Seljak, U., & Bahcall, N. A. 2008, Phys. Rev. D, 78, 043520

Hooper, D., & Linden, T. 2011, Phys. Rev. D, 83, 083517

Hou, Z., Keisler, R., Knox, L., Millea, M., & Reichardt, C. 2011, ArXiv e-prints

Howlett, C., Lewis, A., Hall, A., & Challinor, A. 2012, JCAP, 4, 27

Hoyle, F. 1948, MNRAS, 108, 372

Hu, W., & Okamoto, T. 2002, ApJ, 574, 566

Hu, W., Scott, D., & Silk, J. 1994, ApJL, 430, L5

Hubble, E. 1929, Proc. Natl. Acad. Sci., 15, 168

Ichikawa, K., Fukugita, M., & Kawasaki, M. 2005, Phys. Rev. D, 71, 043001

Illarionov, A. F., & Sunyaev, R. A. 1974, Astronomicheskii Zh., 51, 1162

Illarionov, A. F., & Sunyaev, R. A. 1975a, Sov. Astron., 18, 413

Illarionov, A. F., & Sunyaev, R. A. 1975b, Sov. Astron., 18, 691

Jarosik, N., et al. 2011, ApJS, 192, 14

Jedamzik, K., Katalinić, V., & Olinto, A. V. 2000, Phys. Rev. Lett., 85, 700

Joudaki, S., & Kaplinghat, M. 2011, ArXiv e-prints

Jungman, G., Kamionkowski, M., Kosowsky, A., & Spergel, D. N. 1996, Phys. Rev. D, 54, 1332

Kamionkowski, M., Kosowsky, A., & Stebbins, A. 1997, Phys. Rev. D, 55, 7368

Katayama, N., & Komatsu, E. 2011, ApJ, 737, 78

Keisler, R., et al. 2011, ApJ, 743(1), article id. 28

Kelsall, T., et al. 1998, ApJ, 508, 44

Khatri, R., Sunyaev, R. A., & Chluba, J. 2011, arXiv:1110.0475

Kneller, J. P., & Steigman, G. 2004, New J. Phys., 6, 117

Khoury, J., Steinhardt, P. J., & Turok, N. 2003, Phy. Rev. Lett., 91, 16, 161301

Knox, L., & Page, L. 2000, Phys. Rev. Lett., 85, 1366

Kogut, A., Banday, A. J., Bennett, C. L., Górski, K. M., Hinshaw, G., & Reach, W. T. 1996, ApJ, 460, 1

Kogut, A., Wollack, E., Fixsen, D. J., Limon, M., Mirel, P., Levin, S., Seiffert, M., & Lubin, P. M. 2004, Rev. Sci. Instrum., 75, 5079

Kogut, A., et al. 2011, J. Cosmol. Astropart. Phys., 7, 25

Komatsu, E., et al. 2009, ApJS, 180, 330

Komatsu, E., et al. 2011, ApJS, 192, 18

Kosowsky, A., & Turner, M. S. 1995, Phys. Rev. D, 52, 1739

Kovac, J. M., Leitch, E. M., Pryke, C., Carlstrom, J. E., Halverson, N. W., & Holzapfel, W. L. 2002, Nature, 420, 772

Kuo, C. L., et al. 2004, ApJ, 600, 32

Larson, D., et al. 2011, ApJS, 192, 16

Layzer, D., & Hively, R. 1973, ApJ, 179, 361

Lee, A. T. et al. 2001, ApJL, 561, L1

Leitch, E. M., Readhead, A. C. S., Pearson, T. J., & Myers, S. T. 1997, ApJL, 486, L23

Lemaître, G. 1927, Ann. Soc. Sci. Brux., 47, 49

Lemaître, G. 1931, MNRAS, 91, 490

Lewis, A., & Challinor, A. 2006, Phys. Rep., 429, 1

Linde, A. D. 1982, Phys. Lett., B108, 389

Lueker, M., et al. 2010, ApJ, 719, 1045

Maeda, K., Alvarez, H., Aparici, J., May, J., & Reich, P. 1999, A&AS, 140, 145

Mangano, G., Miele, G., Pastor, S., Pinto, T., Pisanti, O., & Serpico, P. D. 2005, Nucl. Phys. B, 729, 221

Martin, D., & Puplett, E. 1970, Infrared Phys., 10, 105

Mather, J. C., et al. 1990, ApJL, 354, L37

Mather, J. C., Fixsen, D. J., Shafer, R. A., Mosier, C., & Wilkinson, D. T. 1999, ApJ, 512, 511

Matsumoto, T., Hayakawa, S., Matsuo, H., Murakami, H., Sato, S., Lange, A. E., & Richards, P. L. 1988, ApJ, 329, 567

Mauskopf, P. D., et al. 2000, ApJL, 536, L59

McDonald, P., Scherrer, R. J., & Walker, T. P. 2001, Phys. Rev. D, 63, 023001

McKellar, A. 1941, Publ. Dominion Astrophys. Obs. Vic., 7, 251

Miller, A. D., et al. 1999, ApJL, 524, L1

Miller, A. D. et al. 2002, ApJS, 140, 115

Montroy, T. E., et al. 2006, ApJ, 647, 813

Mukhanov, V. F., & Chibisov, G. V. 1981, Sov. J. Exp. Theor. Phys. Lett., 33, 532

Netterfield, C. B., Devlin, M. J., Jarosik, N., Page, L., & Wollack, E. J. 1997, ApJ, 474, 47

Netterfield, C. B. et al. 2002, ApJ, 571, 604

Ostriker, J. P., & Cowie, L. L. 1981, ApJL, 243, L127

Ostriker, J. P., & Thompson, C. 1987, ApJL, 323, L97

Page, L., et al. 2007, ApJS, 170, 335

Pardo, J. R., Cernicharo, J., & Serabyn, E. 2001, IEEE Trans. Antennas Propag., 49, 1683

Pearson, T. J., et al. 2003, ApJ, 591, 556

Peebles, P. J. E. 1968a, ApJ, 153, 1

Peebles, P. J. E. 1968b, ApJ, 153, 1

Peebles, P. J., & Wilkinson, D. T. 1968, Phys. Rev., 174, 2168

Peebles, P. J. E., & Yu, J. T. 1970, ApJ, 162, 815

Peebles, P. J. E., Seager, S., & Hu, W. 2000, ApJL, 539, L1

Peebles, P. J. E., Page, L. A., & Partridge, R. B., (ed.) 2009, Finding the Big Bang (Cambridge University Press)

Penzias, A. A., & Wilson, R. W. 1965, ApJ, 142, 419

Planck Collaboration, et al. 2011a, A&A, 536, A1

Planck Collaboration, et al. 2011b, A&A, 536, A8

QUIET Collaboration, et al. 2011, ApJ, 741, 111

Readhead, A. C. S., et al. 2004, ApJ, 609, 498

Rees, M. J. 1968, ApJL, 153, L1

Reich, P., & Reich, W. 1986, A&AS, 63, 205

Reichborn-Kjennerud, B., et al. 2010, in Society of Photo-Optical Instrumentation Engineers (SPIE) Conf. Ser., 7741

Riess, A. G., et al. 2011, ApJ, 730, 119

Roger, R. S., Costain, C. H., Landecker, T. L., & Swerdlyk, C. M. 1999, A&AS, 137, 7

Roll, P. G., & Wilkinson, D. T. 1966, Phys. Rev. Lett., 16, 405

Rubiño-Martín, J. A., Chluba, J., & Sunyaev, R. A. 2008, A&A, 485, 377

Ruhl, J. E., et al. 2003, ApJ, 599, 786

Ruhl, J., et al. 2004, in Society of Photo-Optical Instrumentation Engineers (SPIE) Conf. Ser. 5498, ed. C. M. Bradford, P. A. R. Ade, J. E. Aguirre, J. J. Bock, M. Dragovan, L. Duband, L. Earle, J. Glenn, H. Matsuhara, B. J. Naylor, H. T. Nguyen, M. Yun, & J. Zmuidzinas, 11–29

Sachs, R. K., & Wolfe, A. M. 1967, ApJ, 147, 73

Sato, K. 1981, MNRAS, 195, 467

Scott, D., & White, M. 1999, A&A, 346, 1

Seager, S., Sasselov, D. D., & Scott, D. 1999, ApJL, 523, L1

Seager, S., Sasselov, D. D., & Scott, D. 2011, in Astrophysics Source Code Library, record ascl:1106.026, 6026

Seiffert, M., et al. 2011, ApJ, 734, 6

Seljak, U. 1996, ApJ, 463, 1

Sheehy, C. D., et al. 2010, in SPIE Proceedings for Millimeter, Submillimeter and Far-Infrared Detectors and Instrumentation for Astronomy V (Conference 7741, San Diego, CA, USA)

Sherwin, B. D., et al. 2011, Phys. Rev. Lett., 107, 021302

Shirokoff, E., et al. 2011, ApJ, 736, 61

Sievers, J. L., et al. 2007, ApJ, 660, 976

Silk, J. 1968, ApJ, 151, 459

Silk, J., & Stebbins, A. 1983, ApJ, 269, 1

Singal, J., et al. 2011, ApJ, 730, 138

Smith, K. M., Zahn, O., & Doré, O. 2007, Phys. Rev. D, 76, 043510

Smith, K. M., et al. 2009, in American Institute of Physics Conf. Ser. 1141, ed. S. Dodelson, D. Baumann, A. Cooray, J. Dunkley, A. Fraisse, M. G. Jackson, A. Kogut, L. Krauss, M. Zaldarriaga, & K. Smith , 121–178

Smoot, G. F., Gorenstein, M. V., & Muller, R. A. 1977, Phys. Rev. Lett., 39, 898

Smoot, G. F., et al. 1992, ApJL, 396, L1

Sollom, I., Challinor, A., & Hobson, M. P. 2009, Phys. Rev. D, 79, 123521

Staniszewski, Z., et al. 2009, ApJ, 701, 32

Starobinsky, A. A. 1982, Phys. Lett. B, 117, 175

Sunyaev, R. A., & Chluba, J. 2009, Astron. Nachr., 330, 657

Sunyaev, R. A., & Zel'dovich, Y. B. 1970a, Astrophys. Space Sci., 7, 3

Sunyaev, R. A., & Zel'dovich, Y. B. 1970b, Astrophys. Space Sci., 7, 20

Swetz, D. S., et al. 2011, ApJS, 194, 41

Switzer, E. R., & Hirata, C. M. 2005, Phys. Rev. D, 72, 083002

Switzer, E. R., & Hirata, C. M. 2008, Phys. Rev. D, 77, 083006

Szalay, A. S., & Marx, G. 1976, A&A, 49, 437

Taburet, N., Hernández-Monteagudo, C., Aghanim, N., Douspis, M., & Sunyaev, R. A. 2011, MNRAS, 418, 2207

Tashiro, H., Sabancilar, E., & Vachaspati, T. 2012, ArXiv:1202.2474

Tegmark, M. 1996, ApJL, 464, L35

The Polarbear Collaboration, et al. 2010, POLARBEAR the web, arXiv e-print (arXiv:1011.0763)

The QUBIC collaboration, et al. 2011, AP, 34(9), 705–716

Timbie, P. T., et al. 2006, New Astron. Rev., 50, 999

van Engelen, A., et al. 2012, ArXiv e-prints

Varshalovich, D. A., & Khersonskii, V. K. 1977, Sov. Astron. Lett., 3, 155

Vernstrom, T., Scott, D., & Wall, J. V. 2011, MNRAS, 415, 3641

Viero, M. P., et al. 2009, ApJ, 707, 1766

Webster, A. S. 1974, MNRAS, 166, 355

Weiss, R. 1980, ARAA, 18, 489

Partridge, R. B., & Wilkinson, D. T. 1967, Phy. Rev. Lett., 18, 557–559

Winston, R. 1970, J. Opt. Soc. Am. (1917–1983), 60, 245

Woody, D. P., & Richards, P. L. 1979, Phys. Rev. Lett., 42, 925

Woody, D. P., Mather, J. C., Nishioka, N. S., & Richards, P. L. 1975, Phys. Rev. Lett., 34, 1036

Wright, E. L. 1979, ApJ, 232, 348

Wright, E. L. 1982, ApJ, 255, 401

Wright, E. L. 2012, Wright Cosmology Tutorial. http://www.astro.ucla.edu/~wright/CMB.html

Wright, E. L., et al. 1991, ApJ, 381, 200

Wright, E. L., et al. 1992, ApJL, 396, L13

Wright, E. L., et al. 1994, ApJ, 420, 450

Zaldarriaga, M., & Seljak, U. 1997, Phys. Rev. D, 55, 1830

Zaldarriaga, M., & Seljak, U. 1998, Phys. Rev. D, 58, 023003

Zannoni, M., Tartari, A., Gervasi, M., Boella, G., Sironi, G., De Lucia, A., Passerini, A., & Cavaliere, F. 2008, ApJ, 688, 12

Zel'dovich, Y. B. 1963, Sov. J. Exp. Theor. Phys., 16, 1395

Zel'dovich, Y. B. 1972, MNRAS, 160, 1P

Zel'dovich, Y. B., Kurt, V. G., & Sunyaev, R. A. 1969, Sov. J. Exp. Theor. Phys., 28, 146